Université de Montréal

Characterization of Carotid Artery Plaques Using Noninvasive Vascular Ultrasound Elastography

par Hongliang Li

Département de pharmacologie et physiologie/Institut de génie biomédical/Faculté de médecine

Thèse présentée en vue de l'obtention du grade de Philosophiae Doctor (Ph.D.) en génie biomédical

September 2019

Université de Montréal

Faculté des études supérieures et postdoctorales

Cette thèse intitulée :

Characterization of Carotid Artery Plaques Using Noninvasive Vascular Ultrasound Elastography

Présentée par :
Hongliang Li

a été évalué par un jury composé des personnes suivantes :

Fréderic Leblond, Ph.D.
Président-rapporteur

Guy Cloutier, Ph.D.
Directeur de recherche

Samuel Kadoury, Ph.D.
Membre du jury

Siddhartha Sikdar, Ph.D.
Examinateur externe

Alain Vinet, Ph.D.
Représentant du doyen de la FESP

Résumé

L'athérosclérose est une maladie vasculaire complexe qui affecte la paroi des artères (par l'épaississement) et les lumières (par la formation de plaques). La rupture d'une plaque de l'artère carotide peut également provoquer un accident vasculaire cérébral ischémique et des complications. Bien que plusieurs modalités d'imagerie médicale soient actuellement utilisées pour évaluer la stabilité d'une plaque, elles présentent des limitations telles que l'irradiation, les propriétés invasives, une faible disponibilité clinique et un coût élevé. L'échographie est une méthode d'imagerie sûre qui permet une analyse en temps réel pour l'évaluation des tissus biologiques. Il est intéressant et prometteur d'appliquer une échographie vasculaire pour le dépistage et le diagnostic précoces des plaques d'artère carotide. Cependant, les ultrasons vasculaires actuels identifient uniquement la morphologie d'une plaque en termes de luminosité d'écho ou l'impact de cette plaque sur les caractéristiques de l'écoulement sanguin, ce qui peut ne pas être suffisant pour diagnostiquer l'importance de la plaque. La technique d'élastographie vasculaire non-intrusive (« noninvasive vascular elastography (NIVE) ») a montré le potentiel de détermination de la stabilité d'une plaque. NIVE peut déterminer le champ de déformation de la paroi vasculaire en mouvement d'une artère carotide provoqué par la pulsation cardiaque naturelle. En raison des différences de module de Young entre les différents tissus des vaisseaux, différents composants d'une plaque devraient présenter différentes déformations, caractérisant ainsi la stabilité de la plaque.

Actuellement, les performances et l'efficacité numérique sous-optimales limitent l'acceptation clinique de NIVE en tant que méthode rapide et efficace pour le diagnostic précoce des plaques vulnérables. Par conséquent, il est nécessaire de développer NIVE en tant qu'outil d'imagerie non invasif, rapide et économique afin de mieux caractériser la vulnérabilité liée à la plaque. La procédure à suivre pour effectuer l'analyse NIVE consiste en des étapes de formation et de post-traitement d'images. Cette thèse vise à améliorer systématiquement la précision de ces deux aspects de NIVE afin de faciliter la prédiction de la vulnérabilité de la plaque carotidienne.

Le premier effort de cette thèse a été dédié à la formation d'images (Chapitre 5). L'imagerie par oscillations transversales a été introduite dans NIVE. Les performances de

l'imagerie par oscillations transversales couplées à deux estimateurs de contrainte fondés sur un modèle de déformation fine, soit l' « affine phase-based estimator (APBE) » et le « Lagrangian speckle model estimator (LSME) », ont été évaluées. Pour toutes les études de simulation et *in vitro* de ce travail, le LSME sans imagerie par oscillation transversale a surperformé par rapport à l'APBE avec imagerie par oscillations transversales. Néanmoins, des estimations de contrainte principales comparables ou meilleures pourraient être obtenues avec le LSME en utilisant une imagerie par oscillations transversales dans le cas de structures tissulaires complexes et hétérogènes.

Lors de l'acquisition de signaux ultrasonores pour la formation d'images, des mouvements hors du plan perpendiculaire au plan de balayage bidimensionnel (2-D) existent. Le deuxième objectif de cette thèse était d'évaluer l'influence des mouvements hors plan sur les performances du NIVE 2-D (Chapitre 6). À cette fin, nous avons conçu un dispositif expérimental *in vitro* permettant de simuler des mouvements hors plan de 1 mm, 2 mm et 3 mm. Les résultats *in vitro* ont montré plus d'artefacts d'estimation de contrainte pour le LSME avec des amplitudes croissantes de mouvements hors du plan principal de l'image. Malgré tout, nous avons néanmoins obtenu des estimations de déformations robustes avec un mouvement hors plan de 2.0 mm (coefficients de corrélation supérieurs à 0.85). Pour un jeu de données cliniques de 18 participants présentant une sténose de l'artère carotide, nous avons proposé d'utiliser deux jeux de données d'analyses sur la même plaque carotidienne, soit des images transversales et longitudinales, afin de déduire les mouvements hors plan (qui se sont avérés de 0.25 mm à 1.04 mm). Les résultats cliniques ont montré que les estimations de déformations restaient reproductibles pour toutes les amplitudes de mouvement, puisque les coefficients de corrélation inter-images étaient supérieurs à 0.70 et que les corrélations croisées normalisées entre les images radiofréquences étaient supérieures à 0.93, ce qui a permis de démontrer une plus grande confiance lors de l'analyse de jeu de données cliniques de plaques carotides à l'aide du LSME.

Enfin, en ce qui concerne le post-traitement des images, les algorithmes NIVE doivent estimer les déformations des parois des vaisseaux à partir d'images reconstituées dans le but d'identifier les tissus mous et durs. Ainsi, le dernier objectif de cette thèse était de développer un algorithme d'estimation de contrainte avec une résolution de la taille d'un pixel ainsi qu'une efficacité de calcul élevée pour l'amélioration de la précision de NIVE (Chapitre 7). Nous avons

proposé un estimateur de déformation de modèle fragmenté (SMSE) avec lequel le champ de déformation dense est paramétré avec des descriptions de transformées en cosinus discret, générant ainsi des composantes de déformations affines (déformations axiales et latérales et en cisaillement) sans opération mathématique de dérivées. En comparant avec le LSME, le SMSE a réduit les erreurs d'estimation lors des tests de simulations, ainsi que pour les mesures *in vitro* et *in vivo*. De plus, la faible mise en œuvre de la méthode SMSE réduit de 4 à 25 fois le temps de traitement par rapport à la méthode LSME pour les simulations, les études *in vitro* et *in vivo*, ce qui pourrait permettre une implémentation possible de NIVE en temps réel.

Mots-clés : Athérosclérose, plaque vulnérable, élastographie par ultrasons, oscillations transversales, imagerie par ondes planes, mouvements hors plan, imagerie à haute résolution, transformées en cosinus discret, modèle clairsemé, flux optique, estimation de phase, estimation de contraintes affines.

Abstract

Atherosclerosis is a complex vascular disease that affects artery walls (by thickening) and lumens (by plaque formation). The rupture of a carotid artery plaque may also induce ischemic stroke and complications. Despite the use of several medical imaging modalities to evaluate the stability of a plaque, they present limitations such as irradiation, invasive property, low clinical availability and high cost. Ultrasound is a safe imaging method with a real time capability for assessment of biological tissues. It is clinically used for early screening and diagnosis of carotid artery plaques. However, current vascular ultrasound technologies only identify the morphology of a plaque in terms of echo brightness or the impact of the vessel narrowing on flow properties, which may not be sufficient for optimum diagnosis. Noninvasive vascular elastography (NIVE) has been shown of interest for determining the stability of a plaque. Specifically, NIVE can determine the strain field of the moving vessel wall of a carotid artery caused by the natural cardiac pulsation. Due to Young's modulus differences among different vessel tissues, different components of a plaque can be detected as they present different strains thereby potentially helping in characterizing the plaque stability.

Currently, sub-optimum performance and computational efficiency limit the clinical acceptance of NIVE as a fast and efficient method for the early diagnosis of vulnerable plaques. Therefore, there is a need to further develop NIVE as a non-invasive, fast and low computational cost imaging tool to better characterize the plaque vulnerability. The procedure to perform NIVE analysis consists in image formation and image post-processing steps. This thesis aimed to systematically improve the accuracy of these two aspects of NIVE to facilitate predicting carotid plaque vulnerability.

The first effort of this thesis has been targeted on improving the image formation (Chapter 5). Transverse oscillation beamforming was introduced into NIVE. The performance of transverse oscillation imaging coupled with two model-based strain estimators, the affine phase-based estimator (APBE) and the Lagrangian speckle model estimator (LSME), were evaluated. For all simulations and *in vitro* studies, the LSME without transverse oscillation imaging outperformed the APBE with transverse oscillation imaging. Nonetheless, comparable

or better principal strain estimates could be obtained with the LSME using transverse oscillation imaging in the case of complex and heterogeneous tissue structures.

During the acquisition of ultrasound signals for image formation, out-of-plane motions which are perpendicular to the two-dimensional (2-D) scan plane are existing. The second objective of this thesis was to evaluate the influence of out-of-plane motions on the performance of 2-D NIVE (Chapter 6). For this purpose, we designed an *in vitro* experimental setup to simulate out-of-plane motions of 1 mm, 2 mm and 3 mm. The *in vitro* results showed more strain estimation artifacts for the LSME with increasing magnitudes of out-of-plane motions. Even so, robust strain estimations were nevertheless obtained with 2.0 mm out-of-plane motion (correlation coefficients higher than 0.85). For a clinical dataset of 18 participants with carotid artery stenosis, we proposed to use two datasets of scans on the same carotid plaque, one cross-sectional and the other in a longitudinal view, to deduce the out-of-plane motions (estimated to be ranging from 0.25 mm to 1.04 mm). Clinical results showed that strain estimations remained reproducible for all motion magnitudes since inter-frame correlation coefficients were higher than 0.70, and normalized cross-correlations between radiofrequency images were above 0.93, which indicated that confident motion estimations can be obtained when analyzing clinical dataset of carotid plaques using the LSME.

Finally, regarding the image post-processing component of NIVE algorithms to estimate strains of vessel walls from reconstructed images with the objective of identifying soft and hard tissues, we developed a strain estimation method with a pixel-wise resolution as well as a high computation efficiency for improving NIVE (Chapter 7). We proposed a sparse model strain estimator (SMSE) for which the dense strain field is parameterized with Discrete Cosine Transform descriptions, thereby deriving affine strain components (axial and lateral strains and shears) without mathematical derivative operations. Compared with the LSME, the SMSE reduced estimation errors in simulations, *in vitro* and *in vivo* tests. Moreover, the sparse implementation of the SMSE reduced the processing time by a factor of 4 to 25 compared with the LSME based on simulations, *in vitro* and *in vivo* results, which is suggesting a possible implementation of NIVE in real time.

Keywords : Atherosclerosis, vulnerable plaque, ultrasound elastography, transverse oscillations, plane wave imaging, out-of-plane motions, high-resolution imaging, discrete cosine transforms, sparse model, optical flow, phase estimation, affine strain estimation.

Table of contents

List of tables

List of figures

List of symbols

c : The speed of sound

Z : Acoustic impedance

R : Acoustic reflection coefficient

D_{depth} : Maximum imaging depth

τ : The time delays applied on transducer elements

d_{pitch} : The distance between two adjacent transducer elements

θ : The steering or tilted angle of plane wave transmission

r : Pixel intensities of the reference frame

$\bar{r}$: The mean intensity of pixels inside the measure window from the reference frame

t : Pixel intensities of the target frame

$\bar{t}$: The mean intensity of pixels inside the measure window from the target frame

I_x : The spatial derivative of image intensity in the lateral direction

I_z : The spatial derivative of image intensity in the axial direction

I_t : The derivative of image intensity in the temporal direction

U_x : Lateral displacement

U_z : Axial displacement

s_{xx} : Lateral strain

s_{xz} : Lateral shear strain

s_{zx} : Axial shear strain

s_{zz} : Axial strain

Θ : The phase of a cross-spectrum

k_x : The frequency variable in the lateral direction

k_z : The frequency variable in the axial direction

f_x : The modulated spatial frequency in the lateral direction

f_z : The modulated spatial frequency in the axial direction

λ_x : The expected lateral oscillation wavelength of transverse oscillation beamforming

λ_z : The transmitted pulse wavelength

σ_x : The full width at half maximum of a Gaussian envelope

Φ : The phase difference of two Fourier spectrums

ϕ : The phase of an analytical image

n_t : The time-ensemble length

Δt : The time step between two consecutive frames

E : Elasticity modulus

γ : Poisson's ratio

ε_{min} : Principal minor strain

ε_{max} : Principal major strain

div : Divergence operator

λ_d : The regularization parameter to regulate the influence of incompressibility constraint

λ_s : The regularization parameter to regulate the influence of smoothness constraint

$\mathbf{c_x}$: The coefficients of Discrete Cosine Transform of a lateral displacement field

$\mathbf{c_y}$: The coefficients of Discrete Cosine Transform of an axial displacement field

B : The Discrete Cosine Transform matrix

$\mathbf{B}^{\boldsymbol{x}}$: The first-order derivative of **B** in the lateral direction

$\mathbf{B}^{\boldsymbol{y}}$: The first-order derivative of **B** in the axial direction

$\dot{D}$: First-order derivative operator

$\ddot{D}$: Two-order derivative operator

List of abbreviations

CT : Computed tomography

MRI : Magnetic resonance imaging

IVUS : Intravascular ultrasound

CEUS : Contrast-enhanced ultrasound

OCT : Optical coherence tomography

DSA : Digital subtraction angiography

PET : Positron emission tomography

SPECT : Single photon emission computed tomography

NIRF : Near-infrared fluorescence

NIVE : Noninvasive vascular elastography

RF : Radiofrequency

CPWC : Coherent plane wave compounding

TO : Transverse oscillation

CPWC&TO : Coherent plane wave compounding with transverse oscillation beamforming

CPWC&TO* : CPWC with TO beamforming and heterodyne demodulation

LSME : Lagrangian speckle model estimator

$LSME^{T}$: LSME with the time-ensemble approach

$LSME^{T\&I}$: LSME with the time-ensemble approach and the incompressibility constraint

PBE : Phase-based estimator

APBE : Affine phase-based estimator

$APBE^{T}$: APBE with the time-ensemble approach

$APBE^{T\&I}$: APBE with the time-ensemble approach and the incompressibility constraint

SMSE : Sparse model strain estimator

FWHM : Full width at half maximum

HS : Horn-Schunck

LK : Lucas-Kanade

OF : Optical flow

ROI : Region of interest

LDL : Low-density lipoproteins

AHA : American Heart Association

LRNC : Lipid-rich necrotic core

IPH : Intraplaque hemorrhage

LRNC : Lipid-rich necrotic core

PSV : Peak systolic velocity

CCA : Common carotid artery

ICA : Internal carotid artery

ECA : External carotid artery

HU : Hounsfield unit

DAS : Delay and sum

ARFI : Acoustic radiation force impulse

NCC : Normalized cross-correlation

LSQSE : Least squares strain estimator

MW : Measurement window

PVA-C : Polyvinyl alcohol cryogel

NRMSE : Normalized root-mean-square-error

RoCLT : Range of cumulated lateral translation

MaxSCs : Maximum strain curves

MeanSCs : Mean strain curves

DCT : Discrete Cosine Transform

To my family

Acknowledgements

First of all, I would like to thank my research supervisor, Professor Guy Cloutier, who offered me a chance to work in Laboratoire de biorhéologie et d'ultrasonographie médicale (LBUM). His creative opinions and broad knowledge inspired me throughout my research. Without his wise advices and support, I would not finish this thesis. I believe that the scientific rigor and perseverance gained from him will encourage me throughout my career.

I am grateful to Professor Fréderic Leblond, Professor Samuel Kadoury, Professor Siddhartha Sikdar and Professor Alain Vient for kindly accepting as my defense committee members.

Special thanks to Dr. Louise Allard for her support on my study and life.

I also would like to thank Université de Montréal, l'Institut de Génie Biomédical de l'Université de Montréal and Réseau de Bio-Imagerie du Québec for their scholarship support.

Thanks to other coauthors of my papers, Dr. Jonathan Porée, Dr. Marie-Hélène Roy-Cardinal, Boris Chayer, Judith Muijsers, Marcel van den Hoven, Zhao Qin, Professor Gilles Soulez and Professor Richard Lopata for their collaborations and contributions.

I say thank you to previous and present LBUM members. I learned a lot from your expertise. It was my pleasure to work with you.

I especially want to thank some friends who I met in Montréal. Shiming, Meng, Qian, Boxuan, Lei, Shanshan, Wei, Linjiang, Qi, Yu, Huiyang, Shuiling, Huicheng and all others. I really enjoyed the time we spent.

Finally, I would like to thank my family for their unwavering support and endless love. Also, I wish my father could receive my appreciation in paradise for his love. Additionally, I present this work to my upcoming son.

Thank you to all of you.

Chapter 1 : General introduction

1.1 Motivation

Atherosclerosis is a progressive disease affecting large blood vessels such as coronary, peripheral or carotid arteries. It is characterized by the accumulation of lipids and fibrous deposits inside intimal regions of the vessel wall [1]. As the lipid accumulates in the intima, a plaque is gradually formed to induce vessel inward remodeling followed by a decrease of the vessel lumen. As a consequence, the narrowed vessel lumen affects the quantity of blood distributed downstream, and the insufficient supply of blood could lead to ischemic stroke when carotid arteries are considered. On the other hand, the biomechanical instability of a plaque may also induce ischemic complications. Indeed, an unstable (vulnerable) plaque, which is prone to rupture, is characterized by a lipid core and a thin fibrosis cap infiltrated by macrophages [2]. Following rupture, a thrombus may form in the blood stream and when it is detaching of the wall by the flow kinetics, it can migrate and obstacle downstream smaller arteries, causing ischemic stroke.

In current clinical practice, the level of luminal vessel narrowing or stenosis degree is commonly used as an indicator of treatments to prevent stroke. Specifically, patients with mild or moderate stenosis (less than 70% in diameter reduction) are recommended to change lifestyle or take medication. Severe stenoses are treated by carotid endarterectomy or angioplasty. However, the severity of carotid artery stenosis is not sufficient to identify plaques at high risk of rupture. One-third of cryptogenic stroke whose origin is unknown is induced by rupture of non-stenotic but high risk plaques [3]. On the other hand, some patients with a severe stenosis may never experience any symptoms and are thought to have stable plaques [4]. In other words, defining the vulnerability of a plaque is a multifactorial process [5], involving not only the plaque geometry, but also its composition [6]. Thus, comprehensive and early diagnosis of plaque vulnerability has its clinical value for stroke prevention.

Several approaches are currently used to evaluate the atherosclerosis progression. Angiography can detect a stenosis, but it fails to provide information about the content of the plaque. Computed tomography (CT) methods are able to assess the degree of stenosis and the

amount of calcium in the plaque, but accurate identification and quantification of plaque components are challenging because of the limited temporal, spatial, and contrast resolutions. It is also ionizing for patients. Finally, Magnetic resonance imaging (MRI), which is considered the gold standard method to identify lipid-rich tissue, is able to identify vulnerable carotid plaques. But the scan is time-consuming and expensive. Therefore, there is a need to develop a noninvasive, fast and low cost imaging tool to better characterize the plague vulnerability.

Safety, real time and easy accessibility of ultrasound enable it as a method of choice for screening and diagnosis of vascular plaques. Clinically, Doppler imaging is used to evaluate a stenosis using the peak systolic velocity [7]. Indeed, an obstructed vessel results in the acceleration of the blood flow. However, this method cannot provide information on the composition of a plaque. To gain this information, several techniques based on ultrasound echo properties were utilized. Intravascular ultrasound (IVUS) can image the vessel wall and provide volume information of plaques using a catheter with an ultrasound transducer on the extremity, but this technique is invasive. Contrast-enhanced ultrasound (CEUS) is a way to image intraplaque neovessels using microbubbles, which are associated with the growth of plaques. One drawback of CEUS is the injection of contrast agents within the venous system. Another limitation is that it is still insufficient to detect the lipid core and fibrosis cap of a vulnerable plaque.

Ultrasound elastography or strain imaging, a method first introduced by Ophir *et al*. [8] in 1991, is a technique that measures the strain or relative elasticity of biological tissues,. An external compression is applied on a tissue and its displacements responding to the stress are measured with a tracking method. Strains can be obtained from the spatial derivation of displacements. In the late nineties, elastography was explored to characterize the vessel wall with IVUS images. The natural cardiac pulsation or the inflation of a compliant balloon on a catheter was used by de Korte *et al*. [9] to differentiate the coronary calcified plaque component (less strain) from non-calcified tissues (higher strain) *in vivo.* However, IVUS elastography is invasive, which restricts it to be a complementary tool of B-mode IVUS for assessing vascular plaques. In 2004, noninvasive vascular elastography (NIVE) was proposed to show the potential of determining the stability or vulnerability of a plague using ultrasound imaging [10]. NIVE could determine the strain field of the moving vessel wall of a superficial artery (*e.g*., carotid)

caused by the natural cardiac pulsation without the need of an external compression. Due to Young's modulus differences among different vessel tissues, a lipid pool, a calcified and a normal tissue made of collagen and elastin are expected to present different strains under the blood pressure stress activation.

Currently, sub-optimum performance and computational efficiency limit the clinical acceptance of NIVE as a fast and efficient method for the early diagnosis of vulnerable plaques. Specifically, NIVE with a cross-sectional view of the vessel is challenging because the motion perpendicular to the ultrasound beam, namely the lateral motion, is difficult to track because of the limited lateral resolution of ultrasound images and the absence of phase information in that direction. To improve the estimation performance of NIVE, developments of new strain algorithms and advanced ultrasound image reconstruction methods were made.

To improve lateral strain estimation, Konofagou *et al*. [11] proposed to perform interpolation between adjacent radiofrequency (RF) A-lines. A one-dimensional (1-D) cross-correlation based method was used to obtain high precision lateral displacements [12]. The main disadvantage of this 1-D method is that the accuracy of the lateral displacement estimation is lower by an order of magnitude, compared with the axial displacement estimation, because of differences between lateral and axial resolutions. To avoid noisy lateral estimation, the spatial angular compounding strategy was proposed to reconstruct radial and circumferential strains using only accurate axial estimations at several steering angles [13-15]. However, these approaches compute strains from displacement derivatives, which enhances variance of strain estimations due to associated high frequency displacement noise. To circumvent this issue, an alternative strategy is the affine model-based estimation, which derives all strain components, such as axial, lateral and shear strains, directly without derivative operations [16-18]. Nevertheless, lateral strain estimation is still not reliable using these affine models [19].

Advanced ultrasound beamforming methods could also improve lateral strain estimation. Korukonda and Doyley demonstrated that synthetic aperture imaging enhanced lateral displacement estimation with a cross-correlation based method [20, 21]. Coherent plane wave compounding (CPWC) beamforming was also proposed to obtain superior lateral strain estimation with the model-based Lagrangian speckle model estimator (LSME) [18]. Recently, a transverse oscillation (TO) beamforming strategy provided improved lateral displacement

estimations for vascular and cardiac applications [17, 22]. In the context of cross-sectional NIVE, however, the performance of model-based strain estimators considering advanced beamforming, such as CPWC and TO imaging, has not yet been studied.

Another important challenge for strain estimation is the inherent issue of out-of-plane motion. During 2-D ultrasound acquisitions, out-of-plane motions that are perpendicular to the imaging scan plane are not considered, consequently they may impact the reliability of NIVE because vascular wall motions are three-dimensional (3-D). The magnitude of out-of-plane motions is hypothesized to induce strain estimation artifacts due to reduced image correlation. Based on simulations, Fekkes *et al*. [23] demonstrated that a 3-D cross-correlation based strain estimator outperformed 2-D methods when large out-of-plane motions were considered. A similar conclusion was made by Brusseau *et al* [24]. In that latter study, a multi-row probe was devised to achieve multi-plane acquisitions. A maximum out-of-plane motion of 0.8 mm was considered using a breast mimicking phantom and a 3-D search scheme. However, to our knowledge, there has been no study on the influence of out-of-plane motions for NIVE using *in vitro* and *in vivo* clinical dataset. Moreover, an evaluation framework to determine the impact of out-of-plane motions on the performance of estimation methods is a necessity for clinical 2-D NIVE.

The computation efficiency is another issue that needs to be addressed. Most strain estimation algorithms are window-based. Specifically, pre-and post-motion images are divided into overlapping windows. Then, cross-correlation [14, 21] or affine [18, 25] estimations are performed within each window. To solve the whole motion field, motion parameters of each window are estimated successively. However, there is always a trade-off between the window size, window overlapping and computation efficiency. Larger windows and overlaps result in more accurate motion estimation with higher spatial resolution, but at a cost of a higher computation time. Low computation efficiency may limit NIVE for clinical screening and characterization of vulnerable plaques. To reduce computation, a global estimation strategy could be an option. Some global approaches, such as the Horn-Schunck (HS) optical flow algorithm [26], consider all pixels inside a region of interest (ROI) to solve a dense motion field globally. Those schemes usually require to optimize iteratively a cost function until convergence and may still be computationally intense. Recently, an effort was made to convert an iterative

optimization process into a least squares scheme to obtain analytic solutions of the Doppler vector domain [27]. The impact of this idea on improving computation efficiency deserves to be investigated for NIVE.

1.2 Objectives

The procedure to perform NIVE analysis consists in image formation and image post-processing steps. Specifically, image formation, also called beamforming, is a process to transmit and receive ultrasound echoes and to reconstruct images using reflected signals from moving vessels. Thereafter, using a technology of motion tracking, the image post-processing allows to compute the motion or strain field of vessel walls from reconstructed images. This thesis aims to improve the accuracy of these two aspects of NIVE to facilitate predicting carotid plaque vulnerability.

First of all, regarding image formation, conventional line-by-line focused imaging is the technique implemented on most scanners for clinical examination. Emerging imaging modalities, such as plane wave imaging, are promising to enhance image quality. Some other specific imaging technologies, such as transverse oscillation beamforming, were proven efficient for motion tracking due to enriching lateral phase information. This approach may thereby improve the performance of ultrasound elastography. Therefore, the first objective of this thesis was to introduce these novel imaging approaches into NIVE. The advantages of advanced imaging methods coupled with model-based strain estimators are expected to improve NIVE performance.

Secondly, during the acquisition of ultrasound RF signals for image formation, the carotid artery is deformed in 3-D. When performing 2-D NIVE, we assume that the carotid artery is only moving in a 2-D scan plane. Thus, 2-D NIVE suffers from the influence of out-of-plane motions. The next objective of this thesis was to investigate the influence of out-of-plane motions on the performance of 2-D NIVE. This knowledge could give new guidelines for the clinical use of NIVE.

Finally, regarding image post-processing, NIVE algorithms need to estimate strains of vessel walls from reconstructed images with the objective of identifying soft and hard tissues.

Although a large amount of strain estimation algorithms have been proposed, a strain estimator that is able to determine subtle structures inside a carotid artery is still needed. Therefore, the third objective of this thesis was to develop a strain estimation algorithm with a high resolution as well as a high computation efficiency.

1.3 Thesis plan

This thesis consists of eight chapters. Beside the present introduction (**Chapter 1)** that gives the motivation and objectives of this work, **Chapter 2** presents the pathophysiology of carotid atherosclerosis, including its causes and symptoms. It also introduces diagnosis tools to characterize carotid plaques. **Chapter 3** presents the basic principles of ultrasound image formation and undertakes a literature review of emerging ultrasound imaging modalities, whereas **Chapter 4** provides a state of the art introduction to ultrasound elastography and, especially, details of approaches used for NIVE. **Chapter 5** consists in the first article of this thesis, which applied plane wave and transverse oscillation beamforming into the image formation to evaluate NIVE performance with two strain estimation algorithms. **Chapter 6** is the second article of this thesis, which established a framework for evaluating out-of-plane motions and discussed the influence of such artifact motions on NIVE performance. **Chapter 7** includes the third article of this thesis, which aims to fulfill our third objective. A strain estimation algorithm based on a sparse model is proposed to reconstruct a dense strain field with pixel-wise resolution as well as a high computation efficiency. Finally, **Chapter 8** discusses originalities and limitations of my doctoral works, concludes the whole three projects and gives future perspectives.

Chapter 2 : Atherosclerosis

2.1 Atherosclerosis pathogenesis

Atherosclerosis is a vascular disease that affects artery walls (by thickening) and lumens (by plaque formation). Before introducing the method of diagnosis and the characterization of the vulnerability of the plaque, it is worthwhile to better understand its pathogenesis.

A healthy artery wall consists of three layers: tunica intima, tunica media and tunica adventitia, as shown in figure 2.1(A). The tunica intima, commonly called the intima, is the innermost layer, mainly made up of a single layer of endothelial cells. It is a permeable barrier that performs the exchange between the blood and the artery wall. The tunica media is the middle layer and normally the thickest part of the artery wall. Smooth muscle cells, its primary component, regulate dilation and compression of the artery. The outermost layer, the tunica adventitia, consists of collagenous and elastic fibers. This layer helps the artery to attach with surrounding tissues.

The exact mechanism of the pathogenesis of atherosclerosis is still not clearly understood. However, a widely acceptable theory on the cause of atherosclerosis is a response to an injury, as shown in figure 2.1(A). This theory claims that atherosclerosis is initiated by subtle physical devastation of endothelial cells due to some risk factors (*e.g.*, hypertension, diabetes, infections, etc...). This injury process provokes an inflammatory response as monocytes adhere to the damaged endothelial layer and then entered beneath, which induces thickening of the intima. As proliferation of low-density lipoproteins (LDL) goes on at the site of the injury, monocytes would differentiate into macrophages and start to ingest LDL, which would induce intimal thickening. The macrophages containing LDL, also referred to as foam cells, are the main part of the fatty streak, as shown in figure 2.1(B). These fatty streaks are asymptomatic and consist in the precursor stage of atherosclerosis. Over time, foam cells die and lipids gradually accumulate into the endothelial layer. This could cause the formation of a fibrous plaque with a lipid-rich necrotic core and an overlying collagen cap.

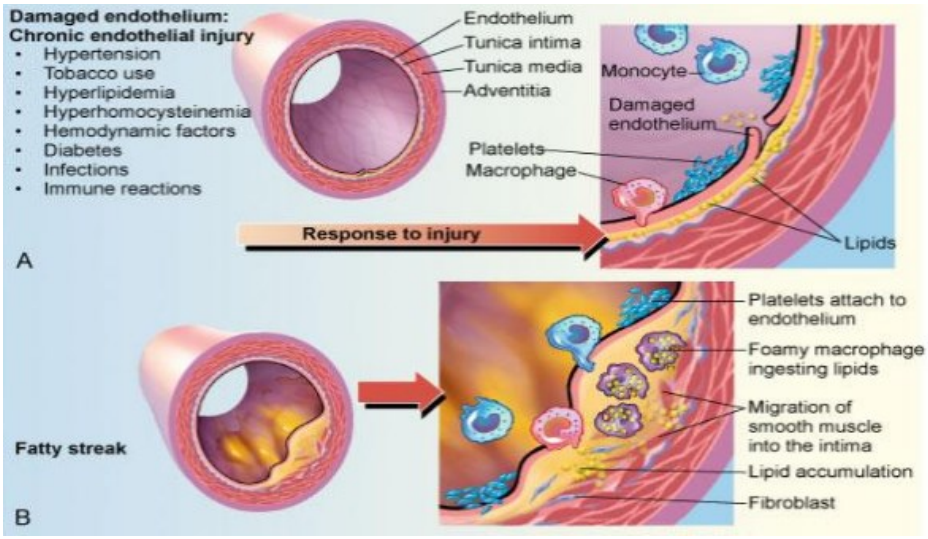

Figure 2.1 Atherosclerosis pathogenesis. Damaged endothelium (A). Fatty streak formation (B). Adapted and modified from [28].

2.2 Atherosclerosis progression

The atherosclerotic disease is progressive; it can start in the childhood and progress silently through the elderly. Its pathologic features include three stages corresponding to early, intermediate and advanced lesions defined by the American Heart Association (AHA) [29]. A summary of atherosclerosis progression phases is shown in figure 2.2, in which 6 types of lesions are classified. Initial lesions (type I) and fatty streak lesions (type II) are early lesions, where intimal thickening and intracellular lipid accumulation happen. Type III lesions correspond to an intermediate stage, as shown in figure 2.3(c), where some small pools of extracellular lipid appear in this stage. Type IV lesions (atheroma) represent the first phase of advanced lesions. It arises from the formation of lipid cores as more lipids accumulate (figure 2.3(d)). Type V lesions, referred to as fibroatheroma (figure 2.3(e)), are different from type IV lesions, as a fibrous cap covering a lipid core is formed. The fibrous cap is made of smooth muscle cells and infiltrated by varying amounts of macrophages and lymphocytes [30]. Type VI lesions could be described as the disruption state of type IV and V lesions surface [30]. They not only have the morphology of type IV or V lesions, but they also present surface fissures and/or hemorrhage/hematoma of lesions and/or thrombi (figure 2.3(f)).

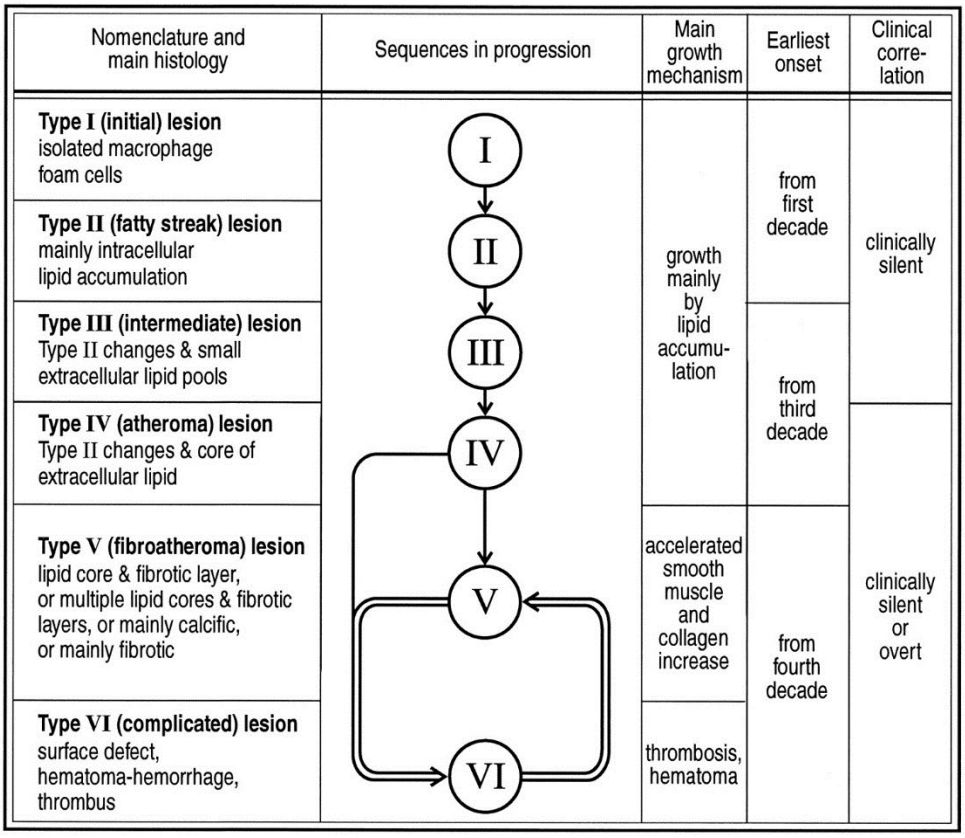

Figure 2.2 AHA classification of atherosclerotic lesions. Flow chart in the second column presents the progression of atherosclerotic lesions. Roman numbers indicate lesion types which are described in the first column. The loop between types V and VI clarifies how lesions are enlarged when thrombi deposit on their surfaces repeatedly. Adapted from [29].

2.3 High-risk plaque description

Thrombosis accompanying plaque rupture is one of the major cause of ischemic stroke in patients with carotid artery atherosclerosis [31]. It is shown that the risk of stroke is annually less than 1% when asymptomatic patients have a stenosis less than 75%, while the risk is increased to 2% - 5% for those with one higher than 75% [32, 33]. For symptomatic patients with severe stenosis ($\geq$ 70%) who suffered from transient ischaemic attacks previously, the risk rises up to 10% for the first year and goes much higher to 30%-35% in the next five years [33, 34].

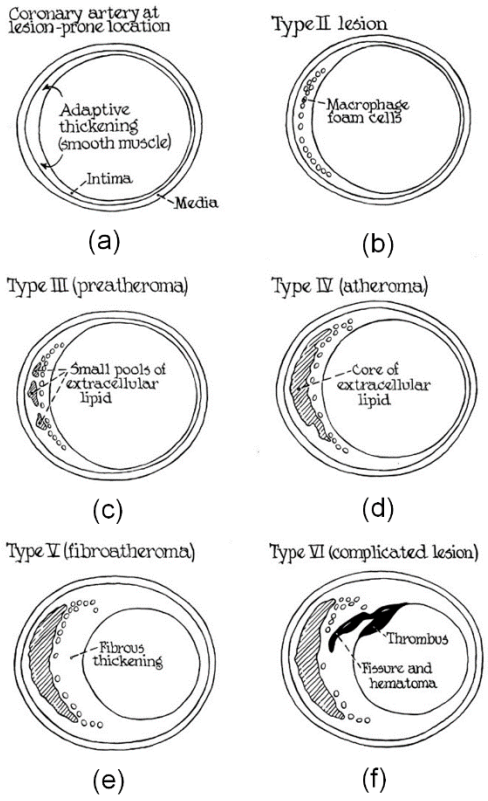

Figure 2.3 Diagram of cross-sectional morphology of AHA lesion classification. Adapted and modified from [29].

However, the risk of lesion rupture is not only associated with the size of the lesion, but also with its morphology [35, 36]. A typical morphology of a lesion with a high risk of rupture, also named a vulnerable plaque, is presented in figure 2.4. A vulnerable plaque is characterized by a thin fibrous cap and a large lipid-rich necrotic core (LRNC). The overlying thin fibrous cap is infiltrated by macrophages with few or absence of smooth muscle cells [37]. The thicknesses of the thin fibrous cap of vulnerable carotid plaques vary from 80 μm – 460 μm depending on different measurement modalities, including optical coherence tomography (OCT) [38], sonography [39] and post-mortem histopathology [40]. Fissures and ruptures on the thin cap would lead to total disruption of the fibrous cap [35], exposing then the lumen to thrombogenic substances underlying the lipid core [35].

Another main ingredient of a vulnerable plaque is the LRNC that is considered as soft tissues. A large LRNC was identified as a strong predictor of vulnerable plaque fissures [41]. A prevalence study proved that a plaque without intraplaque hemorrhage (IPH) where the LRNC

accounts for more than 40% of the plaque area can be considered as a high-risk lesion [42]. Moreover, in a small clinical trial of 37 patients with carotid stenosis larger than 70%, patients with a LRNC were more often symptomatic than asymptomatic [43].

Intraplaque hemorrhage (IPH) is commonly seen in advanced lesions and it is associated with carotid plaque progression [44, 45]. It arises from the disruption of microvessels which could be introplaque neovasculars that stem from tunica adventitia. There is evidence to prove that repeated IPH is contributing to the LRNC expansion [46]. In [47], it was reported that the incidence of IPH in symptomatic patients was 84%, which is much higher than the occurrence of 56% in asymptomatic patients.

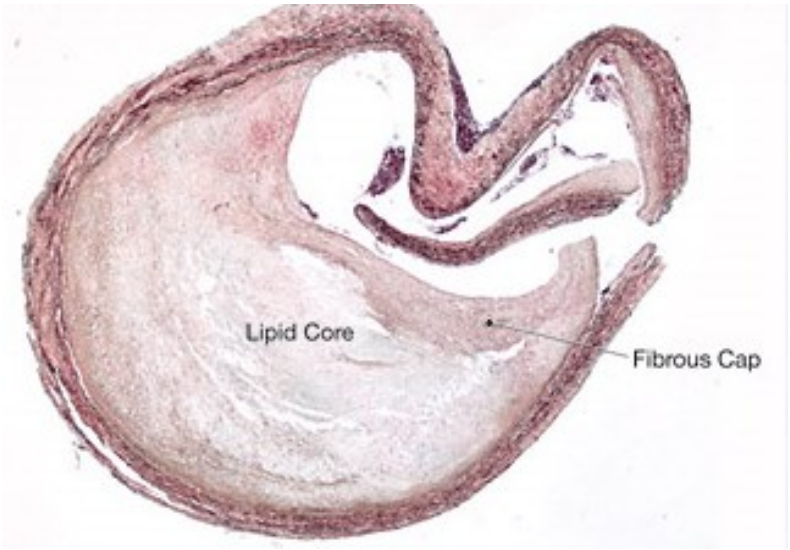

Figure 2.4 Micrograph of a carotid plaque from an asymptomatic patient. A large lipid core and a thin fibrous cap are presented. Adapted from [31].

2.4 Imaging modalities

There is a strong clinical interest in imaging plaques and assessing its vulnerability, particularly for asymptomatic patients. Identifying the content of the plaque would help to predict its rupture, determine the treatment and prevent stroke. For symptomatic patients who are taking medications, imaging follow-up of plaques is necessary to evaluate treatments and monitor the evolution of lesions. This section gives a brief review of imaging modalities of carotid plaques. Firstly, some invasive technologies, such as angiography, intravascular ultrasound and optical coherence tomography, are introduced. Then, B-mode ultrasound, Doppler ultrasound, CT and

MRI, which are noninvasive imaging modalities, are reviewed briefly. Finally, other recent and novel imaging methods are discussed.

2.4.1 Angiography

Digital subtraction angiography (DSA) is a reference standard to assess stenosis severity of an artery. During the intervention, a contrast medium is injected through a catheter that allows to see the vessel architecture. The pre-contrast and post-contrast X-ray images are subtracted to highlight opacified lumens. Then, DSA enables to observe and measure accurately the lumen stenosis. However, it does not allow to see plaque components. Moreover, it is invasive and has ionizing radiation, which could induce some complications, such as stroke when the catheter detaches a portion of the plaque unintentionally. In addition, it not suitable to patients who are allergic to iodic-based contrast agents. An example of DSA of a carotid artery is shown in figure 2.5.

Figure 2.5 DSA image of a carotid internal artery with a severe stenosis. Adapted and modified from [48].

2.4.2 Intravascular ultrasound (IVUS)

IVUS is an invasive imaging technology using a catheter with an ultrasound transducer to give a cross-sectional visualization of a plaque. Like ultrasound B-mode imaging, IVUS is able to provide anatomical information, such as lumen stenosis, eccentric patterns, echolucent lesions, and to a lesser extent information on plaque composition, such as calcification [49].

Conventional IVUS with 20 to 40 MHz transducers provides axial resolution of 70 – 200 μm, lateral resolution of 200 – 400 μm and an imaging depth of 5 – 10 mm [50-52]. One limitation of IVUS is that its resolution is insufficient to distinguish the thin fibrous cap whose thickness is usually less than 65 μm. Better axial resolution with 40 μm can be achieved with a 60 MHz transducer (Kodama, ACIST Medical Systems), while imaging depth was reduced accordingly. Recently, higher frequency IVUS transducers operating at 90 – 150 MHz have been developed to counter this problem [52]. The axial resolution can reach 50 μm and below. However, clinical studies are still needed to validate these new technologies. Figure 2.6 shows an IVUS image of a carotid artery with a plaque.

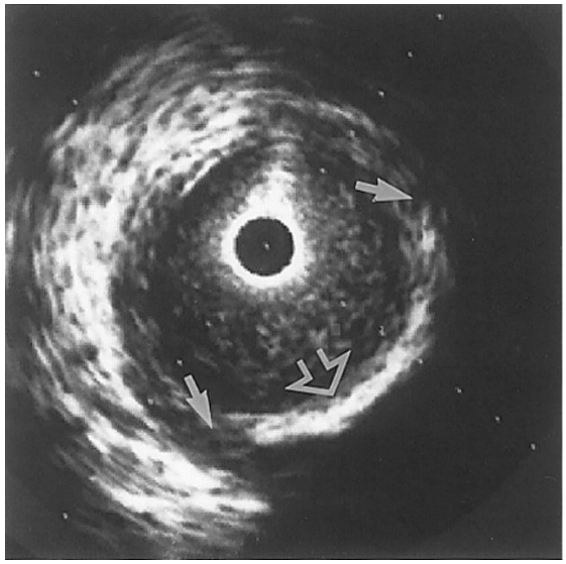

Figure 2.6 An IVUS image of an internal carotid artery acquired by a 30 MHz transducer. A hyperechoic region (open arrow) suggests a calcification. Hypoechoic plaque is seen at the shoulder of the lesion (short arrows). Adapted and modified from [53].

2.4.3 Optical coherence tomography (OCT)

OCT is a high resolution imaging method whose axial resolution is 4 – 20 μm. Its principle is like ultrasound imaging and allows to measure echo time delay and intensity of light scatterers. However, light velocity is much higher than sound speed. One uses low-coherence interferometry to measure the echo time delay indirectly because of such a high speed. The intensity of the backscattered light is recorded to produce a two-dimensional (2-D) image of optical scattering. Due to the superior spatial resolution, OCT is advantageous to measure the

thickness of a thin fibrous cap for vulnerable plaque characterization. However, the imaging depth of OCT is limited (2 – 3 mm) due to the limited penetration of light. Another promising finding is that OCT is able to identify macrophages in fibrous caps (figure 2.7), which suggests that it could be useful to characterize different features of vulnerable plaques [54].

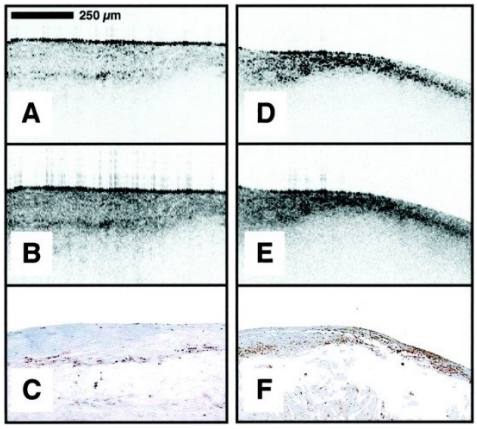

Figure 2.7 Raw (A), logarithm (B) OCT and histology (C) images of a fibroatheroma with less macrophages in the fibrous cap. Raw (D), logarithm (E) OCT and histology (F) images of a fibroatheroma with more macrophages in the fibrous cap. Adapted from [54].

2.4.4 Noninvasive vascular ultrasound

Noninvasive vascular ultrasound and more specifically, B-mode ultrasound, allows the evaluation of superficial arteries. For carotid plaque imaging, it permits to identify plaque morphology including size, texture and echogenicity in real time. In addition, it provides the measurement of the intima-media thickness, which is recognized as a marker of early atherosclerosis [55]. It is also sensitive to plaque calcification detected by the hyper-echogenicity from calcification spots. However, B-mode ultrasound only presents the morphology of a plaque in terms of echo brightness, which may not be sufficient to distinguish plaque components and tell us about its vulnerability.

2.4.5 Doppler ultrasound

Color Doppler is a noninvasive imaging method to assess the stenosis degree although its spatial resolution is less than DSA. In addition, Doppler provides blood flow velocity, which is a diagnosis indicator of stenosis degrees, but its measurement is affected by imaging angles, inter-observer discrepancy and shadow artifact due to calcification [35]. The peak systolic

velocity (PSV) is recommended for the diagnosis of carotid stenosis. Specifically, a 50%-69% stenosis of the internal carotid artery (ICA) is identified when PSV is 125-230 cm/sec [7]. When the PSV is more than 230 cm/sec, the stenosis is viewed as being more than 70% [7]. Coupling ultrasound B-mode and Doppler imaging, the carotid duplex imaging mode is a first-line examination for carotid atherosclerosis. A carotid duplex image showing a plaque in the ICA is presented in figure 2.8.

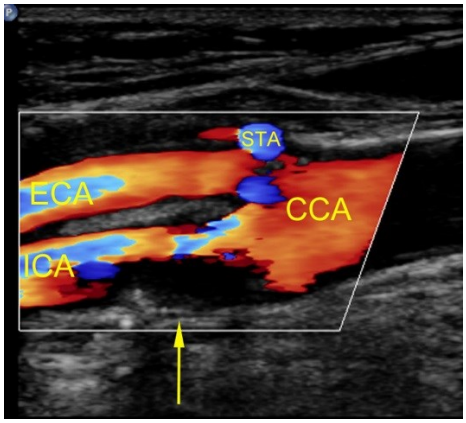

Figure 2.8 An echolucent plaque indicated by the yellow arrow causing 70% stenosis. ECA = external carotid artery, ICA = internal carotid artery, CCA = common carotid artery, STA = superficial temporal artery. Adapted from [56].

2.4.6 Computed tomography (CT)

A CT scan provides slice data according to Hounsfield unit (HU) values as different tissue presents varied X-ray attenuation. Calcifications with higher HU values are prone to be identified during a CT scan, which overcome shadow artifacts of large calcifications for B-mode imaging. The spatial resolution of CT scan is on the sub-millimeter range, which suggests the possibility to differentiate plaque components, such as fatty, mixed and calcified tissues [57] whose HU values are respectively less than 60 HU, between 60 and 130 HU and larger than 130 HU [58]. Figure 2.9 shows a plaque component analysis using CT scan. In addition, it was reported in [59] that there is high positive relationship between plaque lipid volume and the presence of ulceration. Thanks to slice scan imaging and developed software toolkit for image reconstruction, CT can obtain total volume of plaques and volume of subcomponents of plaques according to HU thresholds. CT imaging mainly has two limitations. Firstly, CT plaque imaging

is irradiative. Secondly, although CT plaque imaging has high imaging contrast for calcifications, the imaging contrast of fatty tissues is limited.

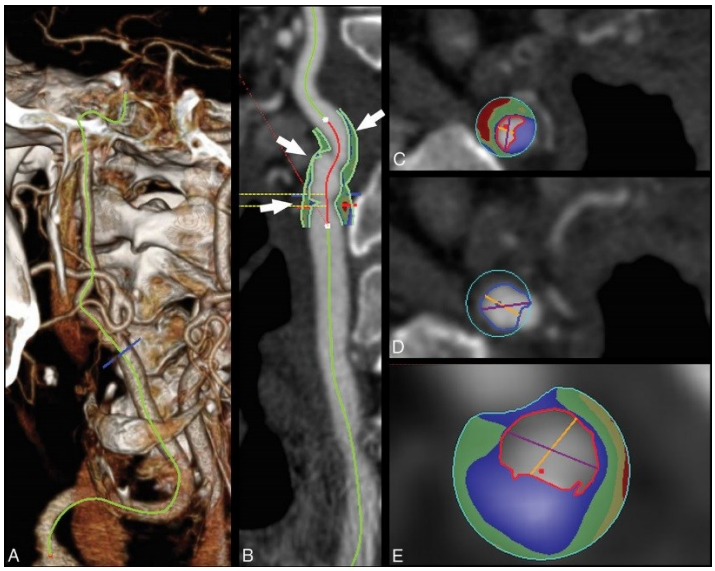

Figure 2.9 Plaque component analysis of a 75-year-old man with a transient ischemic attack using CT image reconstruction software. Volume-rendered image where the carotid artery is traced (A). Reconstruction post-processed image (B). Plaque cross-sectional identification positioned in (B), as indicated by white arrows (C), (D) and (E), where the lumen is indicated by a red contour, the lipid component by the red color, mixed tissues in green and calcium in blue. Adapted from [57].

2.4.7 Magnetic resonance imaging (MRI)

MRI is a non-invasive and nonradioactive imaging method, which allows to identify not only the stenosis degree, but also to evaluate plaque components. One superior advantage of MRI over other imaging modalities is its ability to detect the presence of IPH. A hemorrhagic plaque presents a higher intensity in T1-weighted MRI. To detect LRNC and the fibrous cap of a vulnerable plaque, contrast-enhanced T1-wighted MRI was introduced [60]; it requires using a contrast agent and dedicated carotid coils. One case showing a LRNC and a fibrous cap with a 1.5-Tesla scanner is presented in figure 2.10. Although MRI is currently considered the best modality to characterize a vulnerable carotid plaque, there are some limitations. One important limitation is the side effect of contrast agents, which makes patients with a decreased renal function ineligible. The other limitation is that the scan time is time-consuming due to complex procedures, which also leads to a high cost and less equipment availability.

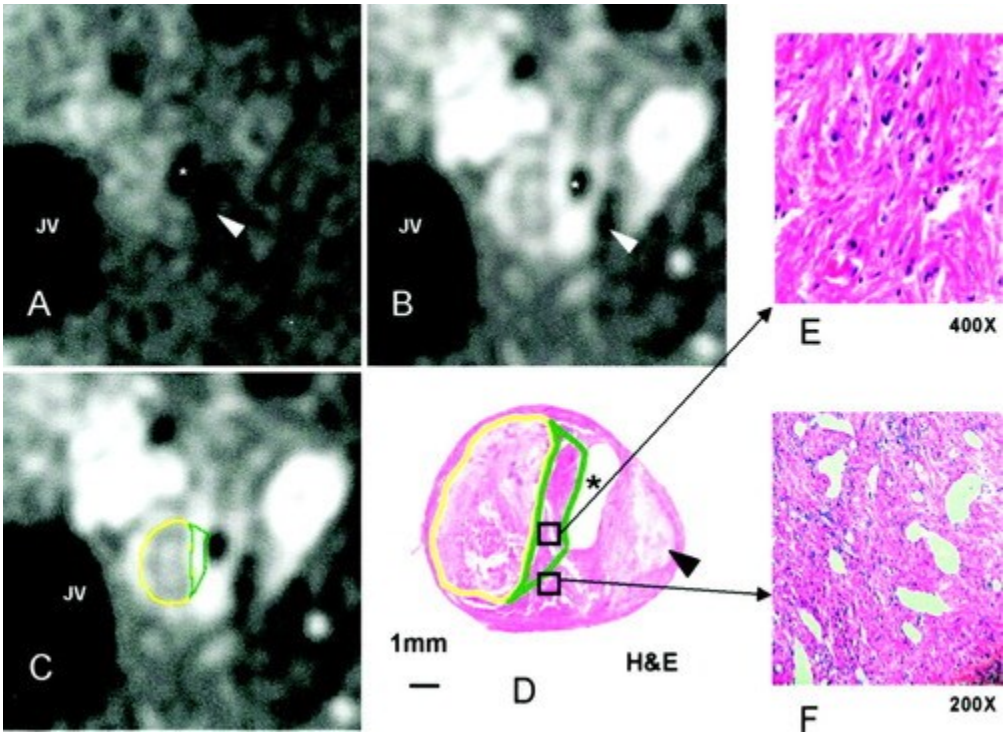

Figure 2.10 Pre-contrast T1-weighted image (A), post-contrast T1-weighted images (B, C). Histological image (D) indicating the fibrous cap by the green contour and LRNC by the yellow contour. Micrographs regarding regions in (D) that are showing a strong contrast enhancement (E, F). Adapted from [60].

2.4.8 Other novel imaging modalities

Contrast-enhanced ultrasound (CEUS) is an imaging technique for visualizing vessels using micro bubbles. Flowing micro bubbles inside vessels resonate when they are exposed to acoustic waves, which leads to ultrasound signal enhancement. The enhanced regions not only help better identifying the vascular lumen, but also provide a visualization of intra-plaque neovascularization, which is associated with plaque growth [61-63]. However, more clinical validations are needed for reproducibility and clinical utility of the approach [57, 64].

Positron emission tomography (PET) and single photon emission computed tomography (SPECT) are nuclear functional imaging techniques that monitor metabolic disorders. The most common application of PET/SPECT into assessing atherosclerotic plaques is to quantify plaque inflammation using a radiotracer based on ^{18}F-fluorodeoxyglucose (FDG). Accumulated macrophages within an inflammatory region of an atherosclerotic plaque would metabolize FDG, which makes uptake of FDG be an indicator of plaque inflammation. One limitation of

PET/SPECT with FDG is their low spatial resolution (4 – 5 mm for PET and 1 – 1.6 cm for SPECT) [49, 65, 66]. The other is its radiation and high cost.

Near-infrared fluorescence (NIRF) imaging is a molecular imaging technique without radiation. Fluorescent contrast agents, such as fluorophores, are excited by near-infrared wavelengths (700-900 nm). When the excited state of fluorophores is relaxed to a low energetic state, the generated fluorescence light is acquired to reconstruct 2-D images. A recent study found that proteolytic enzymes might be associated with fibrosis cap erosion promoting plaque rupture [67]. Using gelatinase-activated or cathepsin-B-sensitive probes, NIRF is able to identify the proteolytic activity of a vulnerable plaque [67-69]. However, NIRF is now used only in animal or pre-clinical studies. Performing a large study validation with patients is needed.

Non-invasive ultrasound elastography has been proposed to characterize plaques of carotid arteries. It captures deformations of vascular walls induced by the blood pressure pulse using motion estimation algorithms, from which the estimated strains allow to differentiate a soft LRNC (large strain) and hard calcification spots (small strains). An example of non-invasive ultrasound elastogram is shown in figure 2.11.

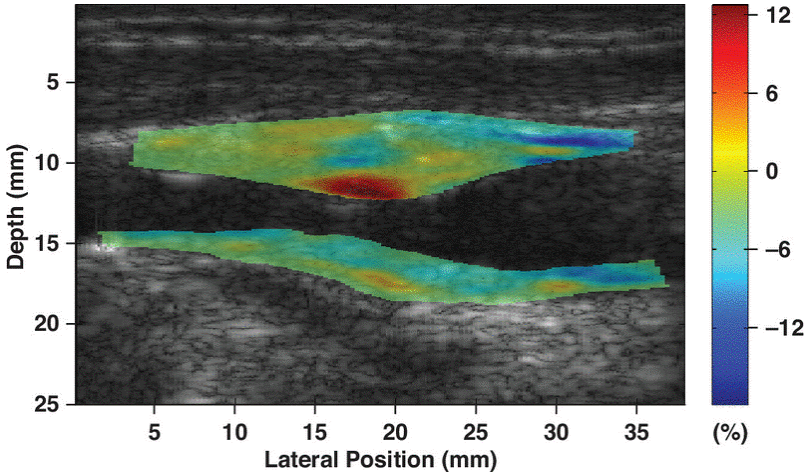

Figure 2.11 Shear strain elastogram of a plaque with 60% stenosis of internal carotid artery in a cross-sectional view. Adapted from [70].

2.5 Summary

Atherosclerosis is a complex vascular disease. It could begin in childhood without symptoms and develop silently until the first cardiovascular event in the elderly. Despite many imaging modalities being available for research and clinical use (see Table 2-1), the early diagnosis of atherosclerosis, especially for vulnerable plaques, is still challenging.

Table 2-1 Comparison of imaging modalities

Imaging modalities	Diagnosis criteria	Limitations
Angiography	Lumen stenosis	Ionizing radiation, invasive
IVUS	Anatomical information and calcification	Invasive
OCT	Fibrous cap	Low penetration depth (2 – 3 mm)
Ultrasound	Plaque morphology and calcification	Insufficient to detect other plaque components
Doppler	Lumen stenosis	Insufficient to detect other plaque components
CT	Calcification and plaque volumn	Ionizing radiation
MRI	Lipid core and intraplaque hemorrhage	Injection of contrast agents, time-consuming and expensive
CEUS	Neovascularization	Injection of micro bubbles
PET/SPECT	Plaque inflammation	Low resolution, radiation and expensive
NIRF	Fibrous cap	Injection of Fluorescent contrast agents
Elastography	Lipid core and calcification	Low resolution and computation time

Although MRI is currently considered as the reference modality to characterize a vulnerable carotid plaque, it is not feasible for early screening of asymptomatic peoples and clinical routine diagnosis of symptomatic patients due to its high cost, long acquisition time and

less equipment availability. For follow-up of patients with atherosclerosis during treatments, invasive and/or ionizing radiative imaging modalities, such as IVUS, CT, angiography, are also better to be avoided.

Ultrasound is a safe (non-invasive, nonradioactive) and real time imaging method for assessment of biological tissues. It is of value, especially noninvasive vascular ultrasound, for early screening and diagnosis of atherosclerosis due to its low cost and high clinical availability. Despite the fact that current non-invasive vascular ultrasound does not have the same tissue sensitivity as MRI for vulnerable plaque characterization, non-invasive ultrasound elastography would be a competitive way to characterize components of vulnerable plaques, such as LRNC, by measuring biomechanical properties. Therefore, this thesis is focusing on vulnerable carotid plaque characterization using non-invasive ultrasound elastography.

In the following two chapters of this thesis, physical principles of medical ultrasound imaging as well as a literature review on imaging beamforming methods are presented in Chapter 3. Chapter 4 introduces fundamental principles of quasi-static elastography and present a literature review on non-invasive vascular ultrasound elastography.

Chapter 3 : Medical ultrasound imaging

3.1 Principles of ultrasound image formation

The pulse-echo technique is the basis of ultrasound imaging. Specifically, an electrical pulse is converted into ultrasound waves by an ultrasonic transducer. Then, echoes from tissue reflection and scattering are collected by the same transducer and post-processed into a display format. Different post-processing techniques are used, either based on echo intensities or frequencies. Final display formats are classified into gray-scale and Doppler imaging modes. Doppler imaging is mostly used to measure the velocity of blood flow.

3.1.1 Gray-scale imaging modes

When ultrasonic waves travel in a homogeneous medium, they will continue propagating in the same direction without energy loss. When ultrasonic waves come across the interface of two different tissues, propagation of ultrasonic waves depends of the tissues' acoustic impedance $Z = \rho \times c$, where ρ is the tissue density and c is the speed of sound. In fact, the ultrasonic waves will be reflected in part at the interface and the rest will be transmitted into the next tissue. The amount of reflection is determined by reflection coefficient R:

$$R = \frac{(Z_1 - Z_2)^2}{(Z_1 + Z_2)^2}, \tag{3.1}$$

where Z_1 and Z_2 are acoustic impedances of the two tissues respectively. The larger the difference of acoustic impedances of two tissues, the larger the amplitudes of echoes by reflection will be. Normally, the differences in acoustic impedance of soft tissues are not significantly large, which ensures the amount of reflected energy from a tissue interface is small, allowing ultrasound to carry more energy through the next tissue. Finally, the echoes from the tissues inside an insonification area are acquired by an ultrasound transducer to form an image.

When an ultrasonic wave is transmitted by a transducer, the echoes are received and converted into radiofrequency (RF) signals by the piezoelectric effect of the same transducer. RF signals can be displayed in different modes (see figure 3.1). Amplitude mode (A-mode) is to display echo envelop amplitudes from different tissue interfaces as a function of receiving

time. One axis shows amplitude information. The amplitude spikes represent the amplitudes of echoes by reflection. The other axis displays imaging depth information. Brightness mode (B-mode) is an alternative way that displays echoes. Each amplitude of echo in A-mode is modulated into image intensity of a pixel in a gray level image where the pixel brightness is proportional to the amplitude of echo. When ultrasonic waves are transmitted by several elements, the received A-mode scan lines are combined and converted into brightness spots in B-mode imaging. Sweeping the region of interest of a tissue using several transmissions, a 2-D B-mode image is formed, whose lateral and axial directions represent the 2-D tissue dimension, respectively. Motion mode (M-mode) is to track motions of a certain position along time. One axis displays time information. The other axis shows amplitudes or brightness variance in terms of time. As shown in M-mode imaging, a static object displays a straight line, while a moving object shows a profile of oscillations.

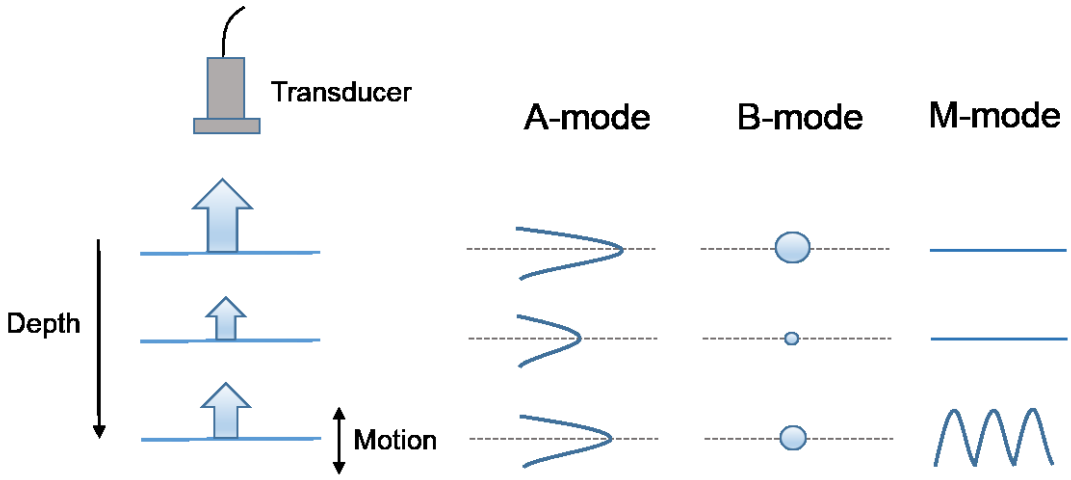

Figure 3.1 Gray-scale imaging modes. Display examples of A-mode, B-mode and M-mode with respect to static and moving objects.

Both B-mode and M-mode are able to track tissue motions. An advantage of B-mode is that it can show a 2-D view of tissues. Current ultrasound elastography techniques are mainly based on 2-D ultrasound images, which are detailed in the next section.

3.1.2 Line-by-line focused imaging

Line-by-line focused imaging is the most widely used approach in modern ultrasound scanning systems (see figure 3.2). To form a 2-D image, a combination of elements of a

transducer transmits a focused ultrasound beam into an imaged area. Then, the echoes are received by the same transducer to build a scan line in the reconstructed image. By sweeping ultrasound beams across the imaged area sequentially, a full image delineating tissues within the imaged area is reconstructed.

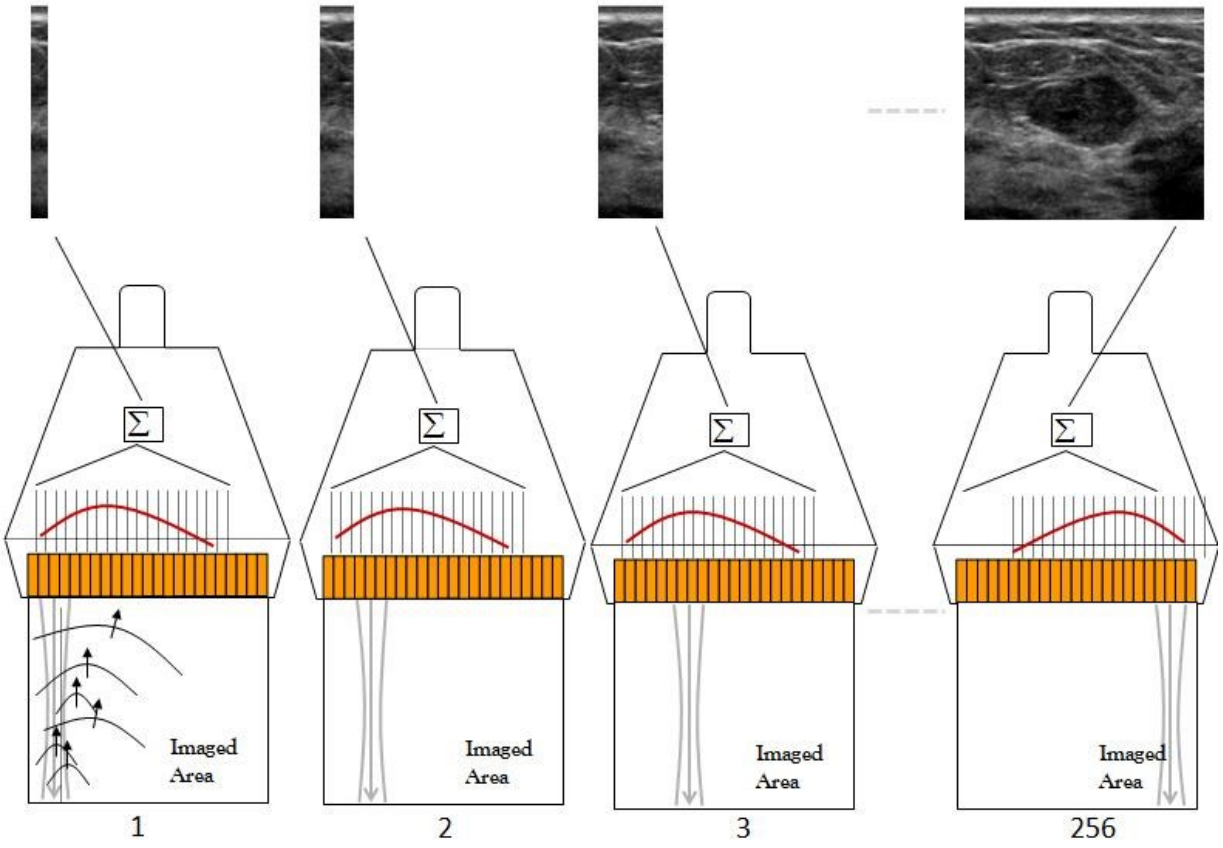

Figure 3.2 An image formation process using line-by-line focused imaging. The number of scan lines for one image is typically 256. Adapted from [71].

The reconstruction time of one image using line-by-line focused imaging depends on the number of scan lines and the imaging depth. For a given maximum imaging depth, D_{depth}, the travelling time of an ultrasonic wave for one scan line is

$$t_{line} = \frac{2D_{depth}}{c}, \tag{3.2}$$

where c is the speed of ultrasound in soft tissues, which is assumed to be constant at 1540 m/s. Multiplying by 2 is to consider the round trip of ultrasonic wave travelling. If we want to build an image with 256 scan lines for an imaging depth of 5 cm, the construction time is $256 \times t_{line}$,

which is about 16.6 ms. Under this condition, the frame rate is about 60 Hz, which allows real time imaging.

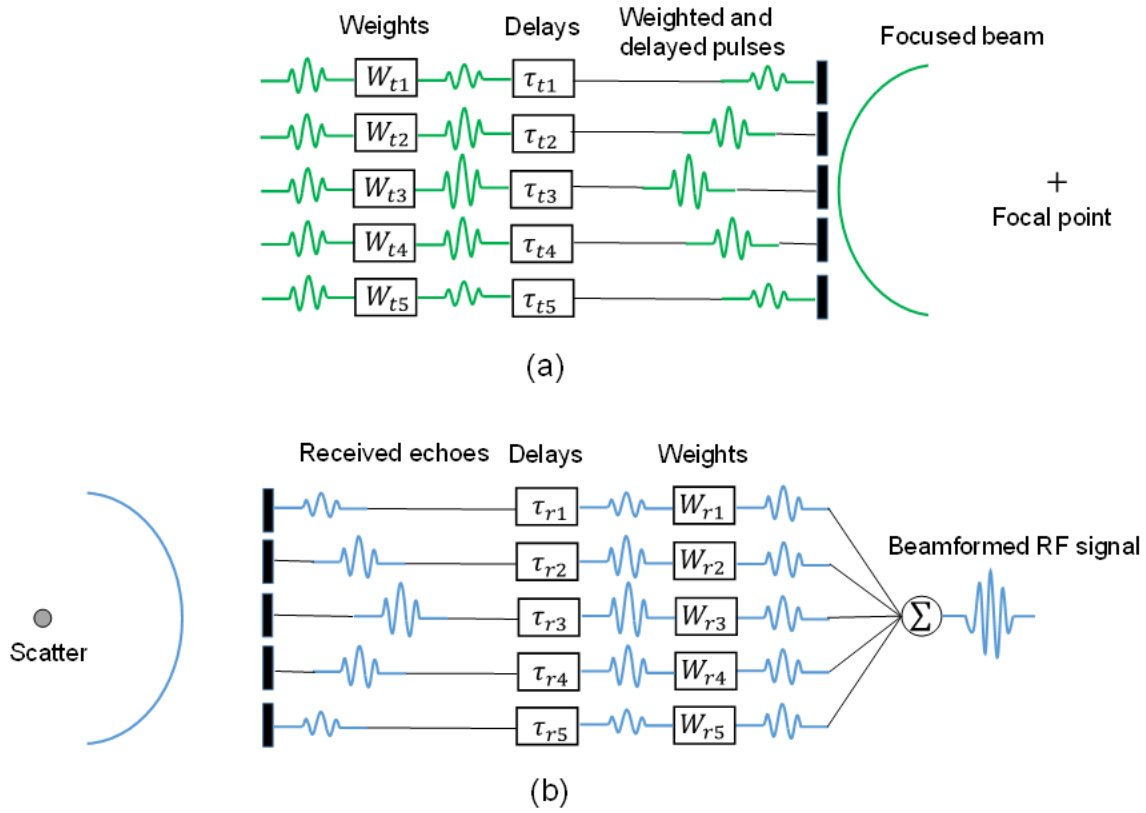

Figure 3.3 A diagram of delay and sum beamforming for transmitting (a) and receiving (b) phases using a linear transducer whose five elements are excited. The limited number of elements considered is just for the purpose of display.

3.1.3 Standard ultrasound beamforming

During transmitting and receiving of ultrasound signals, the generation and control of the ultrasound beam are called beamforming. A standard ultrasound beamforming technique is the delay and sum (DAS) approach (see figure 3.3). In transmitting, the amplitudes of pulses across transducer elements are controlled by applying a weight function, which is also referred as an apodization function. Then, weighted pulses are delayed to allow for compensation of travelling times between transducer elements and the focal point. Finally, weighted and delayed pulses are transmitted to form a focused beam. In receiving, transducer elements in turn collect received echoes, which are called raw channel data. To perform focusing in a certain region,

received echoes are accordingly delayed. Then, weighted echoes are summed to form a RF signal.

3.1.4 Beam manipulations

Ultrasound beam shapes can be altered by manipulating arriving time and amplitude of the pulse of individual elements in a transducer. For example, to steer a beam with an angle, a linear sequence of delays associated with the steering angle is applied into active transducer elements (see figure 3.4(a)). Using a linear transducer, beam steering allows to form images at different angles without moving the transducer. By compounding these images, image quality can be improved.

At a given depth, ultrasound beams can be focused on transmitting using a symmetric and spherical sequences of delays if the beam is perpendicular to the transducer surface (see figure 3.4(b)). In modern line-by-line focused imaging scanners, focal depths and numbers of focal points on transmitting are flexible and can be determined by users. More focal points provide better image quality but at the expense of a lower frame rate. A common way is multi-focal imaging where several beamformed RF signals with different focal depths are combined into one scan line. In addition, beam steering and focusing can also be performed simultaneously to make focused beams directional (see figure 3.4(c)), where delays depend on travelling times of ultrasound from transducer elements to the focal point. Other than transmitting focusing, dynamic receiving focusing can also be achieved at each depth using received echoes. It is more flexible than transmitting focusing as received echoes can be stored; delays can then be applied according to desired focussing depths without sacrificing the frame rate.

Ultrasound signals on some active transducer elements have to be attenuated to suppress side lobes of ultrasound beams in transmitting or receiving. This selective manipulation can be done by apodization (see figure 3.4(d) and (e)). Usually, some window functions, such as Gaussian or hamming function, are applied to excite the innermost elements using more powers.

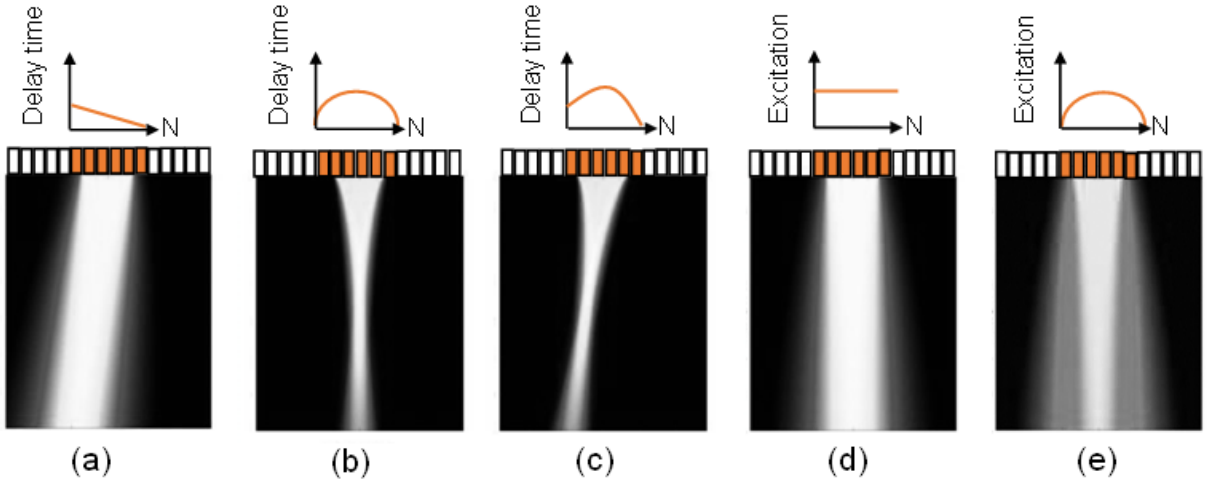

Figure 3.4 Beam shapes generated by a linear transducer with six active elements using unfocused beam steering (a), focusing without beam steering (b), focusing with beam steering (c), no apodization (d) and apodization (e).

3.1.5 Resolutions

Spatial resolution of an ultrasound imaging system corresponds to the smallest distance necessary between two targets to produce separate echoes. The axial resolution is equal to the half of the pulse wavelength. Higher transmitted frequency thus means a better axial resolution. Lateral resolution at a focal point is determined by the width of the ultrasound beam. For line-by-line focused imaging, the beam width is proportional to the transmitted frequency and F-number, which is defined as the ratio between the dimension of the active transducer aperture and focal depth. The elevational resolution is the slice thickness of a 2-D imaging plane. For a linear transducer, the elevational resolution is associated with the element height, focal depth and transmitted pulse wavelength.

It is necessary to consider temporal resolution when imaging moving targets. The temporal resolution is related to the time interval of transmitted pulses and the way to construct an image. The minimum time interval, which is the reciprocal of the pulse repetition frequency, ensures the echo from preceding pulse does not overlap with the echo of the following pulse. For an example of line-by-line focused imaging (see figure 3.2), the temporal resolution would be lower if we would construct an image with more scan lines as more pulse transmissions would be needed.

3.2 Advanced beamforming approaches

Conventional line-by-line focused imaging limits the accuracy of NIVE. One factor is that focused imaging provides relatively low temporal resolution of around 30-100 frames per second as it builds images sequentially [18]. The low frame rate can result in a large motion between two consecutive frames, thus requiring additional efforts to deal with these large displacements. Moreover, the lower frame rate can cause larger inter-frame out-of-plane motions, which increase image decorrelation thereby inducing inaccurate estimations with NIVE. The other factors are the limited lateral resolution of focused imaging, and the absence of phase information for speckle tracking in that direction. Thus, the lateral estimation of NIVE is not as reliable as for the axial estimation. To obtain more accurate motion estimation, some advanced beamforming approaches have been introduced into NIVE. In this section, we firstly introduce some ultrafast imaging techniques using unfocused transmission strategies to enhance the imaging frame rate. Then, some beamforming techniques trying to increase lateral resolution of images are also presented. Some of them also aim providing lateral phase information. Please note that only advanced beamforming approaches applied into the framework of ultrasound elastography are described in this section. Some other advanced beamforming approaches can be found in [72-76].

3.2.1 Synthetic aperture imaging

Synthetic aperture imaging, as depicted in figure 3.5, uses a succession of single-element transmissions to construct a low resolution image using echoes received by all elements. Then, these low resolution images are combined into a high resolution image.

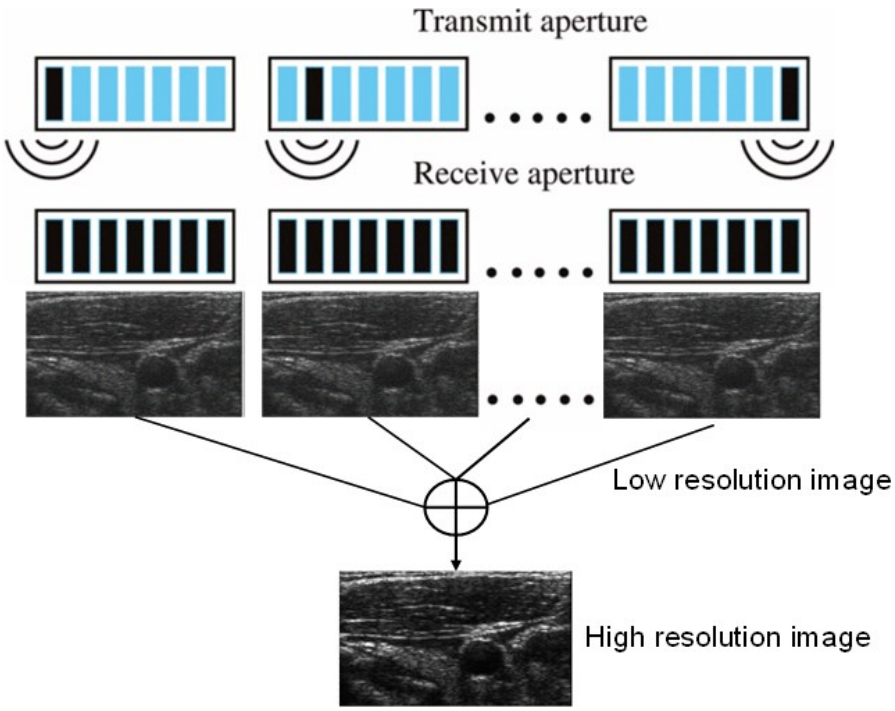

Figure 3.5 Principle of synthetic aperture imaging. In transmitting, each element sends a spherical wave sequentially spreading throughout the entire scan plane. In receiving, all elements of a transducer acquire echoes. For each transmitting and receiving event, channel data are reconstructed into a low resolution image using DAS approach. Finally, all low resolution images are summed into a high resolution image.

Using raw channel data from each transmission, receiving focusing can be implemented at each imaging point through DAS beamforming by considering round trip times from transmitting elements to the point target and back to receiving elements. To perform transmitting focusing, channel data from multiple unfocused single-element transmissions are summed coherently into a final beamformed signal. The final beamformed signal $s(x,z)$ at position of (x,z) can be written mathematically as

$$s(x,z) = \sum_{i=1}^{N_{TX}} \sum_{j=1}^{M_{RX}} W_{ij} RF_{ij}(\tau_{TX,RX}), \tag{3.3}$$

$$\tau_{TX,RX} = (\sqrt{z^2 + (x - x_i)^2} + \sqrt{z^2 + \left(x - x_j\right)^2})/c, \tag{3.4}$$

where N_{TX} and M_{RX} are the numbers of active elements used in transmitting and receiving modes, respectively; RF_{ij} is the RF signals received by the j^{th} element from the i^{th} element transmission; W_{ij} corresponds to the apodization function; and $\tau_{TX,RX}$ is the applied time delay

which accounts for the wave transmitted from the i^{th} element position, x_i, to the point target and back to the j^{th} element position, x_j. In a word, dynamic focusing in transmitting and receiving enables synthetic aperture imaging to have a good resolution.

Another advantage of synthetic aperture imaging is its high frame rate as one full image is formed in one transmission. In comparison, with line-by-line focused imaging, only one scan line is formed in one transmission. Another similar technique, sparse synthetic aperture imaging that uses limited active elements instead of all elements can achieve a higher frame rate (*e.g.*, 1000 frames per second) [77].

3.2.2 Plane wave imaging

Another alternative for ultrafast imaging is plane wave imaging, which generates a plane wavefront by activating all transducer elements instead of only firing one element at a time. Each transmission of unfocused plane waves allows to construct one image. Theoretically, the frame rate is equivalent to the pulse repetition frequency and can reach up to 20 kHz. To obtain better image quality than single plane wave imaging, Montaldo *et al*. [78] proposed coherent plane wave compounding (CPWC) imaging, where low resolution images using several plane waves with tilted angles are coherently summed to form a high resolution image. As shown in figure 3.6, several tilting plane waves are transmitted using all transducer elements activated by a vector of linear delays, τ_θ, which are defined as

$$\tau_\theta = N d_{pitch} sin\theta / c, \tag{3.5}$$

where N is the number of transducer elements, d_{pitch} is the pitch that is the distance between adjacent transducer elements, and θ is the steering angle. Then, acquired echoes using the same elements are beamformed using the DAS method and coherently summed considering transmitting angles as

$$s(x,z) = \sum_{i=1}^{N_{TX}} \sum_{j=1}^{M_{RX}} W_j RF_i(\tau_{TX,RX}), \tag{3.6}$$

$$\tau_{TX,RX} = (xcos\theta_i + zsin\theta_i + \sqrt{z^2 + \left(x - x_j\right)^2})/c, \tag{3.7}$$

where N_{TX} and M_{RX} are the numbers of active elements used in transmitting and receiving modes, respectively; RF_j is the RF echo received by the j^{th} element; W_j represents the receiving

apodization function; $\tau_{TX,RX}$ is the applied time delay, which accounts for the wave transmitted at the angle θ_i, to the point target and back to the j^{th} element position, x_j. CPCW imaging can achieve the same image quality as multi-focal images using line-by-line focused imaging while keeping the frame rate ten times higher [78].

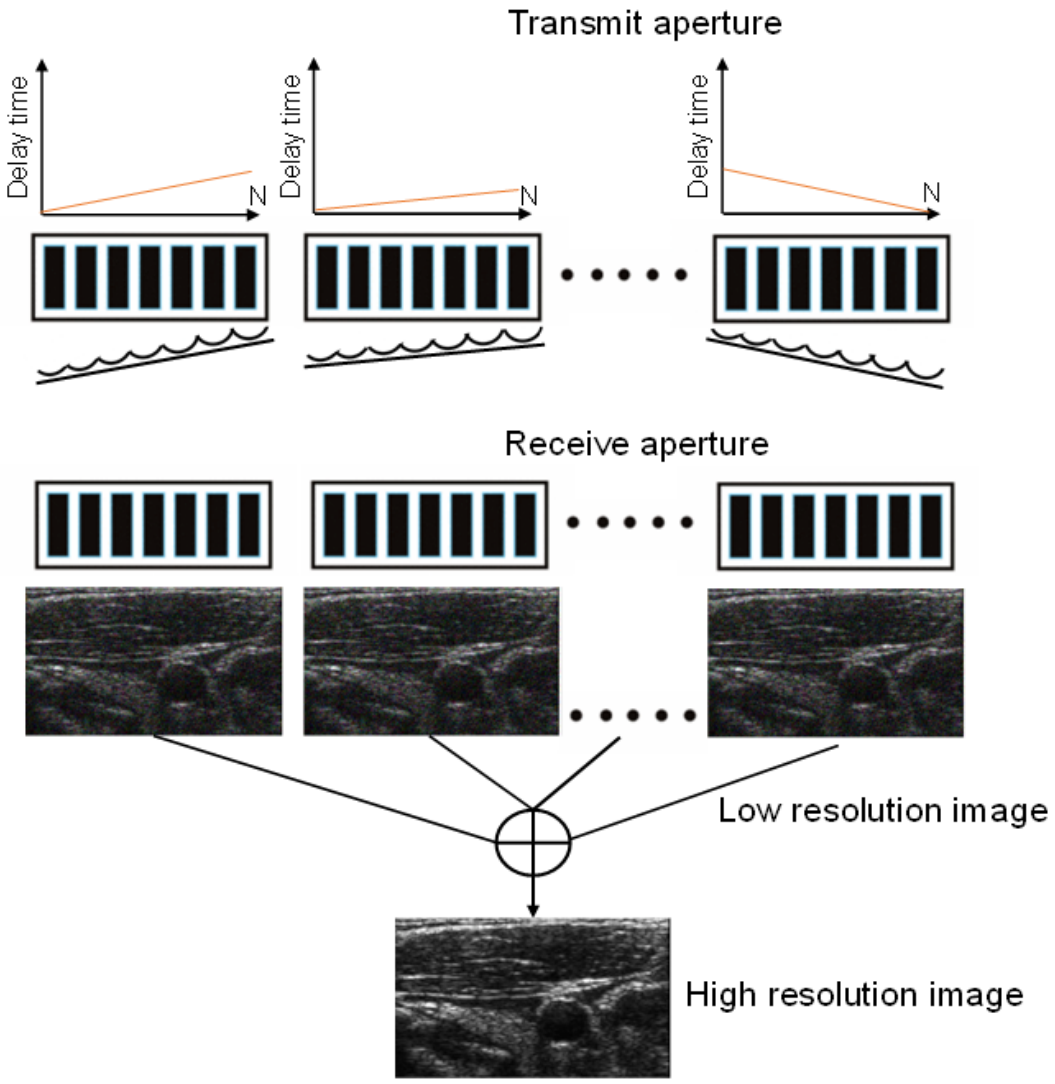

Figure 3.6 Principle of coherent plane wave imaging. In transmission, several tilting plane waves are generated using all transducer elements activated by linear delays. In receiving, all transducer elements acquire echoes. For each transmission and receiving event, channel data are beamformed into a low resolution image. Finally, all low resolution images at different tilting angles are coherently summed into a high resolution image.

3.2.3 Transverse oscillation beamforming

The anisotropy of speckle patterns of an ultrasound image due to the limited lateral resolution deteriorates lateral strain estimations. Transverse oscillation (TO) beamforming is a technique to produce a lateral beam profile that is as close as possible to the axial beam profile. As shown in figure 3.7, there are more oscillations in the lateral beam profile when using TO beamforming, which could allow a better performance of lateral motion tracking similar to the one in the axial direction. TO beamforming was originally proposed to modulate the lateral beam so as to estimate 2-D velocity vectors of blood flow [79, 80]. Afterwards, it was applied in elastography to generate TO images that were used to obtain for more accurate lateral displacement estimates [81]. Recently, TO beamforming was coupled with plane wave imaging to characterize *in vivo* flow velocity [82] and pulse wave velocity of an arterial wall [22].

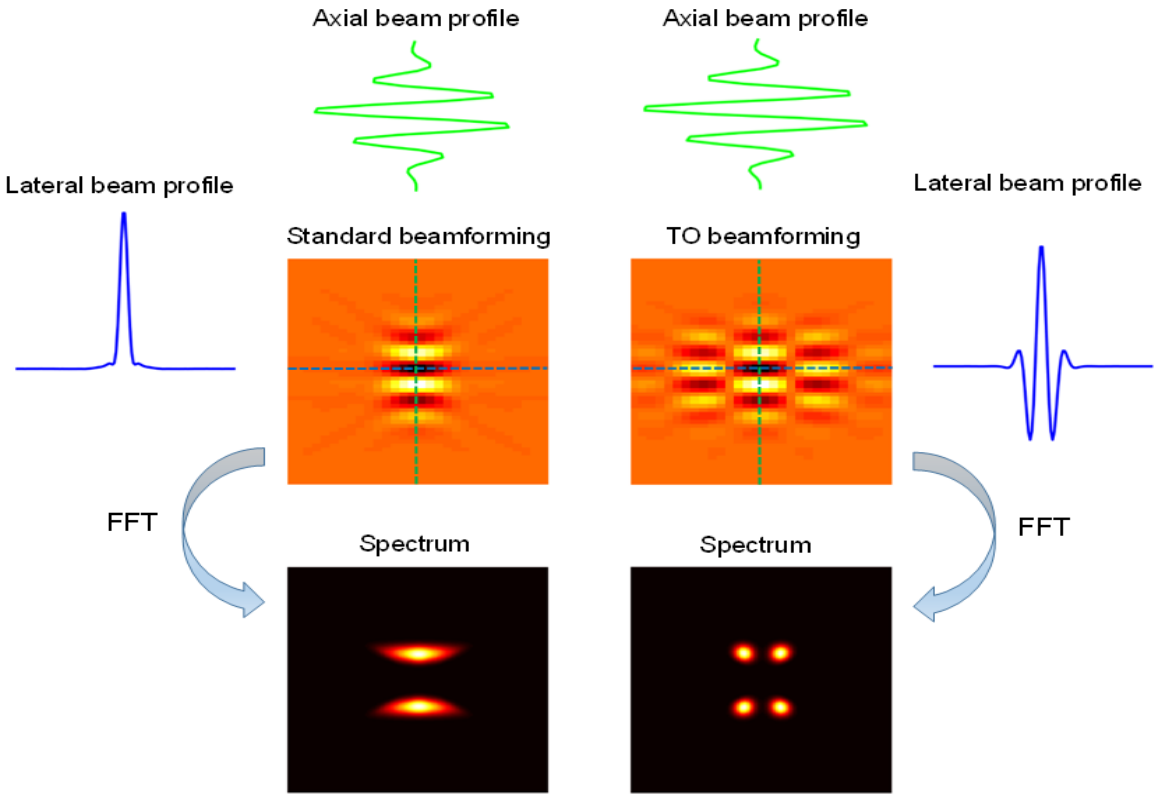

Figure 3.7 Beamformed images and corresponding frequency spectra using standard and TO beamforming, respectively. Lateral and axial beam profiles indicated by blue and green lines are shown, respectively.

There are two ways to generate TO images. The first one is to use the DAS method with specific apodization functions. It differs from conventional apodization functions used for the DAS method as it is a two Gaussian peaks apodization function. Moreover, the distance between the two peaks should be changed with increasing imaging depth. The final TO image is generated by weighting and summing beamformed RF signals using the predefined apodization functions. An alternative way to generate TO images is by the TO filtering method, which is performed on the spectrum of beamformed data. A filter mask is multiplied with the spectrum of the beamformed RF image, which features the spectrum of a TO image as four sub-regions (see figure 3.7). Then, a TO image is recovered by an inverse Fourier transform.

3.3 Summary

Line-by-line focused imaging provides a low frame rate. Moreover, there is a trade-off among the number of transmitting focused points, frame rate and image resolutions. Ultrafast imaging techniques have been developed to achieve dynamic transmitting and receiving focusing to maximize spatial resolution while keeping a high frame rate, which could improve the performance of NIVE.

Korukonda and Doyley showed that the high lateral resolution of synthetic aperture imaging improved lateral NIVE estimations [20, 21]. However, single-element transmission with synthetic aperture imaging induces less transmitted energy, which decreases the penetration depth and signal-to-noise ratio (SNR) of beamformed images. Plane wave imaging avoids this limitation through using all elements to transmit a plane wave. To produce high quality images at an ultrafast frame rate, CPWC imaging was proposed and subsequently introduced into NIVE. Poree *et al*. [18] verified that CPWC imaging helps obtaining more accurate NIVE strain estimations than using line-by-line focused imaging. Even so, lateral NIVE estimations are still challenging due to limited phase or speckle information existing in the lateral direction of images. TO beamforming allows to introduce lateral oscillations to help tracking lateral motions. Thus, an ultrafast TO imaging coupling CPWC imaging with TO beamforming could be beneficial for strain estimations with NIVE, which is detailed in Chapter 5. In the next chapter, the principle of ultrasound elastography and strain estimation algorithms for NIVE are described.

Chapter 4 : Ultrasound elastography

4.1 Background

It is known that changes in mechanical properties of tissues are associated with the onset and progression of some diseases. For example, tissues tend to be stiffer for liver cirrhosis. Palpation has been used for centuries by physicians who compress an organ and feel its stiffness for disease diagnosis. However, palpation is subjective. Elastography seeks to objectively characterize tissue stiffness using modalities of medical imaging, such as ultrasound or MRI. For example, in ultrasound elastography, tissue deformation is induced by internal or external excitation. Then, the response of tissue deformation is captured by ultrasound images from which elastography techniques can derive information on tissue stiffness, which is unattainable with conventional ultrasound echo imaging.

Current ultrasound elastography techniques can be classified into quasi-static or dynamic elastography. Quasi-static elastography, also called strain imaging, measures the tissue strain under a stress induced by excitations. The first work on strain imaging utilized a manual compression on the top of a tissue to induce its deformation [8]. Later, a focused ultrasound beam was used to deform the tissue through acoustic radiation force impulse (ARFI) imaging [83]. Another way to induce deformation is to exploit cardiovascular natural movements. Strain imaging based on cardiac pulsation is referred as myocardial elastography [84]. When pulsating vessels are studied, IVUS elastography [85] and NIVE [86] were respectively proposed to assess vascular elasticity invasively and noninvasively.

Dynamic elastography, also referred as shear wave imaging, applies mechanical excitations to produce a shear wave. The tracking of this shear wave allows quantifying the elastic modulus of a tissue. More details on shear wave imaging can be found in [87-89]. In this thesis, the focus is mainly on strain imaging and details are described in the next section.

4.2 Principles of ultrasound strain imaging

Ultrasound strain imaging is a technique to measure relative stiffness of tissues, which assumes that a soft tissue is supposed to deform more (representing larger strain) than a hard

tissue under the same stress. It was firstly introduced by Ophir *et al* [8] in 1991. The principle in 1-D of strain imaging is shown in figure 4.1. Here, an ultrasound transducer uniaxially applies a small compression on a soft phantom with a hard inclusion. The deformation process of the phantom can be regarded as the compression of a spring where the parts with different stiffness would give rise to different displacements according to the Hooke's law. To measure these displacements at each depth, a cross-correlation method is used to analyze two RF signals, namely pre-compression and post-compression signals. Finally, the spatial gradient of the displacement field represents the strain distribution, which is also known as an elastogram.

As tissues deform in all three dimensions, 2-D strain estimations are preferred instead of 1-D estimations when performing a 2-D scan. In the next section, state-of-the-art 2-D strain estimation methods are described.

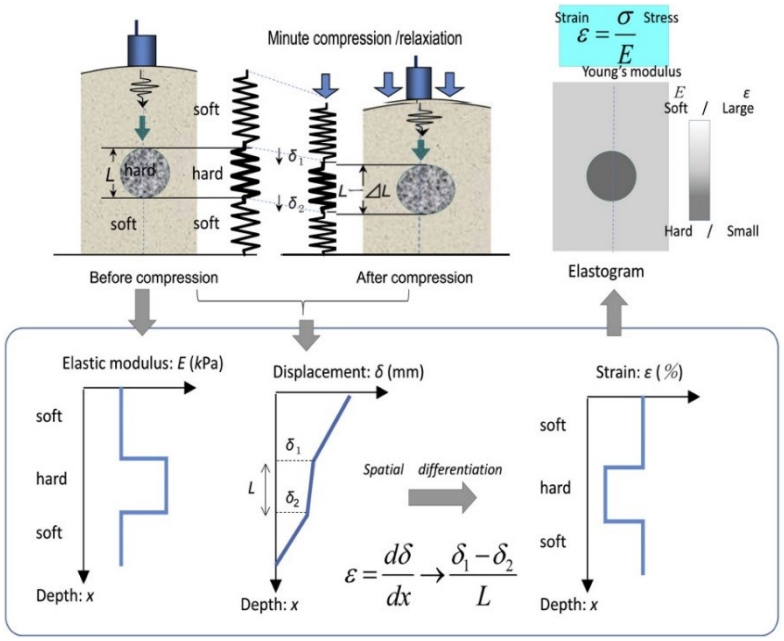

Figure 4.1 Principle of ultrasound strain imaging. A minute compression is applied on a soft phantom with a hard inclusion. Two RF signals, pre-compression and post-compression signals, are acquired and analyzed to obtain displacements at each depth. Finally, the spatial gradient of the displacement field represents the strain distribution. Adapted from [90].

4.3 Strain estimation methods

Most 2-D strain estimation methods can be categorized as either window-based or pixel-based methods. Window-based methods use a local strategy which assumes that pixel motions inside a measurement window are uniform and attempt to estimate the motion of a block centroid using some similarity metrics (see figure 4.2). Pixel-based methods utilize a global strategy which estimates the motion of each pixel by imposing some prior information. The two different methods are described in following sections.

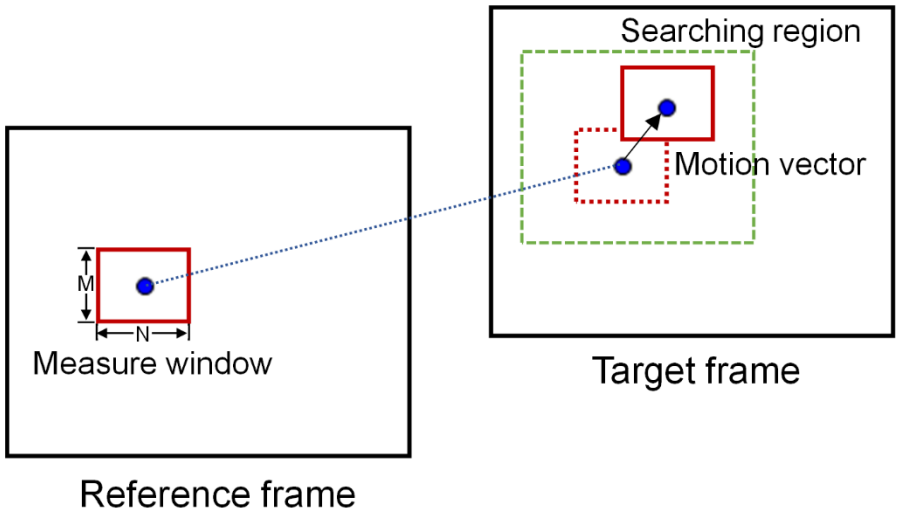

Figure 4.2 Diagram of window-based motion estimation. A measurement window with size of $M \times N$ defined in a reference frame is tracked within a searching region of a target frame. The motion vector of the image block is estimated using some similarity metrics.

4.3.1 Window-based strain estimation methods

4.3.1.1 Space-domain methods

Space-domain methods exploit the similarity of image intensities of two image blocks. Like the block matching strategy in computer vision, a reference block is tracked in a searching region using some similarity metric. In ultrasound elastography, they are also referred to as speckle tracking methods.

The most commonly used similarity metric is the normalized cross-correlation (NCC),

$$NCC(i,j) = \frac{\sum_{y=0}^{M-1}\sum_{x=0}^{N-1}(r(x,y)-\bar{r})(t(x+i,y+j)-\overline{t(i,j)})}{\sqrt{\sum_{y=0}^{M-1}(r(x,y)-\bar{r})^2 \sum_{x=0}^{N-1}(t(x+i,y+j)-\overline{t(i,j)})^2}}, \quad (4.1)$$

where r and t are pixel intensities from reference and target frames, respectively, and $\bar{r}$ and $\bar{t}$ are mean pixel intensities inside measurement windows with size of $M \times N$ from reference and target frames, respectively. The position of the peak of a 2-D NCC map determines the displacement vector of the centroid of a measurement window. Nevertheless, this is only able to provide displacement estimations at an integer pixel level. To obtain sub-pixel accuracy, ones either interpolate RF signals before computing NCC [91] or fit the NCC map into a sub-pixel resolution using some analytical functions [92-95]. After that, the peak position of a NCC map gives rise to sub-pixel estimations at the expense of higher computational load. Other than the NCC metric, the sum absolute difference (SAD) [96] and the sum squared error (SSE) [16, 97] are also used as similarity metrics. A lower SAD or SSE value implies higher correlation of two image blocks.

In practice, a correlation would be deteriorated due to the change of speckle patterns when complex anatomical structures or out-of-plane motions are existing, which is also called speckle decorrelation. To reduce speckle decorrelation, prior information, such as displacement continuity, is combined with NCC or SAD measurement as a cost function to obtain a smooth displacement vector [98-100]. McCormick *et al*. [101] proposed to incorporate motion information of neighboring blocks into a NCC similarity metric. A Bayesian framework was used to convert displacement estimation into probability density estimation by maximizing posterior probability density.

Another category of window-based space-domain methods originates from the optical flow algorithm in computer vision. Assuming that the intensity of a point at location (x, z) moving by (U_x, U_z) between two consecutive ultrasound images remains constant, $I(x,z,t) = I(x+U_x, z+U_z, t+1)$, which can be expanded by Taylor series and by ignoring high-order terms, one gets $I(x+U_x, z+U_z, t+1) = I(x,z,t) + I_x U_x + I_z U_z + I_t$. Then, the optical flow constraint equation is expressed in linear algebra form as:

$$[I_x \quad I_z]\begin{bmatrix}U_x\\U_z\end{bmatrix} = -I_t, \quad (4.2)$$

where I_x, I_z, I_t are the derivatives of the image intensity in the corresponding direction. Since there are two unknown variables in (4.2), Lucas and Kanade [102] proposed the Lucas-Kanade (LK) optical flow method, which assumes displacements of pixels within a small measurement window with size of $M \times N$ being the same. Then, an over-determined linear equation system can be built as:

$$\begin{bmatrix} I_{x_1} & I_{z_1} \\ \vdots & \vdots \\ I_{x_{M\times N}} & I_{z_{M\times N}} \end{bmatrix} \begin{bmatrix} U_x \\ U_z \end{bmatrix} = - \begin{bmatrix} I_{t_1} \\ \vdots \\ I_{t_{M\times N}} \end{bmatrix}. \tag{4.3}$$

The solution can be solved locally using a least squares scheme. Since the optical flow method can achieve sub-pixel precision, the LK optical flow method was used for fine estimations in a hybrid framework in which other window-based methods were deployed first for coarse estimations [15, 103].

Once displacements are obtained, strains are computed with displacement derivatives. However, the two-point derivative operation amplifies the noise of displacement estimations, especially for lateral estimations [104]. A least squares strain estimator (LSQSE) [105] is usually used to compute spatial derivatives with less variances through a linear fit of multiple points instead of two points although it reduces the elastogram resolution [106].

An affine model-based method is an alternative way to estimate strains directly, *i.e.* without computing displacement derivatives. In the framework of the LK optical flow estimation, Maurice *et al*. [107] proposed an optical flow-based Lagrangian speckle model estimator (LSME) to obtain affine motion components (see figure 4.3). Within a pre-compression measurement window whose center point is *C*, the first-order Taylor expansion of displacements of a point *P* is presented as

$$U_x(x_p, z_p) = U_x(x_c, z_c) + (x_p - x_c)s_{xx}(x_p, z_p) + (z_p - z_c)s_{xz}(x_p, z_p), \tag{4.4}$$

$$U_z(x_p, z_p) = U_z(x_c, z_c) + (x_p - x_c)s_{zx}(x_p, z_p) + (z_p - z_c)s_{zz}(x_p, z_p), \tag{4.5}$$

where x_p, z_p and x_c, z_c are the coordinates of point *P* and *C* in the lateral and axial directions respectively, and s_{xx}, s_{xz}, s_{zx}, s_{zz} stand for lateral strain, lateral shear, axial shear and axial strain, respectively. To simplify the notations, an arbitrary point is considered and x_c, z_c are set

to zero to assume estimations locally. Replacing U_x and U_z in (4.2) with (4.4) and (4.5), (4.2) is thus rewritten as:

$$[I_x x \quad I_x z \quad I_x \quad I_z x \quad I_z z \quad I_z] \begin{bmatrix} s_{xx} \\ s_{xz} \\ U_x \\ s_{zx} \\ s_{zz} \\ U_z \end{bmatrix} = -I_t. \tag{4.6}$$

Compared with (4.2), the number of unknown variables is increased to six in (4.6). To solve the six motion components, an over-determined linear equation system considering a measurement window can be built and solved in a similar manner as (4.3).

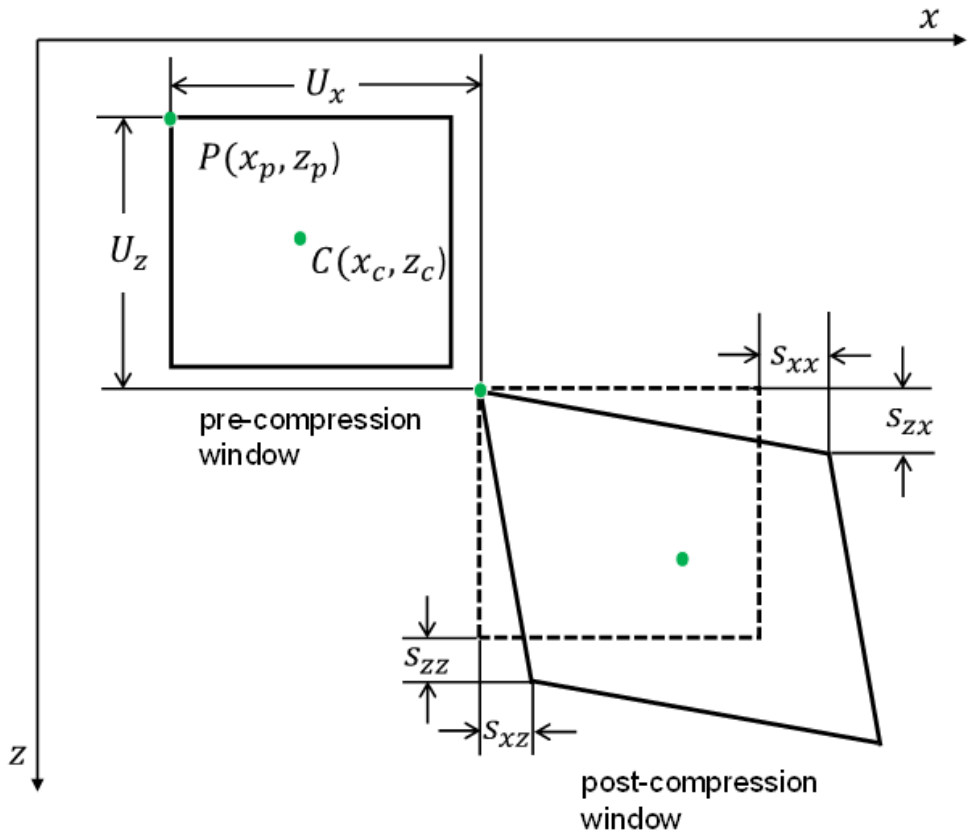

Figure 4.3 Illustration of the affine transformation of a point *P* in a measurement window with a center point *C*. x_p, z_p and x_c, z_c are the coordinates of point *P* and *C* in lateral and axial directions, respectively. U_x and U_z are lateral and axial displacements, respectively. s_{xx}, s_{xz}, s_{zx}, s_{zz} stand for lateral strain, lateral shear, axial shear and axial strain, respectively.

4.3.1.2 Frequency-domain methods

Sumi proposed a 2-D phase tracking method to obtain displacement vectors iteratively [108]. The principle is that the displacement vector of a reference image block is associated with the gradient of the phase of the cross-spectrum $S(k_x, k_z)$, which is computed by multiplying the 2-D discrete Fourier transform of the reference block by the conjugate Fourier transform of a spatial shifted block. Here, k_x and k_z are frequency variables in the lateral and axial directions, respectively. Assuming a measurement window where pixel displacements are uniform, the displacement components, d_x and d_z, are determined by minimizing the following cost function using a least squares scheme:

$$J = \sum_{k_x=0}^{M} \sum_{k_z=0}^{N} \|S(k_x, k_z)\|^2 \left\{\Theta(k_x, k_z) - \frac{2\pi}{M}\frac{d_x}{\Delta x}k_x - \frac{2\pi}{N}\frac{d_z}{\Delta z}k_z\right\}^2, \tag{4.7}$$

where Θ is the phase of the cross-spectrum, and Δx and Δz are lateral and axial image resolution, respectively. At each iteration, the searching region is warped using the displacement vector from previous iteration, after which a new displacement vector can be obtained using (4.7) again. Until a certain criterion is reached, the iteration is terminated. The final displacement vector is an accumulation of each iterative estimation.

Nevertheless, it is not easy to perform 2-D estimations in the frequency domain as lateral phase information is not available since there is no carrier frequency in the lateral direction with conventional ultrasound echoes. Basarab *et al*. [109] proposed a phase-based block matching method to obtain more accurate lateral estimations using 2-D RF images modulated by TO beamforming (see section 3.2.3). They found a relation between the displacement vector and the phases of analytical images as follows:

$$\begin{bmatrix} 2\pi f_x & 2\pi f_z \\ -2\pi f_x & 2\pi f_z \end{bmatrix} \begin{bmatrix} U_x \\ U_z \end{bmatrix} = \begin{bmatrix} \Phi_1 \\ \Phi_2 \end{bmatrix}, \tag{4.8}$$

where f_x and f_z are modulated spatial frequencies in lateral and axial directions, respectively, that are assumed to be known, and Φ_1 and Φ_2 are phase differences of Fourier spectra from original TO RF images. Introducing the affine transformation (4.5) and (4.6) into (4.8), the phase-based method was developed into an affine phase-based estimation method [110], which has been proposed to evaluate cardiac motions [17].

4.3.2 Pixel-based strain estimation methods

Instead of performing estimations within a measurement window using window-based methods, pixel-based methods can globally derive displacements of each pixel inside a ROI to obtain a dense motion field. There are a few pixel-based methods used in ultrasound elastography. These methods normally formulate displacement estimations as an optimization problem where a cost function incorporating a data term and a regularization term is minimized as follows,

$$\min_{U_x,U_z} D_{data}(U_x, U_z) + \lambda R_{reg}(U_x, U_z), \tag{4.9}$$

where λ is a parameter to control the influence of the regularization term. The most common regularization term is the spatial smoothness constraint. This physical prior information reduces, to some extent, estimation variances due to speckle decorrelation. Recently, temporal continuity was jointly considered to make estimations more robust [111]. The data term exploits the correspondence between pre-compression and post-compression images. In 1981, Horn and Schunck [26] proposed the classical HS optical flow method, which includes the optical flow constraint equation (see (4.2)) as a data term and a global displacement smoothness constraint as a regularization term. This method has been used to characterize strains of carotid plaques [112] and breast phantoms [113, 114]. With a local smoothness constraint, negative NCCs were used as a data term of a cost function to compute a 2-D displacement field [106, 115]. SSE was also used as a data term coupled with a displacement continuity regularization for 2-D displacement estimations [116, 117].

A disadvantage of these optimization-based methods is their computational complexity as they require to optimize iteratively a cost function until convergence. A dynamic programming and analytic minimization of the cost function was proposed to avoid an iteration process [116, 118]. It reduced computation time and enabled real time ultrasound elastography.

Once 2-D displacements are obtained, axial and lateral strains can be computed using the LSQSE method as done for window-based methods or Kalman filtering [116]. Although some works have considered axial or lateral strain during the minimization process [106, 115], shear strains are still missing.

4.4 Summary

Tissue motion is complex and does not necessarily undergo rigid transformations (displacement) alone, but also compression and expansion (strains and shears). Most of above-mentioned strain estimation methods, either window-based or pixel-based, are displacement-based. Strains and shears are computed from derivatives of displacements. Because the derivative operation is highly sensitive to high-frequency noise and to decorrelation, some direct strain estimation methods attempted to obtain strains directly using adaptive stretching [104, 119-121] or spectrum shift [122, 123] strategies without an explicit derivative operation. However, these methods are only able to provide 1-D axial strain estimation. For cross-sectional NIVE, the lateral strain and shears are necessary to build radial and circumferential strain maps. Above-mentioned affine estimation methods could be a suitable alternative to provide strain estimations with full strain components. However, these window-based methods always have a trade-off between window size, overlap and estimation accuracy. Usually, considering a small window results in image decorrelation inducing larger estimation variances, but with a higher elastogram resolution. A large window is able to increase correlation, while decreasing spatial resolution of strain maps. Pixel-based methods avoid this issue at the cost of a high computation time, but they are displacement-based with the need of a derivative operation.

To conclude this section, a direct and pixel-based strain estimation method is needed for cross-sectional or longitudinal 2-D NIVE. Implementing such approach in the context of 3-D imaging would also be highly relevant but it is beyond the scope of this thesis. In Chapter 7, a novel strain estimation algorithm is proposed. It is able to estimate pixel-wise strains globally against local noise. Moreover, an analytical solution is formulated avoiding the need of an iterative minimization to achieve a high computation efficiency.

Chapter 5 : Two-dimensional affine model-based estimators for principal strain vascular ultrasound elastography with compound plane wave and transverse oscillation beamforming

5.1 Introduction to manuscript

This chapter reproduces the content of a published article 'Two-dimensional affine model-based estimators for principal strain vascular ultrasound elastography with compound plane wave and transverse oscillation beamforming' in the journal *Ultrasonics* (Vol. 91, p. 77-91, 2019) by Hongliang Li, Jonathan Porée, Marie-Hélène Roy Cardinal and Guy Cloutier after evaluation by a peer review committee.

The following is the order of authors for this published article and corresponding affiliations:

Hongliang Li[1,2], Jonathan Porée[1,2], Marie-Hélène Roy Cardinal[1] and Guy Cloutier[1,2,3]

[1] Laboratory of Biorheology and Medical Ultrasonics, University of Montreal Hospital Research Center (CRCHUM), Montréal, QC, Canada;

[2] Institute of Biomedical Engineering, University of Montreal, Montréal, QC, Canada;

[3] Department of Radiology, Radio-Oncology and Nuclear Medicine, University of Montreal, Montréal, QC, Canada.

The contributions of all authors of the published article is detailed below:

Hongliang Li: Developed and implemented the corresponding beamforming and strain estimation algorithms, performed the post-processing of the data, drafted the manuscript and responded to the reviewer's comments of the article.

Jonathan Porée: Developed the finite element model, performed *in vitro* data acquisitions, contributed to strain estimation algorithms.

Marie-Hélène Roy Cardinal: Contributed to the interpretation of results and the revision of the manuscript.

Guy Cloutier: Supervised this work as the research director. Contributed to the interpretation of results as the project director. Corrected and finalized the manuscript for submission and revision.

5.2 Abstract

Polar strain (radial and circumferential) estimations can suffer from artifacts because the center of a nonsymmetrical carotid atherosclerotic artery, defining the coordinate system in cross-sectional view, can be misregistered. Principal strains are able to remove coordinate dependency to visualize vascular strain components (*i.e.*, axial and lateral strains and shears). This paper presents two affine model-based estimators, the affine phase-based estimator (APBE) developed in the framework of transverse oscillation (TO) beamforming, and the Lagrangian speckle model estimator (LSME). These estimators solve simultaneously the translation (axial and lateral displacements) and deformation (axial and lateral strains and shears) components that were then used to compute principal strains. To improve performance, the implemented APBE was also tested by introducing a time-ensemble estimation approach. Both APBE and LSME were tested with and without the plane strain incompressibility assumption. These algorithms were evaluated on coherent plane wave compounded (CPWC) images considering TO. LSME without TO but implemented with the time-ensemble and incompressibility constraint (Porée *et al*., IEEE Trans. Med. Imag. 2015) served as benchmark comparisons. The APBE provided better principal strain estimations with the time-ensemble and incompressibility constraint, for both simulations and *in vitro* experiments. With a few exceptions, TO did not improve principal strain estimates for the LSME. With simulations, the smallest errors compared with ground true measures were obtained with the LSME considering time-ensemble and the incompressibility constraint. This latter estimator also provided the highest elastogram signal-to-noise ratios (SNRs) for *in vitro* experiments on a homogeneous vascular phantom without any inclusion, for applied strains varying from 0.07% to 4.5%. It also allowed the highest contrast-to-noise ratios (CNRs) for a heterogeneous vascular phantom with a soft inclusion, at applied strains from 0.07% to 3.6%. In summary, the LSME outperformed

the implemented APBE, and the incompressibility constraint improved performances of both estimators.

Keywords – Ultrasound elastography, compound plane wave imaging beamforming, transverse oscillation beamforming, optical flow estimation, phase estimation, affine model-based estimation, tissue incompressibility.

5.3 Introduction

In recent years, noninvasive vascular elastography (NIVE) has gained increasing attention for evaluating the functionality of superficial arteries. Principal strains are able to remove coordinate dependency to visualize vascular strain components [124]. Currently, most two-dimensional (2-D) elastography algorithms are based on the cross-correlation, either in the space domain [14, 21, 92, 125-130] or frequency domain [131-133], or based on registration methods [99, 115]. With known axial (along the ultrasound beam) and lateral (perpendicular to it) displacements between pre- and post-motion image blocks, axial and lateral strains and shears were computed from estimated displacement derivatives in respective directions [21, 128, 131, 132]. Since associated high frequency displacement noise enhances the variance of such strain estimators, the least squares strain estimator (LSQSE) was proposed to increase the signal-to-noise ratio (SNR) by a piecewise linear fit [14, 92, 125, 130]. However, tissue motion in the imaging plane may be complex and does not necessarily only undergo rigid transformations (translations and rotations), but also compression and expansion [134]. The signal distortion caused by such complex deformations induces decorrelation effects. Signal processing strategies, such as temporal stretching [135] and iterative coarse-to-fine approaches [92, 136, 137], have been used to reduce decorrelation noise. Other estimators were also proposed to reduce decorrelation noise by considering axial strain or axial shear [115, 119, 138].

In addition to abovementioned rigid model-based estimators, an alternative strategy is the affine model-based estimation methodology, which considers all non-rigid deformations of the tissue. Space-domain and phase-domain affine model-based methods have been investigated for cross-sectional imaging of arteries [10, 16, 19, 139] and cardiac structures [17]. One of them is a registration-based algorithm [16]. It minimized a cost function using a numerical optimization method and improvements in SNR and contrast-to-noise ratio (CNR) were reported

on axial strain estimations compared to the 2-D cross-correlation, but at a higher computational time cost.

Two other space-domain methods based on optical flow (OF) were proposed. In [139], a two-step OF strategy was reported to improve the performance of the axial strain estimation. More specifically, the OF estimation was performed sequentially two times and the two axial strain estimates were recombined. However, shear components were unable to be recombined and the lateral strain was also not considered. Furthermore, this latter approach [139] requires extra computational load due to an additional OF estimation. The other affine method is the OF-based Lagrangian speckle model estimator (LSME). In [19], Mercure *et al*. concluded that this approach performed better than an optimization-based LSME due to its reliability and computational efficiency. In [18], an OF-based LSME involving a constrained motion model was developed to provide robust 2-D principal strain estimations. Another method with an affine model is the affine phase-based estimator (APBE) [17], inspired by the phase-based estimator (PBE) [109, 140, 141]. This algorithm demonstrated a more accurate lateral estimation for cardiac motions than the standard block matching algorithm.

To perform cross-sectional scans in the context of NIVE, lateral estimations are particularly challenging due to the lower lateral than axial resolution of conventional focusing imaging, and the lack of phase information in the lateral direction. To overcome this limitation, several methods have been introduced. One assumes tissue incompressibility to improve the quality of lateral displacements [142], and SNR and CNR of elastograms [131], [18]. Konofagou and Ophir used the lateral weighted interpolation of radiofrequency (RF) data to improve lateral displacement estimations [11]. However, the lateral interpolation and iterative scheme increase computational complexity [143].

Angular compounding schemes were also proposed to obtain lateral strain with more accurate axial estimations at multiple beam steering angles, using conventional focusing imaging [14, 144-146]. Another way is to use advanced beamforming methods to enable more accurate lateral estimations. Korukonda and Doyley [20, 21] demonstrated that synthetic aperture imaging could improve lateral NIVE estimates because of the high lateral sampling frequency and narrow lateral beamwidth. However, due to the single element emission, the low transmit power might be insufficient for the clinical use of NIVE [147]. Hansen *et al*. reported

that elastograms obtained with plane-wave angular compounding were comparable to standard focusing angular compounding [148]. Plane wave images are known, however, to exhibit low contrast and low resolution due to the lack of transmit focusing [75].

Alternatively, coherent plane wave compounding (CPWC) beamforming was proposed to solve these issues [78]. Under the framework of CPWC imaging, superior lateral strains and shears were obtained, compared with conventional OF-based LSME using standard focusing, by considering the incompressibility constraint and a time-ensemble approach [18]. Transverse oscillation (TO) beamforming [79, 80] was also proposed to improve lateral estimations for vector velocity [149], cardiac motion [17] and longitudinal vascular wall motion [22] assessments. In [150], TO was adapted to plane wave imaging using a Fourier domain beamforming. In the context of cross-sectional NIVE, however, the OF-based LSME and APBE using the combined CPWC and TO imaging beamforming (CPWC&TO) have not yet been studied.

In this manuscript, we provide a performance evaluation of different elastography estimators and image beamforming schemes for cross-sectional carotid artery scanning. Validations were performed with simulations and in vitro phantom experiments. Overall, three contributions were made in this paper. One contribution is on the performance evaluation of two affine model-based estimators in the same framework of high-frame-rate imaging. Those estimators are determining simultaneously, using a minimization process, the translation (axial and lateral displacements) and deformation (axial and lateral strains and shears) components that were then used to compute principal strains. The second contribution is on the development of the affine-based APBE, and the introduction of a time-ensemble approach and an incompressibility constraint, as proposed in [18] for the OF-based LSME. Those improvements provided better principal strain estimations than previous APBE. The third contribution is the introduction of transverse oscillations (TO) into the LSME and the verification that TO imaging may be helpful for principal strain estimations when the tissue structure is complex and heterogeneous. In this study, the OF-based LSME of [18] is used as a benchmark comparison method. A list of abbreviations used in this paper is given in Table 5-1.

Table 5-1 List of abbreviations

CPWC	Coherent Plane Wave Compounding beamforming
TO	Transverse Oscillation beamforming
CPWC&TO	Coherent Plane Wave Compounding with Transverse Oscillation beamforming
APBE	Affine Phase-Based Estimator
LSME	Lagrangian Speckle Model Estimator
CPWC&TO + APBE	APBE tested on CPWC&TO data
CPWC&TO* + APBE	APBE tested on CPWC&TO data with heterodyne demodulation
CPWC&TO + $APBE^{T}$	APBE with the time-ensemble approach tested on CPWC&TO data
CPWC&TO + $APBE^{T\&I}$	APBE with the time-ensemble approach and the incompressibility constraint tested on CPWC&TO data
CPWC&TO + $LSME^{T}$	LSME with the time-ensemble approach tested on CPWC&TO data
CPWC&TO + $LSME^{T\&I}$	LSME with the time-ensemble approach and the incompressibility constraint tested on CPWC&TO data
CPWC + $LSME^{T\&I}$	LSME with the time-ensemble approach and the incompressibility constraint tested on CPWC data (benchmark reference of [18])

5.4 Theory

5.4.1 Image formation

5.4.1.1 Coherent plane wave compounding beamforming

Ultrafast plane wave imaging only needs a simultaneous single pulse emission on all selected transducer elements to produce a plane wave illumination unlike the conventional line-by-line scanning mode. The image generated by this scheme, however, has low image resolution and contrast due to the lack of transmit focusing [75]. Montaldo *et al*. [78] proposed a coherent plane wave compounding beamforming to enhance the image quality without sacrificing significantly the high frame rate capability. Each point of an image formed by one single plane wave is obtained by summing RF signals along transducer elements using certain delays, as given by [78]:

$$s(x,\ z) = \int RF(x_i, \tau_{TX} + \tau_{RX}) dx_i, \tag{5.1}$$

where the coordinate x, z corresponds to the image plane, x_i is the position of the receiving transducer element, $\tau_{TX} = (zcos\theta + xsin\theta)/c$, $\tau_{RX} = \sqrt{z^2 + (x - x_i)^2}/c$, where τ_{TX} and τ_{RX} are the emission and receive delays, respectively, θ is the angle of the emission pulse, and c is the speed of sound. Once the image for one single plane wave is beamformed, the compounded image is obtained by summing coherently all beamformed images with several plane waves at different angles. Twenty-one emissions between −10° to 10° with a 1° increment provided the best image quality for vascular strain imaging using the ultrasound probe of the current study [18]. Therefore, we kept this configuration for simulations and *in vitro* experiments.

5.4.1.2 Filtering-based TO beamforming using CPWC images

Transverse oscillation beamforming allows producing lateral phase information in ultrasound images. Classical TO imaging requires a specific apodization function in reception, made of two Gaussian peaks, to modulate the frequency spectrum of the beamformed TO image into four identified spots [22, 151]. The following equation describes this apodization function w_i:

$$w_i = \frac{1}{2}\left(e^{-\pi\left(\frac{x_i - x_0}{\sigma_0}\right)^2} + e^{-\pi\left(\frac{x_i + x_0}{\sigma_0}\right)^2}\right), \tag{5.2}$$

where x_i is the position of the transducer element, $x_0 = \lambda_z z/\lambda_x$, $\sigma_0 = \sqrt{2}\lambda_z z/\sigma_x$, λ_z is the transmitted pulse wavelength, z is the depth of interest, λ_x is the expected lateral oscillation wavelength, and σ_x is the full width at half maximum (FWHM) of the Gaussian envelope. It can be noticed in (5.2) that the apodization function must be changed dynamically as a function of depth z to keep a constant lateral oscillation wavelength during image beamforming. In addition, to implement different TO parameters (*i.e.*, λ_x and σ_x) one needs to beamform the raw data again.

To overcome these limitations and allow determining proper parameters, a filtering (or convolution) method was used to generate TO images [22]. In theory, TO filtering is able to generate oscillations with any lateral wavelengths. One advantage of the TO filtering method is that it is easy to control and obtain optimal TO parameters. Such post-processing approach only needs to filter beamformed data using different TO parameters and does not require access to pre-beamformed data using different apodization functions. The filtering or convolution is only performed along the lateral direction if RF images are used, while both lateral and axial

directions should be filtered when B-mode images are considered. In this paper, we choose to filter each line of a RF CPWC image by multiplying it with two modulated Gaussian functions in the Fourier domain, as given by (5.3). The filtered frequency pattern of a RF image was made of four spots with an expected lateral oscillation frequency. This filter Ω is available in the public domain [152] as a Matlab graphical user interface. It is given by:

$$\Omega = e^{-2\left(\pi\sigma_x\left(x_f - \frac{1}{\lambda_x}\right)\right)^2} + e^{-2\left(\pi\sigma_x\left(x_f + \frac{1}{\lambda_x}\right)\right)^2}, \tag{5.3}$$

where σ_x and λ_x are defined in (2), and x_f is the lateral coordinate in the frequency domain of the RF image.

5.4.2 Elastography estimator description

5.4.2.1 Optical flow based Lagrangian speckle model estimator

The OF-based LSME accounts for rigid and non-rigid tissue motions using an affine transformation model, and estimates the displacement and strain in a small region of interest (ROI), also called measurement window (MW). Assuming that the image intensity between two consecutive RF images is not modified in a MW, we can deduce the optical flow equation for an arbitrary point:

$$I_x U_x + I_z U_z + I_t = 0, \tag{5.4}$$

where I_x, I_z are the spatial gradient of the image intensity, U_x, U_z represent the lateral and axial displacements, and I_t denotes the temporal gradient of the image intensity.

In a MW, taking a 1st order Taylor expansion of displacements U_x, U_z of an arbitrary point, the affine description of the displacement field is given by

$$U_x(x,z) = U_x(x_0,z_0) + (x - x_0)s_{xx} + (z - z_0)s_{xz}, \tag{5.5}$$

$$U_z(x,z) = U_z(x_0,z_0) + (x - x_0)s_{zx} + (z - z_0)s_{zz}, \tag{5.6}$$

where x_0, z_0 are coordinates of the center of the MW, s_{xx}, s_{xz}, s_{zx}, s_{zz} are the lateral strain, lateral shear, axial shear, and axial strain, respectively, and $s_{ij} = \partial U_i / \partial j$.

Since there are two unknown variables in (5.4), to solve the 2-D optical flow, we assume that the motion field of each pixel within a MW with $p \times q$ pixels is the same and that the coordinates of the center of the MW, x_0, z_0, are zero. Then, we can rewrite (5.4) by considering (5.5) and (5.6) for each pixel to obtain an over-determined linear equation system for all pixels in a MW,

$$\begin{bmatrix} I_{x_1}x_1 & I_{x_1}z_1 & I_{x_1} & I_{z_1}x_1 & I_{z_1}z_1 & I_{z_1} \\ \vdots & \vdots & \vdots & \vdots & \vdots & \vdots \\ I_{x_{p\times q}}x_{p\times q} & I_{x_{p\times q}}z_{p\times q} & I_{x_{p\times q}} & I_{z_{p\times q}}x_{p\times q} & I_{z_{p\times q}}z_{p\times q} & I_{z_{p\times q}} \end{bmatrix} \begin{bmatrix} s_{xx} \\ s_{xz} \\ U_x \\ s_{zx} \\ s_{zz} \\ U_z \end{bmatrix} = - \begin{bmatrix} I_{t_1} \\ \vdots \\ I_{t_{p\times q}} \end{bmatrix}. \quad (5.7)$$

Then, solving this equation system using a robust weighted least square method, as described by (4) of [18], the affine motion vector $\vec{m} = (s_{xx}, s_{xz}, U_x, s_{zx}, s_{zz}, U_z)^T$ is obtained. Note that derivatives of displacement are not used to compute strain components.

5.4.2.2 Affine phase based estimator

Once there are periodic oscillations in axial and lateral directions for a RF image, such as TO images, 2-D motions between consecutive images can be estimated using the APBE method. This estimator is briefly described here; more details are given in [17]. The pre-motion and post-motion images i_1 and i_2 with lateral modulations at consecutive times t_1 and t_2 can be assumed using a 2-D signal model modulated by spatial frequencies f_x and f_z, respectively [140]:

$$i_1(x, z, t_1) = w_1(x, z, t_1) \cos(2\pi f_x x) \cos(2\pi f_z z), \quad (5.8)$$

$$i_2(x, z, t_2) = w_2(x, z, t_2) \cos(2\pi f_x (x + U_x)) \cos(2\pi f_z (z + U_z)), \quad (5.9)$$

where w_1 and w_2 are two 2-D windows defined arbitrarily, $f_x = 1/\lambda_x$ and $f_z = 1/\lambda_z$, with λ_x and λ_z defined in (5.2), and U_x and U_z being lateral and axial components of the displacement, respectively. Note that phases in (5.8) and (5.9) do not change when the displacement is equal to one wavelength, thus the largest unbiased estimated displacement is limited to half a wavelength ($\lambda_x/2$ in the lateral direction and $\lambda_z/2$ in the axial direction).

Given the Fourier spectrum of i_1 or i_2, four single-quadrant analytic signals can be obtained by keeping only one quadrant and canceling other three quadrants. Since the 2-D

Fourier transform of real images is symmetric, only two analytic signals were considered. According to [140], the upper left and right quadrants of each spectrum were used. Two-dimensional displacements between consecutive images are associated with phases of analytic signals, as described here:

$$U_x = \frac{\Phi_1 - \Phi_2}{4\pi f_x}, \tag{5.10}$$

$$U_z = \frac{\Phi_1 + \Phi_2}{4\pi f_z}, \tag{5.11}$$

with

$$\Phi_1(x, \mathrm{z}) = \emptyset_{s11}(x, \mathrm{z}, t_1) - \emptyset_{s21}(\mathrm{x}, \mathrm{z}, t_2), \tag{5.12}$$

$$\Phi_2(x, \mathrm{z}) = \emptyset_{s12}(\mathrm{x}, \mathrm{z}, t_1) - \emptyset_{s22}(\mathrm{x}, \mathrm{z}, t_2), \tag{5.13}$$

where $\emptyset_{s11}$, $\emptyset_{s12}$ are extracted phases of abovementioned analytical images for the image i_1, and $\emptyset_{s21}$, $\emptyset_{s22}$ are phases of analytical images for the image i_2.

We can do the same process for (5.10) and (5.11) as we did for the LSME by introducing an affine model, and then rewriting these two equations for each pixel in a MW with $p \times q$ pixels. The affine APBE model is obtained by combining all equations into a matrix format, as described below in (5.14) and (5.15). The similar affine motion vector $\vec{m}$ was obtained by solving this over-determined equation system using the same robust weighted least square method, as we did for the LSME, unlike the classical least square fitting in [17], to provide a common framework of comparison. This constitutes a new contribution to the APBE (new implementation).

$$\begin{bmatrix} x_1 & z_1 & 1 \\ \vdots & \vdots & \vdots \\ x_{p\times q} & z_{p\times q} & 1 \end{bmatrix} \begin{bmatrix} s_{xx} \\ s_{xz} \\ U_x \end{bmatrix} = \frac{1}{4\pi f_x} \begin{bmatrix} \Phi_1(x_1, z_1) - \Phi_2(x_1, z_1) \\ \vdots \\ \Phi_1\left(x_{p\times q}, z_{p\times q}\right) - \Phi_2(x_{p\times q}, z_{p\times q}) \end{bmatrix}, \tag{5.14}$$

$$\begin{bmatrix} x_1 & z_1 & 1 \\ \vdots & \vdots & \vdots \\ x_{p\times q} & z_{p\times q} & 1 \end{bmatrix} \begin{bmatrix} s_{zx} \\ s_{zz} \\ U_z \end{bmatrix} = \frac{1}{4\pi f_z} \begin{bmatrix} \Phi_1(x_1, z_1) + \Phi_2(x_1, z_1) \\ \vdots \\ \Phi_1\left(x_{p\times q}, z_{p\times q}\right) + \Phi_2(x_{p\times q}, z_{p\times q}) \end{bmatrix}. \tag{5.15}$$

5.4.2.3 Time-ensemble approach

Because of the ultrafast CPWC imaging mode considered in this study, we could implement a time-ensemble approach into the APBE, as done for the LSME in [18].

Specifically, we assumed a constant motion over a given period of time $T = n_t.\Delta t$, where n_t is the number of successive frame pairs, and Δt is the time step between two consecutive frames. By combining these frames, the number of linear equations in the least square estimation is increased to $n_t \times n$, where *n* is the number of pixels in the MW of the estimator. In theory, the more time ensemble is used, better is the robustness of the least square estimation. However, the improvement in strain estimation is at the expense of computational time. For the LSME, we chose a time ensemble number of 8, as it provided the best compromise between accuracy and computational time [18]. For the developed APBE, we assessed estimation errors for different time ensembles (results not shown). We found exponentially decreasing strain estimation errors as a function of the time ensemble numbers. For example, an ensemble number of 12 provided 5% less estimation errors than n_t = 8 while increasing by 50% the computation time. Thus, to provide comparable results between APBE and LSME, we used n_t = 8 for both strain estimation methods.

5.4.2.4 Incompressibility constraint for the affine models

Arterial tissue incompressibility is a common assumption used in computational models of arteries [153, 154], motion compensation for strain imaging [51], ultrasound speckle tracking [52], angular strain compounding [35,53], and ultrasound modulography [54]. *Ex vivo* analyses have confirmed that arteries may be considered incompressible under physiological conditions [55,56]. Karimi *et al*. [57] recently showed that both excised healthy and atherosclerotic human coronary arteries are incompressible. The artery tissue is in fact slightly compressible but may be regarded as incompressible at small strains [55], which is attainable by the high frame rate plane wave imaging method used in this study. In addition, as described in Sections 5.5.5.1 and 5.5.2.1, we modeled the tissue as isotropic and quasi-incompressible (Poisson's ratio = 0.4995) for vascular simulations. For *in vitro* experiments, two phantoms were built with polyvinyl alcohol cryogel (PVA-C) following the manufacturing description of [58]. The Poisson's ratio of this material was estimated at 0.499 ± 0.001, which corresponds to an incompressibility condition [58].

The deformation of an incompressible tissue produces no volume change, which is formulated with the divergence of the displacement field U as $\nabla \cdot U = 0$. Under the condition

of 2D plane strain, the out of plane strain component is negligible and the divergence of U can be rewritten as $\nabla \cdot U = \frac{\partial U}{\partial x} + \frac{\partial U}{\partial z} = s_{xx} + s_{zz} = 0$. Consequently, under these assumptions:

$$s_{xx} = -s_{zz}. \tag{5.16}$$

By introducing (5.16) into (5.7) for the LSME, the motion vector $\vec{m}$ is reduced from six to five unknowns, and consequently the minimization process considered the following equation:

$$\begin{bmatrix} I_{x_1}z_1 & I_{x_1} & I_{z_1}x_1 & I_{z_1}z_1 - I_{x_1}x_1 & I_{z_1} \\ \vdots & \vdots & \vdots & \vdots & \vdots \\ I_{x_{p\times q}}z_{p\times q} & I_{x_{p\times q}} & I_{z_{p\times q}}x_{p\times q} & I_{z_{p\times q}}z_{p\times q} - I_{x_{p\times q}}x_{p\times q} & I_{z_{p\times q}} \end{bmatrix} \cdot \begin{bmatrix} s_{xz} \\ U_x \\ s_{zx} \\ s_{zz} \\ U_z \end{bmatrix} = -\begin{bmatrix} I_{t_1} \\ \vdots \\ I_{t_{p\times q}} \end{bmatrix}. \tag{5.17}$$

For the APBE, axial and lateral motion components were computed using (5.14) and (5.15), respectively, and then the lateral strain s_{xx} was replaced by the axial strain -s_{zz} when considering this assumption. Other displacement and strain components were assessed during the minimization process and used in these equations. In [18], it was shown that this incompressibility constraint in the LSME reduced the variability of principal strain estimations. In the current study, we aimed improving the quality of principal strain elastograms by also incorporating this constraint into the APBE. Reported results considered APBE and LSME implementations with and without the incompressibility constraint.

5.4.3 Implementation of elastography estimators and evaluation scheme

We adopted the implementation scheme of [18], which includes 7 steps. Briefly, a rigid registration using 2-D Fourier-based ensemble-correlations [155] was first performed for each small MW between pre- and post-deformed RF images to account for large displacements. Then, the affine motion vector $\vec{m}$ was computed using a weighted least-squares method [156] from registered pre- and post-deformed MWs. For the sake of a fair comparison, the same parameters were used for both estimators (LSME and APBE). Image pixels in a MW were weighted by a 2-D Gaussian function with a FWHM of 1.0×1.0 mm. Thus the MV size was set at 1.3×1.3 mm, which corresponds to 68 samples axially by 26 RF lines laterally, with the same 80% overlap in

axial and lateral directions. The spatial discretization of elastograms was thus 0.26×0.26 mm. A 90% overlap in time was chosen for the time-ensemble approach.

We filtered CPWC images to obtain TO images (labeled CPWC&TO). The APBE, the APBE using the time-ensemble approach, and the constrained APBE (*i.e.*, incompressibility constraint) with the time-ensemble approach were tested on CPWC&TO data (we used the following abbreviations (see also Table 5-1): CPWC&TO + APBE, CPWC&TO + APBE^{T} and CPWC&TO + APBE$^{T\&I}$). In addition, the LSME using the time-ensemble approach, with or without the incompressibility constraint, was tested with CPWC&TO and CPWC data (described as: CPWC&TO + LSME^{T}, CPWC&TO + LSME$^{T\&I}$, and CPWC + LSME$^{T\&I}$). The performance of six strategies (image beamforming schemes + estimators) was evaluated with simulations and *in vitro* phantom experiments.

5.5 Materials and methods

We simulated a heterogeneous vascular model with a mimicking atherosclerotic plaque and fabricated homogeneous vessel wall and heterogeneous phantoms for evaluation. Plane wave data were collected and beamformed using CPWC imaging at 21 angles, which allowed a frame rate of 500 s^{-1}. We used the full aperture to transmit and receive plane waves. Also, a rectangular window apodization function was used for beamforming. The RF images were reconstructed on a regular Cartesian grid (with 50×20 μm resolution). CPWC images were then filtered to obtain CPWC&TO images.

5.5.1 Simulation of a heterogeneous image sequence

5.5.1.1 Finite element model

A model of a carotid artery with soft and hard inclusions in a cross-sectional view was created using COMSOL Multiphysics (Structural Mechanics Module, version 3.5, COMSOL, France). The plaque geometry described in [157] was meshed with approximately 15,000, 6-node triangular elements. To avoid translations and rotations of the rigid body, a soft and compressible (elasticity modulus E = 1 Pa and Poisson's ratio $\gamma = 0.001$) layer of 1 mm thickness was added on the outer layer. This artificial outer contour was anchored and was not

considered in the elastography analysis. As reported, a wide range of Young's moduli, varying from 30 kPa to 270 MPa, for *ex vivo* or *in vivo* atherosclerotic tissues has been reported in the literature, depending on plaque internal structures and measurement methods [158]. In this study, a large soft necrotic core (E = 10 kPa) was embedded in a medium mimicking a fibrous plaque (E = 600 kPa). Four calcified inclusions (E = 5000 kPa) were also embedded within the plaque. The Poisson's ratio of all plaque components considered isotropic was fixed at 0.4995 (*i.e.*, incompressible). These mechanical parameters are close to those used in [159, 160]. Recently, similar parameters were also selected for elasticity reconstruction methods [161-163]. Displacements of the vessel wall between two successive image frames were computed using the finite element method (FEM). To consider realistic dynamic conditions, a systemic blood pressure waveform with minima and maxima at 80 and 120 mmHg (10 and 16 kPa) was applied to the simulated geometry. This waveform was discretized with 500 samples to simulate an ultrafast non-invasive ultrasound acquisition at a frame rate of 500 s^{-1}. The strain field was derived under plane strain conditions from computed displacement fields.

5.5.1.2 Acoustic models

The ultrasound simulation program Field II [164] was used to obtain RF images coupled with FEM simulated wall motions. The L14-5/38 linear array probe with 128 elements (Ultrasonix Medical Corporation, Richmond, BC, Canada) was simulated by considering a 7.2 MHz center frequency, a 70% fractional bandwidth (at -6 dB) and a sampling rate of 40 MHz. The bandwidth of that probe is between 5-14 MHz. The central frequency of 7.2 MHz allowed good resolution and acceptable grating lobes when using CPWC imaging [78]. The abovementioned vascular model included randomly distributed scatterers whose density was 100 per resolution cell [165] in a cross-sectional view. For CPWC beamforming, the full aperture was activated in transmission to create plane waves. The vascular model was static during emission angles changing from −10° to 10°. The plane wave data with different steering angles were beamformed and compounded to form pre-deformation images using the delay-and-sum algorithm [78]. To form post-deformation images, the displacement fields generated by the FEM were applied on this model and the plane wave data on the deformed model were beamformed and compounded using the same steering angles. The CPWC image sequence was

filtered to generate CPWC&TO images. All beamformed images were contaminated with white Gaussian noise at a SNR of 20 dB.

5.5.2 *In vitro* experiment description

5.5.2.1 Phantom fabrication

Two phantoms were built following the manufacturing description in [166]. The solution had a concentration of 10% by weight of polyvinyl alcohol dissolved in pure water and ethanol homopolymer. The weight percentage of added particles used as acoustic scatterers (Sigmacell cellulose, type 50, Sigma Chemical, St Louis, MO, USA) was 3%. The homogeneous phantom consisted in a 6 freeze-thaw cycles polyvinyl alcohol cryogel (PVA-C) material. The second phantom was constructed to mimic a heterogeneous vascular wall with a soft inclusion. The outer PVA-C layer was fabricated with 6 freeze-thaw cycles and the soft inclusion mimicking a lipid pool underwent 1 freeze-thaw cycle. The first homogeneous phantom without any inclusion had a modulus of 182 ± 21 kPa as measured by tensile test [166]. The heterogeneous phantom with a soft inclusion had a modulus of 25 ± 3 kPa [166], with the surrounding material at 182 ± 21 kPa.

5.5.2.2 Experimental setup

The experimental setup is analog to that illustrated in figure 2 of [18]. The intra-luminal pressure was monitored (Vivitro Labs Inc., Victoria, BC, Canada) and varied using a pulsatile pump (model 1421, Harvard Apparatus, Holliston, MA). Peak and minimum pressures were set at 120 and 60 mmHg, respectively, and an image sequence was acquired. To test the robustness of the different elastography estimators to different strains, the image sequence was down sampled using different time steps to produce frame rates from 500 s^{-1} to 9 s^{-1}.

5.5.2.3 Ultrasound data acquisition

Cross-sectional RF images were acquired with a Sonix Touch ultrasonic system (Ultrasonix Medical Corp.) equipped with a linear array probe of 128 elements (L14-5/38). Plane wave ultrafast data at different steering angles were stored on the Sonix DAQ multi-

channel system. A software development kit (TexoSDK, v6.0.1, Ultrasonix Medical Corp.) was used to generate and record plane wave data. Beamforming was performed in post-processing.

5.5.3 The choice of TO filtering parameters

As described in (5.3), the frequency pattern of the image formed by a TO filter is determined by two parameters, the expected lateral oscillation wavelength λ_x and the FWHM of the Gaussian envelope σ_x. Intuitively, smaller are λ_x and σ_x, wider is the spectrum of the filtered image and higher is the lateral TO frequency. However, too small λ_x and σ_x will filter most energy of the image and may induce the filter to only keep the noise. As a result, the proper TO filtering parameters λ_x and σ_x were determined via a simple simulation test. Two successive frames was selected from the simulated image sequence described in section 5.4.1 with a SNR of 20 dB. Different values of λ_x and σ_x were tested on this image pair 50 times. Parameters providing the least deviation between ground true FEM and computed elastograms were chosen for TO filtering in the remaining of this study. Considering the spectrum of compounded images and the window size of estimators, we set the test range of λ_x from 0.4 to 1 mm and that of σ_x from 0.2 to 1 mm, with increments of 0.1 mm.

5.5.4 Data analysis

5.5.4.1 Principal strain

The Cartesian strain tensor was transformed into the principal minor and major strain tensors, $\varepsilon_{min}, \varepsilon_{max}$, by using the following expression [167]:

$$\varepsilon_{min,max} = \frac{s_{xx}+s_{zz}}{2} \pm \sqrt{\left(\frac{s_{xx}-s_{zz}}{2}\right)^2 + \left(\frac{s_{xz}+s_{zx}}{2}\right)^2}, \tag{5.18}$$

where s_{xx}, s_{zz} are lateral and axial strains, and s_{xz}, s_{zx} are corresponding shear components. When we used the incompressibility constraint, the lateral strain component s_{xx} was replaced by $-s_{zz}$ in this equation.

In this study, otherwise specified, the principal strain map between consecutive frames was estimated for an image sequence. Then, principal strains were cumulated over the range of pressure considered. The largest cumulated strain map was chosen as the final elastogram.

5.5.4.2 Elastogram evaluation

To evaluate simulated elastograms, the normalized root-mean-square-error (NRMSE) between FEM and estimated principal strains was used:

$$NRMSE = \frac{\sqrt{\frac{\sum_{i=1}^{N}(ref_i - est_i)^2}{N}}}{ref_{max} - ref_{min}}, \tag{5.19}$$

where N is the number of pixels in an elastogram, ref is the ground truth principal strain from the finite element analysis, and est is the estimated strain from LSME or APBE algorithm.

Since the ground truth strain value is unknown for *in vitro* experiments, we chose the SNR as the evaluation metric of elastograms for homogeneous and heterogeneous phantoms. The CNR was also used for the evaluation of elastograms of the heterogeneous phantom.

$$SNR = 10log\left(\frac{\mu_{r_1}}{\sigma_{r_1}}\right) + 10log\left(\frac{\mu_{r_2}}{\sigma_{r_2}}\right), \tag{5.20}$$

$$CNR = 10log\left(\frac{2\left(\mu_{r_1} - \mu_{r_2}\right)^2}{\sigma_{r_1}^2 + \sigma_{r_2}^2}\right). \tag{5.21}$$

Here, μ_{r_1}, μ_{r_2} and $\sigma_{r_1}, \sigma_{r_2}$ are means and standard deviations of cumulated principal strains in selected ROIs 1 and 2.

5.6 Results

5.6.1 Optimal TO filtering parameters

The test results on TO filtering parameter selection using different pairs of λ_x and σ_x are represented in figure 5.1(a). The smallest estimation deviation for principal strains was obtained for $\lambda_x = 0.5$ mm and $\sigma_x = 0.4$ mm. These values were used in the remaining of this study. Figure 5.1(b) presents the corresponding filtering mask as described by (5.3).

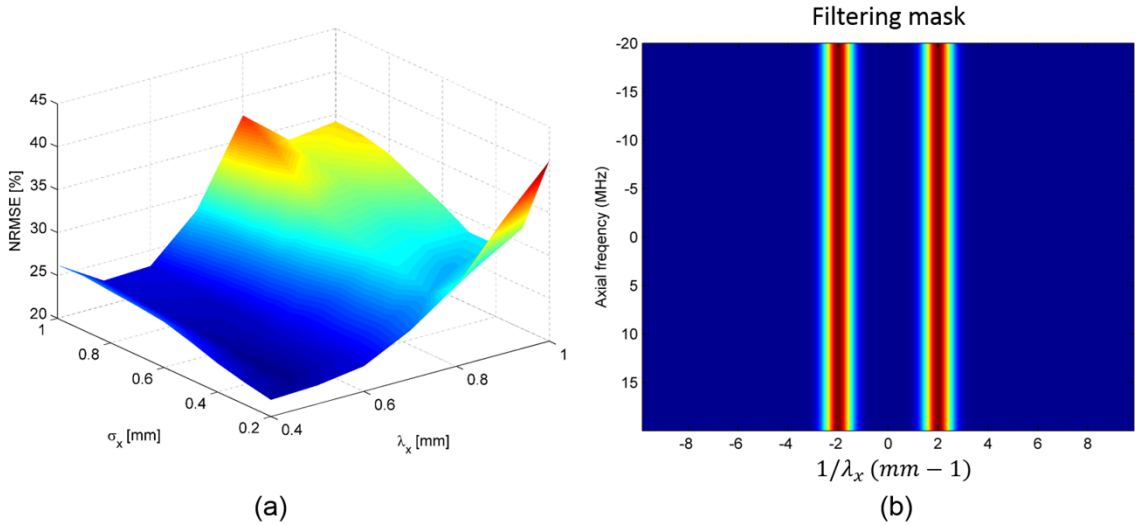

Figure 5.1 (a) The choice of TO filtering parameters using different pairs of λ_x and σ_x. Here the test range of λ_x is from 0.4 mm to 1 mm and that for σ_x is from 0.2 mm to 1 mm, with 0.1 mm increment. From this simulation, $\lambda_x = 0.5$ mm and $\sigma_x = 0.4$ mm provided the smallest estimation deviation (NRMSE) for principal strains and these values were chosen as the TO filtering parameters in our study. (b) The corresponding filtering mask.

5.6.2 The heterogeneous vessel simulation study

Figure 5.2(a)-(b) shows B-mode images of the heterogeneous artery simulation considering CPWC and CPWC&TO beamforming. Principal minor strains obtained with six configurations (CPWC&TO + APBE, CPWC&TO + APBE^{T}, CPWC&TO + APBE$^{T\&I}$, CPWC&TO + LSME^{T}, CPWC&TO + LSME$^{T\&I}$ and CPWC + LSME$^{T\&I}$) are shown in figure 5.2(d)-(i), respectively. We chose in figure 5.2(d) the time-ensemble length $n_t = 1$ (*i.e.*, no time-ensemble) for the APBE tested on CPWC&TO data (CPWC&TO + APBE), whereas $n_t = 8$ for other five configurations (as described in Section 5.4.2.3). Visually, figure 5.2(e) presents less estimation errors than Fig. 5.2(d), which suggests that the time-ensemble approach improved the estimation accuracy of the APBE. Around 12 and 8 o'clock (outside soft and hard inclusions), the principal minor strain is expected to decrease with radial distance from the lumen, which is known as the strain decay phenomenon [168]. The strain decay is difficult to appreciate from figure 5.2(d)-(f). Quantitatively, the APBE with the incompressibility constraint and using the time-ensemble approach tested on CPWC images with TOs (figure 5.2(f)) provided the smallest estimation error (NRMSE = 10.6%) when compared with the APBE with

the time-ensemble approach tested on CPWC images with TOs, CPWC&TO + APBE^{T} (figure 5.2(e), NRMSE = 13.0%) and the APBE tested on CPWC images with TOs, CPWC&TO + APBE (figure 5.2(d), NRMSE = 14.2%), which confirms that the combination of the time-ensemble approach and incompressibility constraint improved the performance of the APBE. With the LSME, the principal minor strains in figure 5.2(g)-(i) provided more homogeneous and clear outlines of the soft inclusion than APBE elastograms. Moreover, the strain decay at 12 and 8 o'clock is observed. The performance of the LSME, with and without the incompressibility constraint, tested on CPWC images with and without TOs (CPWC&TO + LSME^{T}, CPWC&TO + LSME$^{T\&I}$ and CPWC + LSME$^{T\&I}$) is overall comparable, with NRMSE at 9.0%, 8.6% and 8.4%, respectively.

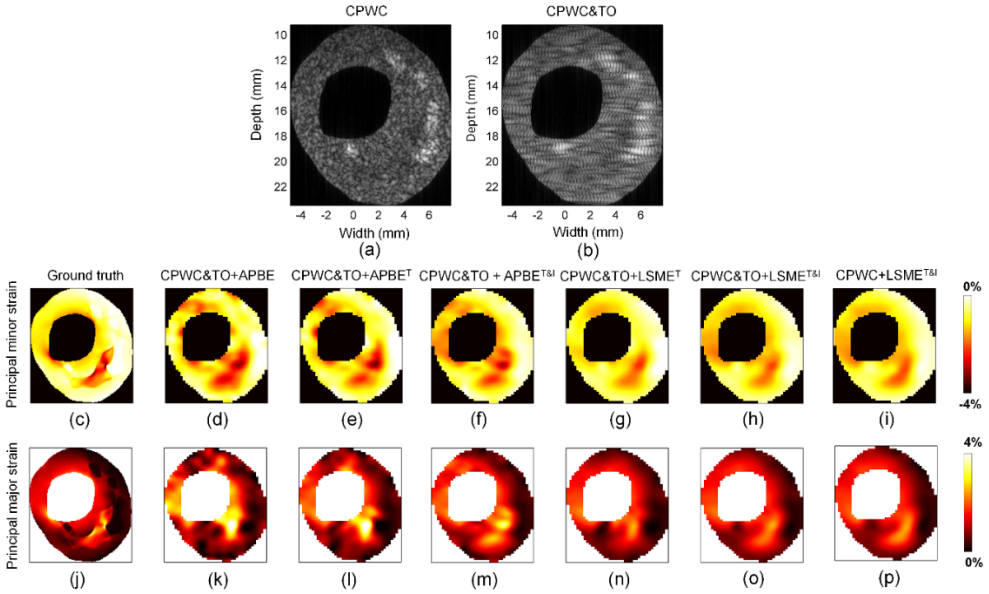

Figure 5.2 B-mode images and principal strains for a simulated vascular phantom with one soft inclusion and four hard inclusions. First row: the CPWC image and CPWC&TO image. Second row: ground truth of the principal minor strains from finite-element model and the principal minor strain estimated with the APBE on CPWC&TO data, the APBE using the time-ensemble approach on CPWC&TO data, the APBE using the incompressibility constraint and the time-ensemble approach on CPWC&TO data, the LSME using the time-ensemble approach on CPWC&TO data, the LSME using the incompressibility constraint and the time-ensemble approach on CPWC&TO data, and the LSME using the incompressibility constraint and the time-ensemble approach on CPWC data, whose NRMSE are 14.2%, 13.0%, 10.6%, 9.0%, 8.6%, 8.4%, respectively. Third row: ground truth of the principal major strains from finite-element model and the principal major strain estimated with the APBE and LSME using the same strategies, whose NRMSE are 17.4%, 14.5%, 12.9%, 9.6%, 9.4%, and 9.5%, respectively.

Regarding the principal major strain, the same conclusions apply. The APBE with the time-ensemble approach (figure 5.2(l)) showed less estimation artifacts than APBE without time averaging (figure 5.2(k)). However, both panels (k) and (l) did not delineate properly the soft inclusion around 4 to 6 o'clock. With the incompressibility constraint (panel (m)), the outline of the soft inclusion was better depicted. The NRMSE confirmed those visual observations; normalized errors were 17.4%, 14.5% and 12.9% for panels (k)-(m), respectively. With the LSME, the incompressibility constraint, CPWC&TO + $LSME^{T\&I}$ (figure 5.2(o)) and CPWC + $LSME^{T\&I}$ (figure 5.2(p)), allowed better outlines of the soft inclusion than the implementation without this constraint, CPWC&TO + $LSME^{T}$ (figure 5.2(n)). LSME provided better results compared with the three APBE implementations, with NRMSE at 9.6% (panel (n) with TO beamforming), 9.4% (panel (o) with TO beamforming), and 9.5% (panel (p) with no TO), respectively.

5.6.3 *In vitro* experiments

5.6.3.1 The homogeneous vascular phantom study

Figure 5.3(a)-(c) shows a picture, and cross-sectional CPWC and CPWC with TOs B-mode images of the homogeneous phantom without any inclusion. As done for the simulation study, the following description compares principal strains of six APBE and LSME implementations. APBE results in panels (d)-(f) confirmed the simulation study. Indeed, the time-ensemble approach and incompressibility constraint improved principal minor strain estimates but several artifacts are noticed on those elastograms. More consistent estimates were obtained with the LSME. The strain decay phenomenon is clearly seen in panels (g)-(i). Visually, a more homogeneous strain texture was obtained with the LSME that considered the time-ensemble and incompressibility constraint, and CPWC beamforming (*i.e.*, the implementation of [18], see panel (i)). To evaluate quantitatively the performance of those implementations, two regions of interest were selected to calculate the SNR (dashed green lines in figure 5.3(i)). One was selected as a 4-mm radius circle surrounding the lumen, whereas the other was an arc from 3 to 8 o'clock 5 mm away from the lumen center. SNRs in figure 5.3(d)-(i) are 11.1 dB, 11.3 dB, 12.0 dB, 15.9 dB, 14.2 dB and 16.5 dB, respectively. The best SNR

was obtained with the implementation of the LSME with the time-ensemble and incompressibility constraint on CPWC data (CPWC + LSME$^{T\&I}$).

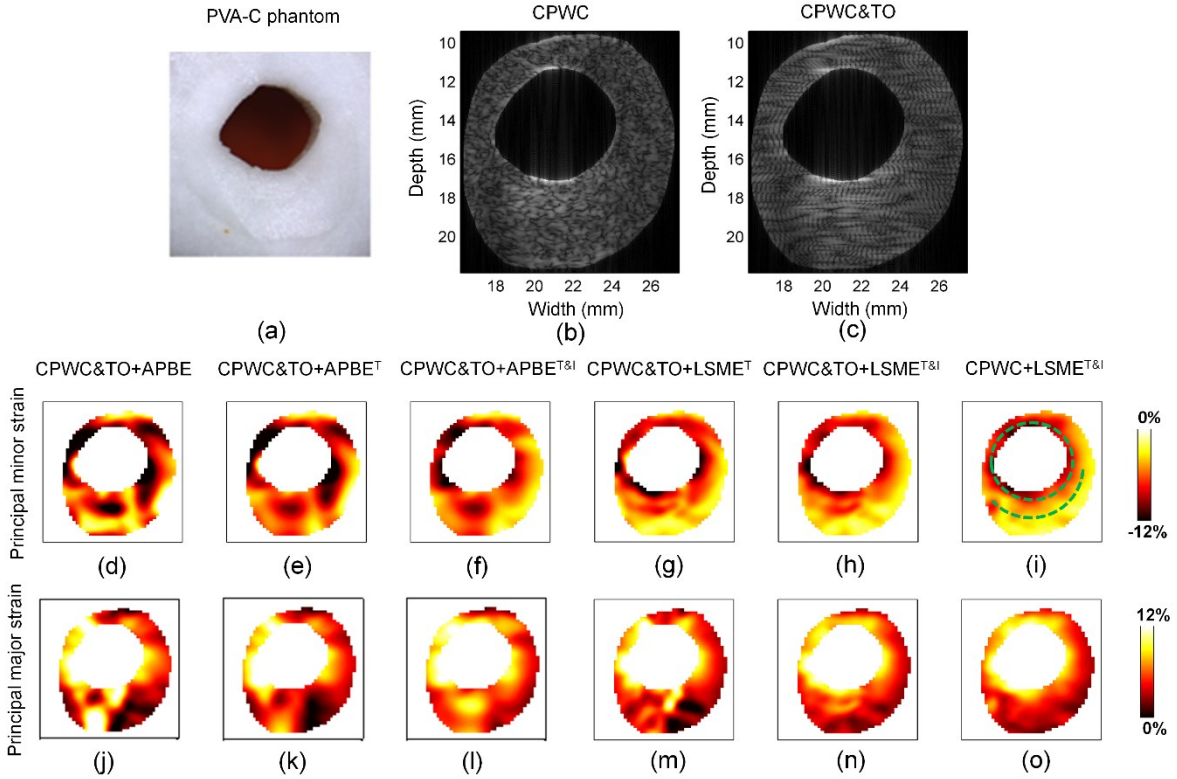

Figure 5.3 B-mode images and principal strains of a homogeneous phantom in vitro experiment. First row: the cross-section image of the phantom, the CPWC image and CPWC&TO image. Second row: the principal minor strains estimated with the APBE on CPWC&TO data, the APBE using the time-ensemble approach on CPWC&TO data, the APBE using the incompressibility constraint and the time-ensemble approach on CPWC&TO data, the LSME using the time-ensemble approach on CPWC&TO data, the LSME using the incompressibility constraint and the time-ensemble approach on CPWC&TO data, and the LSME using the incompressibility constraint and the time-ensemble approach on CPWC data, whose SNRs are 11.1 dB, 11.3 dB, 12.0 dB, 15.9 dB, 14.2 dB, 16.5 dB respectively. Third row: the principal major strains estimated with the APBE and LSME using the same strategies, whose SNRs are 7.2 dB, 7.5 dB, 12.0 dB, 8.9 dB, 14.2 dB, and 16.5 dB, respectively.

Regarding principal major strains of figure 5.3(j)-(o), visual observations are similar to those reported for principal minor strain elastograms. Overall, artifacts are observed on all strain maps and transverse oscillation beamforming seemed to emphasize the variance of both APBE and LSME estimators. With TO, the implementation of the incompressibility constraint (figure 5.3(l) and (n)) provided more consistent estimation at 5 o'clock compared with cases without

that constraint (figure 5.3(k) and (m)). The best result was obtained with the LSME with the time-ensemble and incompressibility constraint on CPWC data, as confirmed by SNR results. On panels (j) to (o), SNRs are 7.2 dB, 7.5 dB, 12.0 dB, 8.9 dB, 14.2 dB and 16.5 dB, respectively.

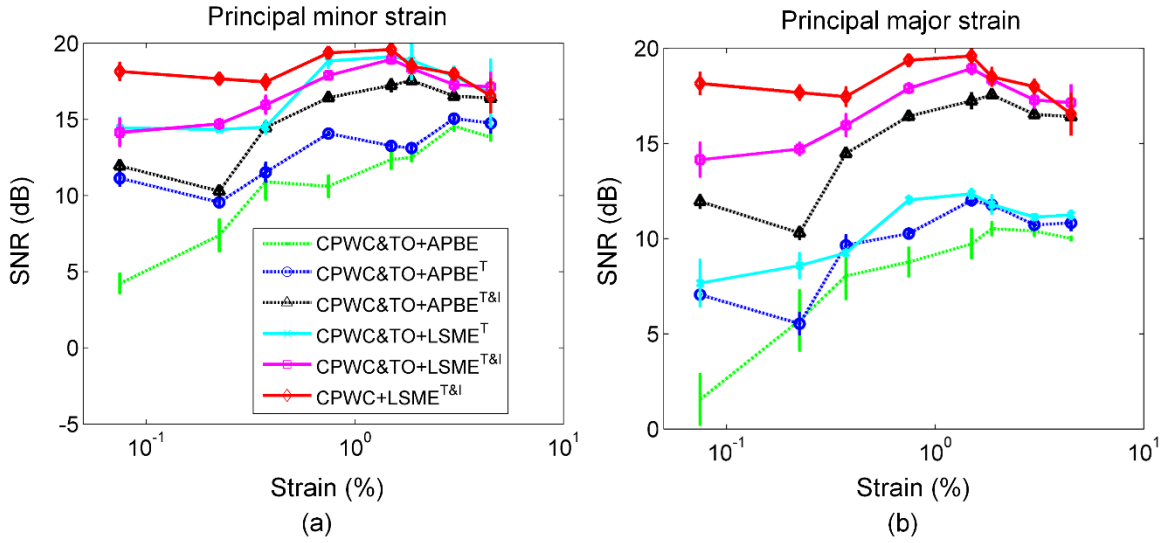

Figure 5.4 SNRs calculated from principal strains estimated with CPWC&TO + APBE, CPWC&TO + APBE^{T}, CPWC&TO + APBE$^{T\&I}$, CPWC&TO + LSME^{T}, CPWC&TO + LSME$^{T\&I}$, and CPWC + LSME$^{T\&I}$ over a range of applied strains from 0.07% to 4.5%. (a) Principal minor strains. (b) Principal major strains. Five realizations were considered.

Figure 5.4 presents the SNR analysis on principal strains for a wide range of applied strains (from 0.07% to 4.5%). Those results are confirming observations of figure 5.3 on cumulated strain maps at a frame rate of 500 s^{-1}. Except for the highest strain of 4.5%, CPWC beamforming with LSME considering the time-ensemble and incompressibility constraint provided the best SNRs. The worse performance was obtained with APBE on CPWC images with TOs (CPWC&TO). The time-ensemble approach and incompressibility constraint improved SNRs of principal strains for both APBE and LSME. Especially, as seen in figure 5.4(b), all implementations of the incompressibility constraint provided higher SNRs for principal major strains than implementations without that constraint. Differences in performance tended to decrease as the applied strain was increased.

5.6.3.2 The heterogeneous phantom study

Figure 5.5 shows visual assessment of the heterogeneous phantom with a soft inclusion under the lumen, B-mode images using both beamforming approaches, and cumulated principal strain maps. Regarding principal minor strains, fewer artifacts are seen when the time-ensemble and then the incompressibility constraint were added to the APBE estimator. When compared with LSME implementations (panels (g)-(i)), more deformations are noticed within the soft inclusion for the different APBE estimates (panels (d)-(f)). In general, with the exception of a few artifacts at 3 o'clock, the soft inclusion was well delineated with LSME implementations. Some overestimation of the inclusion dimension is nevertheless noticed with the LSME implementation on CPWC data (CPWC + $LSME^{T\&I}$). For quantitative analyses, 5 small rectangles of 0.5 mm × 0.5 mm with the same distance away from the lumen center were selected (see white ROIs and the manual segmentation of the inclusion on panel (o)). Three ROIs were chosen within the soft inclusion that was manually segmented from B-mode images to calculate the SNR. The two others were selected out of the soft inclusion to calculate the CNR together with the above three ROIs. SNRs from left to right in Fig 5.5(d)-(i) were 7.6 dB, 9.5 dB, 18.3 dB, 12.5 dB, 19.4 dB and 21.1 dB, respectively. CNRs were -5.2 dB, 4.1 dB, 10.2 dB, -2.6 dB, 11.5 dB and 16 dB, respectively. According to SNR and CNR results, the best implementation is with the LSME considering the time-ensemble and incompressibility constraint on CPWC-beamformed data (*i.e.*, the benchmark reference of [18]).

Regarding principal major strains, similar to previous results, all APBE implementations with CPWC&TO beamforming did not allow identifying the soft inclusion precisely. A lot of artifacts are also noticed with the LSME tested on CPWC&TO images when the incompressibility constraint was ignored (panel m). With the incompressibility constraint, the LSME provided clearer depiction of the inclusion (panels n and o). SNRs in figure 5.5(j)-(o) were 9.7 dB, 11.5 dB, 18.3 dB, 12.6 dB, 19.4 dB and 21.1 dB, respectively. CNRs were -8.5 dB, 0.4 dB, 10.2 dB, 3.2 dB, 11.5 dB and 16.0 dB, respectively. Again, the LSME with the time-ensemble and incompressibility constraint with CPWC beamforming provided the best results among all implementations.

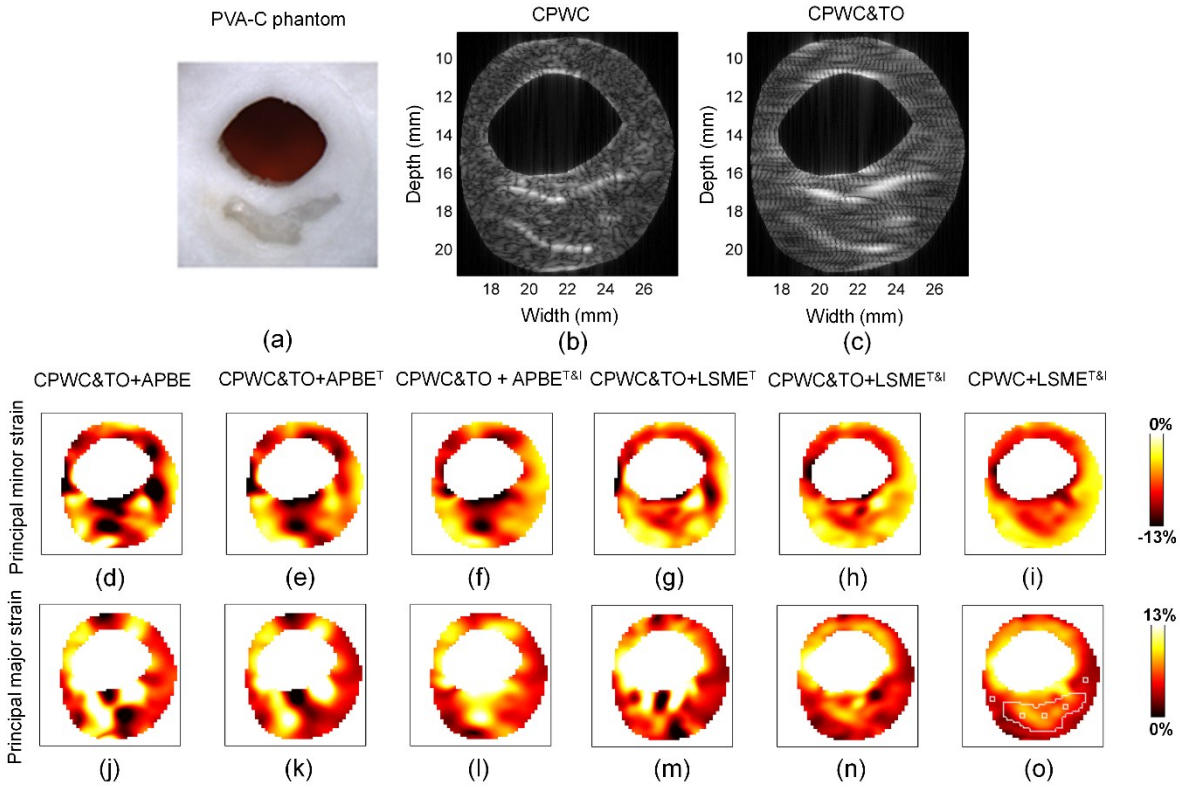

Figure 5.5 B-mode images and principal strains of a heterogeous phantom *in vitro* experiment. First row: the cross-section image of the phantom, the CPWC image and CPWC&TO image. Second row: the principal minor strains estimated with the APBE on CPWC&TO data, the APBE using the time-ensemble approach on CPWC&TO data, the APBE using the incompressibility constraint and the time-ensemble approach on CPWC&TO data, the LSME using the time-ensemble approach on CPWC&TO data, the LSME using the incompressibility constraint and the time-ensemble approach on CPWC&TO data, and the LSME using the incompressibility constraint and the time-ensemble approach on CPWC data, whose SNRs are 7.6.dB, 9.5 dB, 18.3 dB, 12.5 dB, 19.4 dB, and 21.1 dB, respectively, and CNRs are -5.2 dB, 4.1 dB, 10.2 dB, -2.6 dB, 11.5 dB, and 16 dB, respectively. Third row: the principal major strains estimated with the APBE and LSME using the same strategies, whose SNR are 9.7 dB, 11.5 dB, 18.3 dB, 12.6 dB, 19.4 dB, and 21.1 dB, respectively, and CNRs are -8.5 dB, 0.4 dB, 10.2 dB, 3.2 dB, 11.5 dB, and 16 dB, respectively.

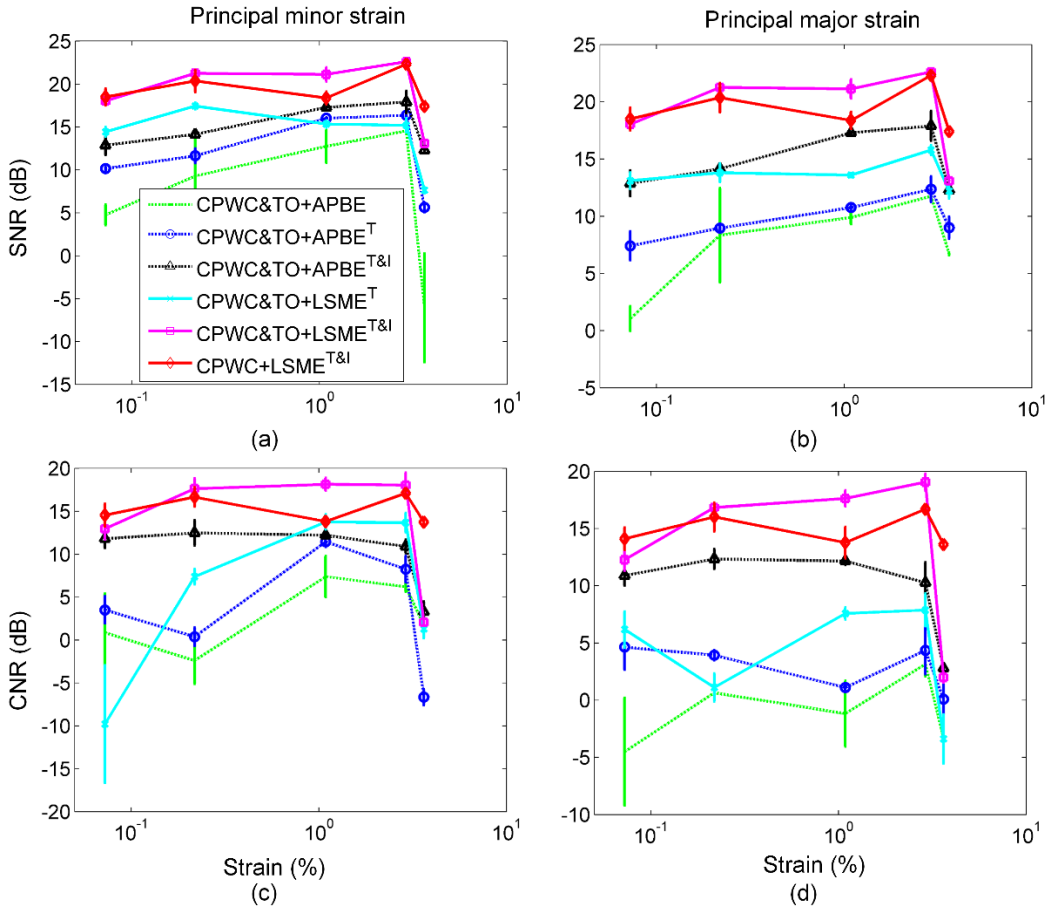

Figure 5.6 SNRs and CNRs calculated from principal strains estimated with CPWC&TO + APBE, CPWC&TO + APBE^{T}, CPWC&TO + APBE$^{T\&I}$, CPWC&TO + LSME^{T}, CPWC&TO + LSME$^{T\&I}$, and CPWC + LSME$^{T\&I}$ over a range of applied strains from 0.07% to 3.6%. (a), (b) SNRs for principal strains. (c), (d) CNRs for principal strains. Five realizations were considered.

SNR and CNR analyses of elastograms over different applied strains, from 0.07% to 3.6%, are given in figure 5.6. Overall, results are consistent with the visual observation of figure 5.5. LSME configurations considering the time-ensemble and incompressibility constraint applied on CPWC images with (CPWC&TO + LSME$^{T\&I}$) and without TOs (CPWC + LSME$^{T\&I}$) still provided the highest SNRs and CNRs. Principal strains from the APBE with the time-ensemble and incompressibility constraint on CPWC images with TOs (CPWC&TO + APBE$^{T\&I}$) had higher SNRs and CNRs than the other two APBE implementations, which confirms again that the time-ensemble and incompressibility constraint improve the performance of this estimator. Similar to figure 5.4(b), configurations considering the

incompressibility constraint (CPWC&TO + APBE$^{T\&I}$, CPWC&TO + LSME$^{T\&I}$ and CPWC + LSME$^{T\&I}$) presented higher SNRs for principal major strains. With a few exceptions, CNRs were also higher for both principal minor and major strains when the incompressibility constraint was used (figure 5.6(c) and (d)). Except for the minimum strain of 0.07%, at 500 images per second, and the maximum strain of 3.6%, transverse oscillation beamforming improved the performance of the LSME in terms of SNRs and CNRs for this specific phantom.

5.7 Discussion

The APBE proposed in [17] was applied on sectorial cardiac images of standard focusing with TOs. Although an affine model that could directly provide access to the deformation matrix was introduced, radial, circumferential and longitudinal strains were computed from the derivative of the displacement field. In the current study, we adapted the APBE for vascular applications by introducing a time-ensemble approach and an incompressibility constraint to directly assess deformations (no derivatives). The new APBE was shown to provide better strain estimations than the APBE implementation without time ensemble and incompressibility with simulations and *in vitro* experiments. Moreover, we combined CPWC and TO beamforming to obtain CPWC&TO images. The higher frame rate of CPWC&TO imaging compared with standard focusing imaging used in [17] provided smaller displacements between consecutive frames, which is an advantage since displacements must be smaller than half a wavelength for unbiased estimations with the APBE, as explained in Section 5.4.2.2.

In addition, we evaluated the performance of the developed APBE against LSME. Two of the three LSME implementations (CPWC&TO + LSME$^{T\&I}$ and CPWC + LSME$^{T\&I}$) outperformed the new APBE (CPWC&TO + APBE$^{T\&I}$) with simulations and *in vitro* experiments. CPWC + LSME$^{T\&I}$ provided better strain estimations than CPWC&TO + LSME$^{T\&I}$ for homogeneous phantom experiments; but comparable or worse performance for simulations of the heterogeneous vessel or for the heterogeneous phantom depending on strain values.

5.7.1 Influence of TO filtering on the quality of CPWC images

From simulations and *in vitro* results, as mentioned above, the APBE did not perform better than the LSME. TO filtering may be one of the reasons for that. Firstly, although TO filtering increases lateral textures of an image to facilitate lateral strain estimation, the filtering method used to create TOs is at the expense of losing in lateral resolution. Considering the point spread function (PSF) of a CPWC image (see figure 5.7(a)), we used (5.3) as a mask to multiply this spectrum to produce a PSF with TOs. This process is also viewed as a convolution of the PSF with a Gaussian function having two peaks modulated by λ_x and σ_x. The lateral width of the resulting PSF with TOs is expanded due to this Gaussian function convolution (see figure 5.7(b)). Moreover, TO filtering elevates the side lobe level despite narrowing the main lobe width.

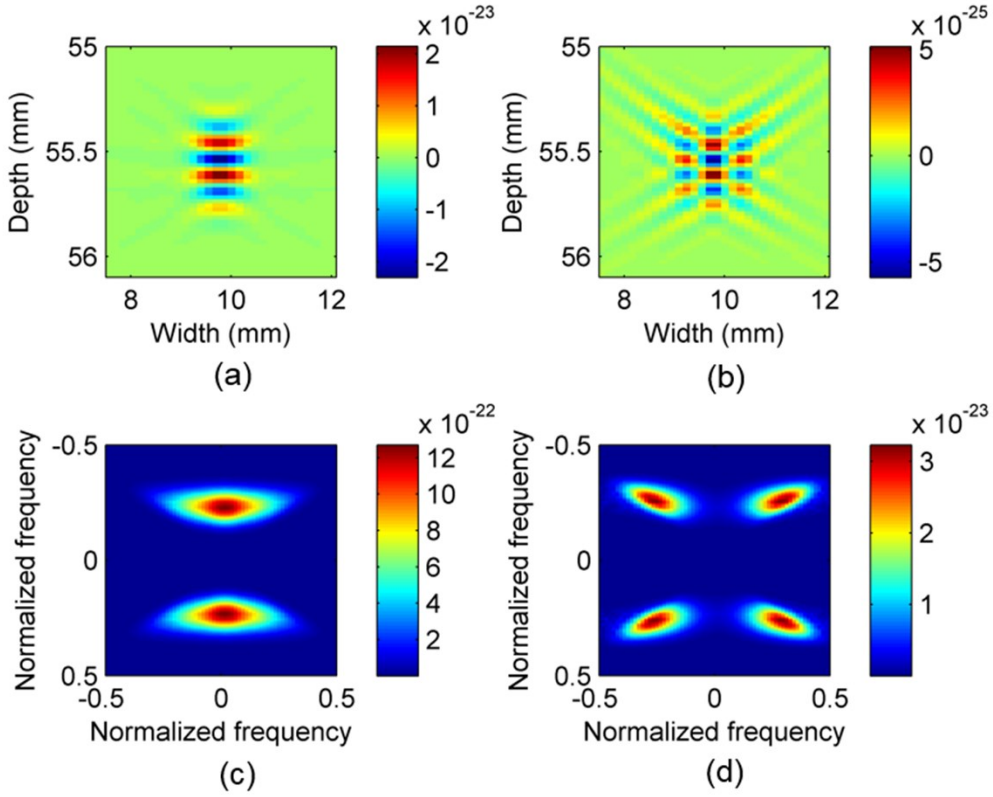

Figure 5.7 The point spread functions (PSF) and corresponding Fourier spectra of CPWC and CPWC&TO beamforming: (a) The PSF of the CPWC image, (b) the PSF of the CPWC&TO image, (c) the Fourier spectrum of (a), (d) the Fourier spectrum of (b).

Secondly, a CPWC image can be viewed as a wide band signal in the lateral direction from a Fourier spectrum analysis (see figure 5.7(c)). When the CPWC image is filtered by the band pass TO filter, the CPWC&TO image becomes a narrow band signal in the lateral direction (see figure 5.7(d)). The CPWC&TO spectrum is also subdivided from 2 to 4 main components, and as a consequence the spectral magnitude at given 2-D frequencies is reduced, which may violate the phase constancy assumption of the APBE, leading to less accurate strain estimations.

Likewise, the increased beam width and reduced spectrum magnitude of filtered TO images also violate the intensity constancy assumption of the LSME inducing less accurate estimations (see performances of CPWC&TO + $LSME^{T}$ or CPWC&TO + $LSME^{T\&I}$ versus CPWC + $LSME^{T\&I}$ for the homogeneous phantom results of figure 5.4). However, the increased lateral oscillations improve image gradients, which was beneficial for the LSME as comparable (figure 5.2) and even better (figure 5.6) performances were obtained when comparing CPWC&TO + $LSME^{T\&I}$ with CPWC + $LSME^{T\&I}$ when the tissue structure was complex and heterogeneous.

5.7.2 Influence of the affine model on the APBE

The APBE implemented without an affine model and known as the PBE was shown to be able to track accurately 2D and 3D trajectories with simulated and *in vitro* data [22, 109, 169]. The APBE proposed by others improved the lateral displacement estimation but provided a slightly less precise axial displacement measurement than the PBE [17]. One possible reason reported in the latter study [17] is that the affine model is more complex and is more prone to over-fitting than the simple PBE model in the presence of noise. Likewise, the same reason may apply to strain estimations with the APBE in our study, which included a minimization process to assess all displacement and deformation components simultaneously. Although the affine model has a low bias due to a precise description of the tissue motion, the increasing model complexity may also bring a high variance in the presence of noise, as discussed earlier when interpreting the performance of CPWC&TO images.

5.7.3 Bias and variance of the two strain estimators

We hypothesize that the LSME providing better performance than the APBE could be due to the estimation variance. In the supervised learning field [170], the mean-squared error of a model prediction can be decomposed into the noise, the bias and the variance in the form: $\mathrm{MSE} = \mathrm{noise} + \mathrm{bias}^2 + \mathrm{variance}$. The noise term is the inherent noise that cannot be reduced. The bias term is referred to how far the prediction is from the true value. The variance term is how much the prediction varies over multiple realizations of the model. Regarding the LSME versus APBE, the maximum detectable displacement in one direction with the APBE is half the wavelength of the oscillations in that direction [169]. The estimation bias of the LSME is also related to the range of displacements. To better clarify this issue, two simple 1-D versions of APBE (phase-based) and LSME (optical flow-based) methods were used to estimate displacements between a pair of 1-D sinusoids under ideal condition (*i.e.*, no noise). The performance for different displacements is presented in figure 5.8. As seen, the optical flow LSME method can be viewed as a biased estimator [171], whereas the phase-based APBE method is able to provide unbiased estimations until the true displacement becomes less than half a wavelength [140]. When the true displacement is more than half a wavelength, the phase estimator provides aliased results. As also seen in figure 5.8, when the motion between consecutive frames is small enough (typically less than 0.2 λ) to be tractable using CPWC imaging, the bias of the LSME is small. Introducing a small bias into an estimator can reduce the estimation variance leading to an overall lower mean-squared error [172]. Therefore, we hypothesize that the reduced variance may account for the better performance of the LSME versus APBE.

Besides abovementioned possible reasons for the poorer performance of the APBE with TO beamforming, we also investigated the impact of heterodyning demodulation to see if this approach, instead of the frequency domain filtering strategy used to produce lateral oscillations, could improve strain results. Readers are referred to the Appendix for more details.

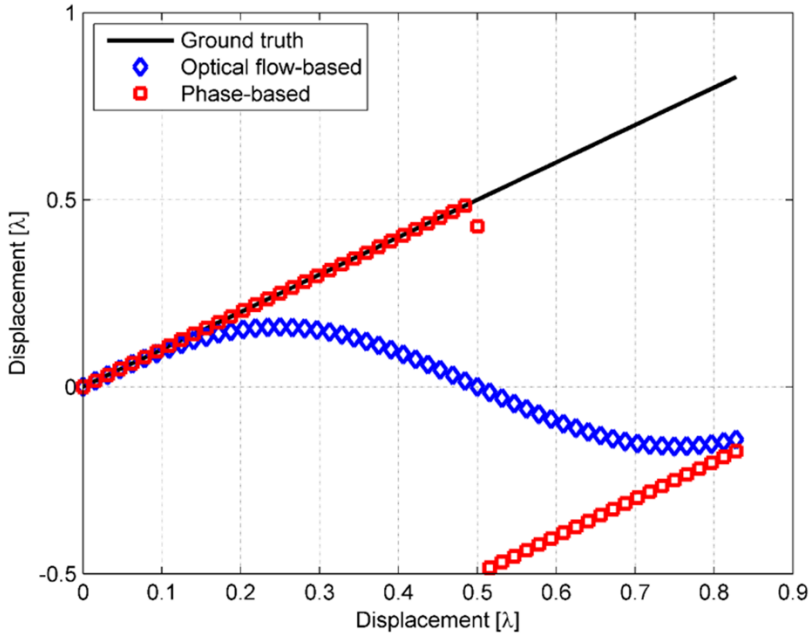

Figure 5.8 Performance of the phase-based and optical flow-based estimators to estimate the displacement between a pair of 1-D sinusoidal signals under ideal condition (no noise added) for different displacements along *x* and *y* axes.

5.7.4 Clinical value of this work

The second most common death cause is stroke accounting for about 1 of 10 deaths in the world [173]. Stroke is mainly induced by atherosclerotic plaque rupture [174]. A prone-to-rupture plaque is usually composed of a large lipid core covered by a thin fibrous cap [2]. In this study, a heterogeneous phantom with a soft inclusion was fabricated to simulate a pathological vulnerable condition. Two of the tested configurations (CPWC&TO + LSME$^{T\&I}$ and CPWC + LSME$^{T\&I}$) revealed the existence of the soft inclusion, as identified by large deformations on principal minor strain (Fig. 5.5(h), (i)) and principal major strain (Fig. 5.5(n), (o)) maps. For the homogeneous phantom (Fig. 5.3(a)), the anticipated strain decay was noticed on elastograms (Fig. 5.3 (h), (i), (n), (o)). Thus, we confirm that the proposed incompressibility constraint and time-ensemble approach with CPWC and CPWC&TO configurations may help identifying features of vulnerable plaques (soft inclusion) and the strain decay of normal vessel walls.

5.7.5 Limitations and perspectives

Lateral estimations (lateral strain and shear) of LSME and APBE were not as good as axial estimates due to the lower lateral resolution in ultrasound imaging. Because of the deleterious impact of this fact on principal strains, we used the incompressibility constraint to avoid using lateral strain estimates for some tested conditions. Nevertheless, we considered the lateral shear estimation that likely deteriorated the performance of both estimators. High resolution imaging approaches (*e.g.*, minimum variance beamforming [75, 175]) may be helpful to improve the lateral shear (and lateral strain) estimation. This is an avenue that may deserve to be explored.

In this study, we used the 2-D plane strain assumption for both LSME and APBE, and consequently the out-of-plane motion was not considered. This out-of-plane motion likely occurs if one considers non-homogenous human plaques and that motion may undermine the speckle or phase coherence in this direction. Fortunately, the models we presented here can be extended to 3-D. Combined with a 3-D data acquisition transducer, this would allow the LSME and APBE to estimate the full 3-D strain tensor while alleviating this assumption. In this study, the out-of-plane motion was also neglected for the incompressibility constraint. The isovolumic assumption used in Section 5.4.2.4 was indeed based on 3-D deformations. This is another aspect that would need to be further investigated.

5.8 Conclusion

In this paper, two affine model-based estimators were studied under the framework of high frame rate imaging. A time-ensemble approach and an incompressibility constraint were introduced to improve the performance of the affine phase-based estimator (APBE) for principal strain measurements. We also evaluated the performance of the APBE against the Lagrangian speckle model estimator (LSME), which also considered the time-ensemble strategy, with or without the incompressibility constraint. For all tested conditions, using the incompressibility constraint outperformed other implementations. In the simulation study, the LSME gave less principal strain estimation errors than the developed APBE. For the *in vitro* study, LSME elastograms provided higher SNRs for a homogeneous phantom, and higher SNRs and CNRs than the developed APBE over a wide range of strain values. In general, the LSME without TO

filtering provided better results. Nonetheless, comparable or better principal strain estimates could be obtained with the LSME and TO filtering in the case of complex and heterogeneous tissue structures (with the incompressibility assumption).

5.9 Acknowledgments

This work was supported by the Collaborative Health Research Program of the Natural Sciences and Engineering Research Council of Canada (CHRP-462240-2014) and the Canadian Institutes of Health Research (CPG-134748).

5.10 Appendix

5.10.1 Impact of heterodyning demodulation on strain performance of the APBE

The heterodyne demodulation has been shown recently to increase the lateral frequency and reduce the lateral beamwidth of the TO method [176, 177]. We thus applied this technique to see if it could also improve the performance of the APBE. We decomposed the APBE method to fit two heterodyning images whose oscillations are orthogonal. Specifically, only one quadrant of the spectrum of one analytic signal of the heterodyning demodulation was used. The strain components were derived using the affine model as we did in Section 5.4.2.2. The optimal parameters of TO images obtained with the heterodyne demodulation were also obtained using successive frames of the simulated carotid image sequence, which are $\lambda_x = 0.5$ mm and $\sigma_x = 0.3$ mm. Strain results are shown in figure 5.9. For these examples only, displacement and strain components without the incompressibility constraint are shown instead of principal strains to better appreciate the influence of the heterodyne demodulation on each motion component. The time ensemble approach was used.

As seen in figure 5.9, no improvements are observed for the APBE when using the heterodyne demodulation. Two reasons may account for this. Firstly, the APBE may not benefit from the double oscillation frequency attributed to the heterodyne demodulation. This may be because the APBE is different from the phased-based zero crossing method in which a higher phase slope is helpful to locate the peak of the complex correlation function. The APBE is

directly applied to analytic signals, which do not require a higher oscillation frequency to enable a higher phase slope. Secondly, the APBE was developed in the framework of RF data demodulated in each direction (as for TO images). The heterodyne demodulation decomposes a TO image into a lateral oscillation image and an axial oscillation image, which correspond to two RF images. For each of them, only two analytical phases are used instead of four, as it is done for TO filtered images. The APBE has to derive axial and lateral estimations from axial and lateral demodulated images, respectively. The absence of modulation in one direction has an influence on the accuracy in the other direction (roughly 20% increase in errors compared with TO images) [109].

Although we found that the heterodyne demodulation did not improve the performance of APBE, it does not contradict conclusions of [177]. Since the context is different (TO filtering versus TO heterodyne beamforming, linear array versus phased array, affine model-based method versus correlation-based method, etc…), the comparison might be misleading because different types of images and estimators were considered. Firstly, in [177], the conclusion was based on the Cramer-Rao Lower Bound (CRLB) formulation to predict the minimum attainable standard deviation of the jitter of displacement estimates of an unbiased motion estimator. Three parameters determine the jitter in the CRLB equation, the decorrelation, frequency content and SNR of beamformed signals. Our affine-based estimators (APBE and LSME) are not correlation-based methods so decorrelation was not computed. Moreover, the LSME is a biased estimator which requires good image gradient correlation instead of image intensity correlation. Secondly, in the current study, we derived strains using an affine model and a minimization procedure. It is a nonlinear process that is more complex than deriving displacements. The conclusions on displacement estimations may thus not be applicable. According to results reported in this section, we judged inappropriate to also test the LSME estimator with heterodyne demodulated images.

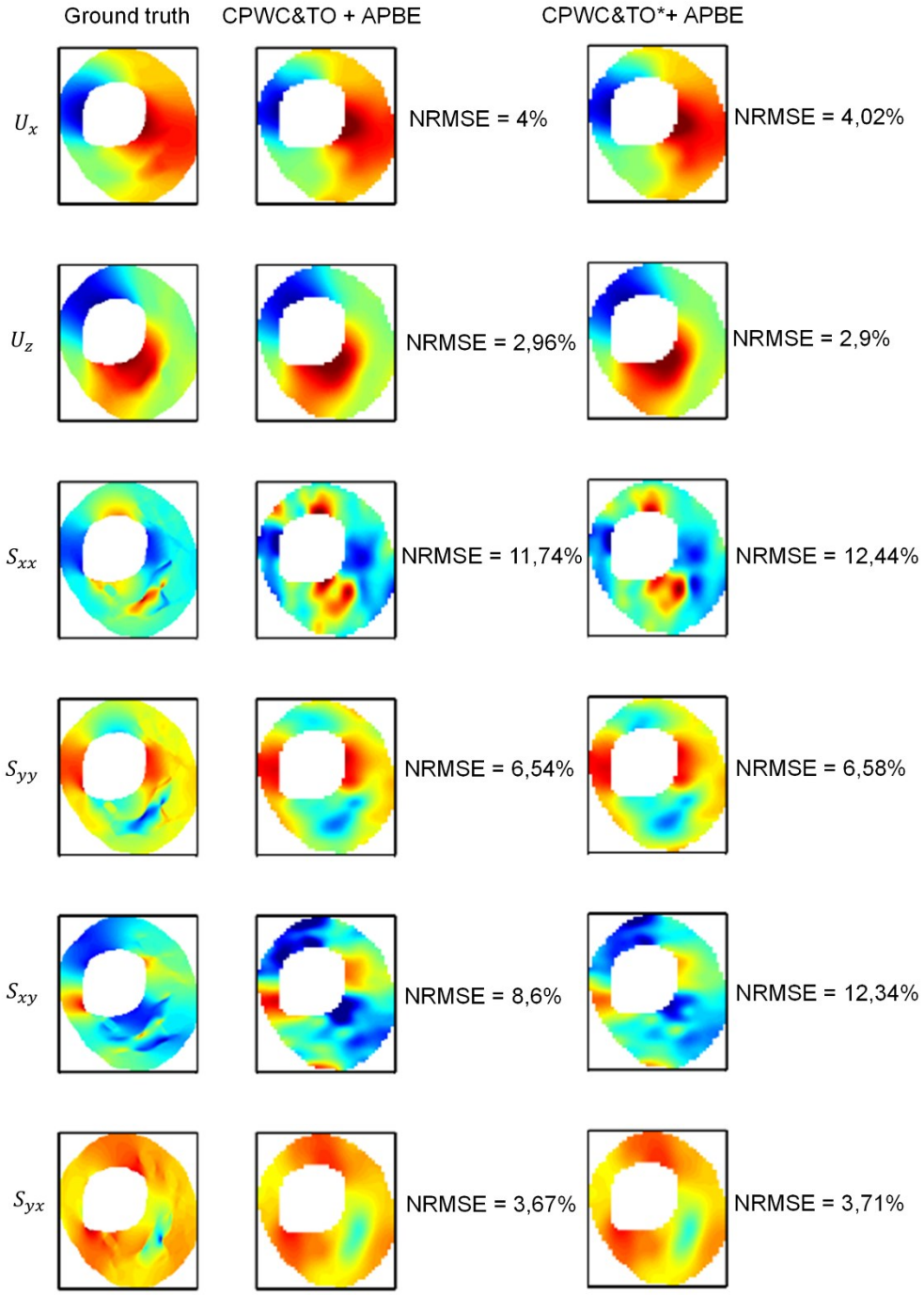

Figure 5.9 Ground truth of motion components from finite-element model (first column) and motion components estimated with the APBE on CPWC&TO beamformed data (second column) and CPWC&TO with heterodyne demodulation data (third column). Note that the incompressibility constraint was not used to better appreciate the influence of the heterodyne demodulation on each motion component. The strain components were also not combined to obtain principal strains for this example.

Chapter 6 : Investigation of out-of-plane motion artifacts in 2D noninvasive vascular ultrasound elastography

6.1 Introduction to manuscript

This chapter reproduces the content of a published article 'Investigation of out-of-plane motion artifacts in 2D noninvasive vascular ultrasound elastography' in the journal *Physics in Medicine & Biology* (Vol. 63, No. 24, p. 245003, 2018) by Hongliang Li, Boris Chayer, Marie-Hélène Roy Cardinal, Judith Muijsers, Marcel van den Hoven, Zhao Qin, Marc Gesnik, Gilles Soulez, Richard G. P. Lopata and Guy Cloutier after evaluation by a peer review committee.

The following is the order of authors for this published article and corresponding affiliations:

Hongliang Li[1,2], Boris Chayer[1], Marie-Hélène Roy Cardinal[1], Judith Muijsers[3], Marcel van den Hoven[3], Zhao Qin[1], Marc Gesnik[1], Gilles Soulez[2,4,5], Richard G. P. Lopata[3], and Guy Cloutier[1,2,4]

[1] Laboratory of Biorheology and Medical Ultrasonics, University of Montreal Hospital Research Center (CRCHUM), Montréal, QC, Canada;

[2] Institute of Biomedical Engineering, University of Montreal, Montréal, QC, Canada;

[3] Cardiovascular Biomechanics, Department of Biomedical Engineering, Eindhoven University of Technology, Eindhoven, Netherlands;

[4] Department of Radiology, Radio-Oncology and Nuclear Medicine, University of Montreal, Montréal, QC, Canada;

[5]Department of Radiology, University of Montreal Hospital, Montréal, QC, Canada.

The contributions of all authors of the published article is detailed below:

Hongliang Li: Designed and conducted *in vitro* experiments, implemented RF data acquisition and beamforming methods, performed the post-processing and analysis of *in vitro* data, developed post-processing algorithms and performed analysis of clinical data, drafted the manuscript and responded to the reviewer's comments of the article.

Boris Chayer: Contributed to designing the *in vitro* experimental setup, fabricated the carotid bifurcation phantom.

Marie-Hélène Roy Cardinal: Contributed to the interpretation of results and the revision of the manuscript.

Judith Muijsers: Contributed to the *in vitro* experimental protocol as a master intern from Eindhoven University of Technology.

Marcel van den Hoven: Designed the carotid bifurcation phantom as a master intern from Eindhoven University of Technology.

Zhao Qin: Contributed to plaque identification and segmentation of clinical data using an in house computer platform.

Marc Gesnik: Contributed to *in vitro* data acquisition through his expertise with the Verasonics research scanner.

Gilles Soulez: Performed clinical data acquisition and plaque segmentation and contributed to manuscript corrections.

Richard G. P. Lopata: Collaborated with LBUM as the supervisor of the two master interns from Eindhoven University of Technology and contributed to manuscript corrections.

Guy Cloutier: Supervised this work as the research director. Contributed to the interpretation of results as the project director. Corrected and finalized the manuscript for submission and revision.

6.2 Abstract

Ultrasound noninvasive vascular elastography (NIVE) has shown its potential to measure strains of carotid arteries to predict plaque instability. When two-dimensional (2-D) strain estimation is performed, either in longitudinal or cross-sectional view, only in-plane motions are considered. The motions in elevation direction (*i.e.*, perpendicular to the imaging plane), can induce estimation artifacts affecting the accuracy of 2-D NIVE. The influence of such out-of-plane motions on the performance of axial strain and axial shear strain estimations has been evaluated in this study. For this purpose, we designed a diseased carotid bifurcation phantom with a 70% stenosis and an *in vitro* experimental setup to simulate orthogonal out-of-

plane motions of 1 mm, 2 mm and 3 mm. The Lagrangian speckle model estimator (LSME) was used to estimate axial strains and shears under pulsatile conditions. As anticipated, *in vitro* results showed more strain estimation artifacts with increasing magnitudes of motions in elevation. However, even with an out-of-plane motion of 2.0 mm, strain and shear estimations having inter-frame correlation coefficients higher than 0.85 were obtained. To verify findings of *in vitro* experiments, a clinical LSME dataset obtained from 18 participants with carotid artery stenosis was used. Deduced out-of-plane motions (ranging from 0.25 mm to 1.04 mm) of the clinical dataset were classified into three groups: small, moderate and large elevational motions. Clinical results showed that pulsatile time-varying strains and shears remained reproducible for all motion categories since inter-frame correlation coefficients were higher than 0.70, and normalized cross-correlations between radiofrequency images were above 0.93. In summary, the performance of LSME axial strain and shear estimations appeared robust in the presence of out-of-plane motions (< 2 mm) as encountered during clinical ultrasound imaging.

6.3 Introduction

The second most common death cause is stroke and it is responsible for about 1 of 10 deaths in the world [173]. Atherosclerotic carotid plaque rupture is responsible for ≈20% of ischemic stroke [174]. Ultrasound noninvasive vascular elastography (NIVE) has shown its potential to evaluate plaque stiffness to predict plaque instability. NIVE utilizes the motion of the vessel wall caused by the natural cardiac pulsation to estimate strain fields of a plaque. Since the theoretical framework of NIVE was proposed [10], several noninvasive carotid strain algorithms have been developed and tested in phantom experiments, animal models or human subjects to identify vulnerable plaques [6, 25, 94, 178-181]. Hasegawa and Kanai proposed a phase-tracking method to estimate radial strain of a carotid arterial wall in longitudinal image view [182]. Some cross-correlation-based techniques have also been used to estimate two-dimensional (2-D) strain tensors [12, 137, 147, 183]. Recently, Porée *et al*. proposed a constrained and time-ensemble approach to improve the optical flow-based Lagrangian speckle model estimator (LSME) [18]. In that report, robust 2-D motion estimations in cross-sectional image view were obtained using coherent plane wave compounding imaging.

When 2-D strain estimation is performed in cross-sectional or longitudinal image view, only in-plane motions are estimated to depict axial (along the ultrasound beam) and lateral (perpendicular to it) deformations. Since carotid wall motions are three-dimensional (3-D) and periodic, they are not constrained to the imaging scan plane directions. A region of interest (ROI) may periodically be in and out of the scan plane due to vessel motion in elevation direction (*i.e.*, perpendicular to the imaging plane); this phenomenon is known as out-of-plane motion. Brusseau *et al*. [24] assessed the influence of out-of-plane motion on quasi-static elastography by tracking a 2-D ROI with a 3-D search scheme. For this purpose, a specific multi-row ultrasound probe was designed to acquire three adjacent imaging planes by activating different element rows sequentially. In the field of 3-D freehand breast or musculoskeletal ultrasound, speckle correlation of consecutive images was found to decrease with out-of-plane motions [184]. The elevational probe motion deduced from the speckle decorrelation has thus been used to provide probe tracking information for 3-D reconstruction [185-187]. For 2-D NIVE, it was also hypothesized that out-of-plane motions induced estimation artifacts due to reduced image correlation. Fekkes *et al*. [23] evaluated a cross-correlation-based 2D strain estimator on a 3-D atherosclerotic carotid artery simulation model considering out-of-plane motion. In that study, a longitudinal vessel motion [188] was simulated and superimposed on a model mimicking out-of-plane motion for strain estimation performed in cross-sectional view. To our knowledge, the influence of out-of-plane motion on the performance of carotid artery strain estimation has not yet been evaluated experimentally.

In this study, we designed an experimental setup to simulate periodic out-of-plane motion with varying magnitudes by an oscillating linear ultrasound probe. An *in vitro* study was conducted on a diseased carotid artery phantom with a soft plaque to evaluate LSME strain performance in longitudinal and cross-sectional views. In addition, the LSME accuracy regarding different degrees of out-of-plane motion was also investigated with a clinical dataset.

6.4 Materials and methods

6.4.1 Phantom fabrication

In vitro experiments were performed on a carotid bifurcation phantom with a soft inclusion made of polyvinyl alcohol cryogel (PVA-C) material. The geometry of the phantom was based on a CT scan of a healthy volunteer [189]. A custom made acrylonitrile butadiene styrene (ABS) mold was created by modifying the CT-scan lumen geometry to consider a 70% stenosis, using the 3-D printing technology (Dimension Elite, Stratasys Inc., Eden Prairie, MN, USA). A gap between the mold and the vessel core allowed pouring a PVA-C wall thickness of 2 mm through an inlet, as shown in figure 6.1(a). The solution was made of 10% by weight concentration of PVA-C dissolved in pure water and mixed with 3% by weight of 50 μm cellulose particles (Sigmacell, type 50, Sigma Chemical, St. Louis, MO, USA) to provide acoustic scatterers. The PVA-C solution was injected into the mold at a temperature of 45 ^{o}C. The viscous fluid prevented cellulose particles from sinking after injection. Once injected, the molded PVA-C was immediately put inside a freezer to undergo freeze-thaw cycles, which started with a plateau at -20 ^{o}C. The thin phantom wall froze in a few minutes, which also prevented sinking of cellulose particles. The phantom wall underwent 6 freeze-thaw cycles at temperature characteristics defined in [166].

The atherosclerotic plaque mold (green part in figure 6.1(a)) was 1 mm smaller than the stenosis allowing the fabrication of a 1 mm thick cap of PVA-C around the soft inclusion. A second inlet (plaque inclusion inlet in figure 6.1(a)) was added to the mold to inject liquid PVA-C to fill the cap. The PVA-C inside the inclusion underwent 1 freeze-thaw cycle to simulate a softer plaque in the upper wall of the internal carotid artery. Young's moduli of the phantom wall and soft inclusion measured by tensile test were 342 ± 24 kPa and 17 ± 3 kPa, respectively, which is consistent with previous results [166]. According to reported speeds of sound and sample densities for 1 and 6 freeze-thaw cycles [166], acoustic impedances of the soft inclusion and wall of the PVA-C phantom are estimated at 1.57×10^6 kg m^{-2} s^{-1} and 1.63×10^6 kg m^{-2} s^{-1}, respectively. A photograph of the fabricated diseased carotid bifurcation phantom is shown in figure 6.1(b). Phantom dimensions are listed in Table 6-1.

Table 6-1 The dimension parameters of a carotid bifurcation phantom with a soft plaque with 70% stenosis.

Dimension parameters	Dimensions
Wall thickness	2 mm
Length	123 mm
Common carotid artery (CCA) internal diameter	6 mm
Internal carotid artery (ICA) internal diameter	5 mm
External carotid artery (ECA) internal diameter	4 mm
Plaque size	10 mm × 4 mm

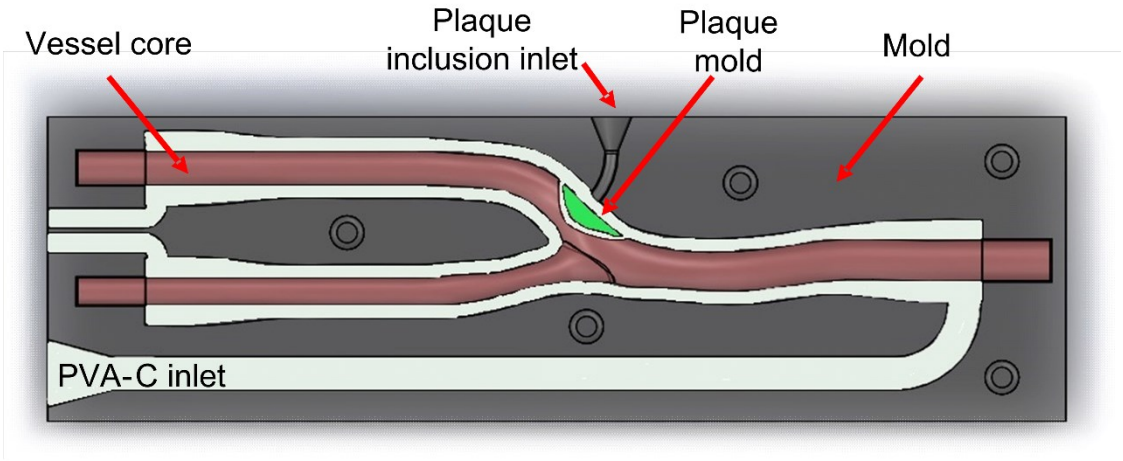

(a)

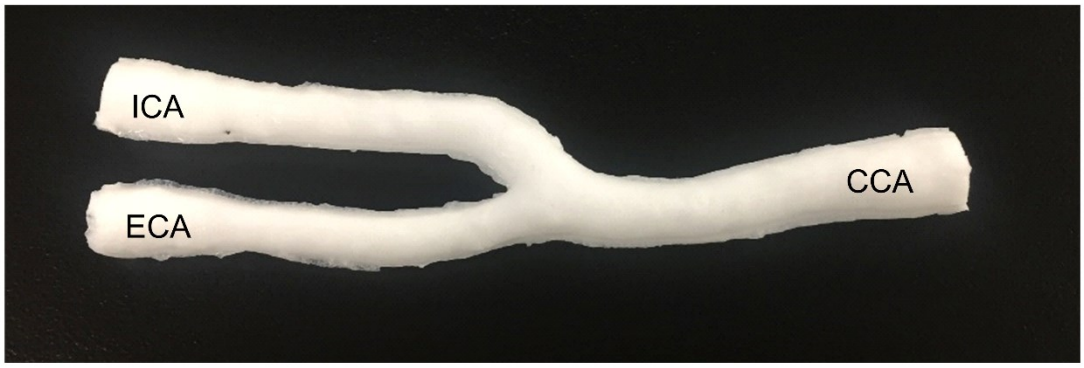

(b)

Figure 6.1 (a) The mold and vessel core of a carotid bifurcation phantom with a soft plaque with 70% stenosis. (b) The polyvinyl alcohol cryogel phantom.

6.4.2 *In vitro* experimental setup

As illustrated in figure 6.2, the carotid bifurcation phantom was suspended in a water tank and its lumen was filled with degassed saline (5% salt) to reduce specular reflection and

refraction at the phantom-liquid interface due to speed of sound differences between both media [12, 18, 145]. The speed of sound in 5% saline at room temperature (25°C) is 1550 m/s [190], which is comparable to speeds of sound of the PVA-C material after 6 freeze-thaw (1550 m/s) and 1 freeze-thaw (1525 m/s) cycles [166]. The phantom ends were connected to hard inlets of the water tank to reduce longitudinal motion from the pump pulsation. Ring clamps and threads were used at both ends of the phantom to tighten the vessel and prevent leaking. The intra-luminal pressure was varied using a pulsatile pump (model 1421, Harvard Apparatus, Holliston, MA, USA) and monitored using a ViVitest software system (Vivitro Labs Inc., Victoria, BC, Canada). Maximum and minimum pressures controlled by a water column connected to the main tubing were 110 and 65 mmHg, respectively. The stroke rate of the pulsatile pump was set to 72 beats per minute to simulate the resting heart rate of an adult.

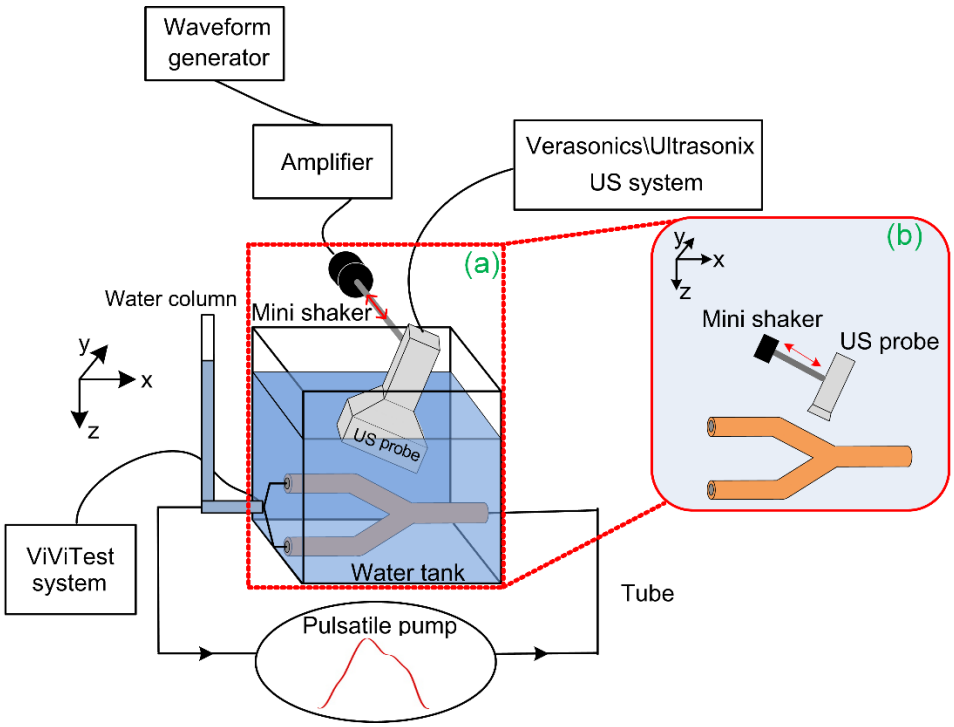

Figure 6.2 *In vitro* experimental setup diagram. Panel (a) demonstrates longitudinal view acquisitions. Panel (b) displays cross-sectional view acquisitions.

Panel (a) in figure 6.2 shows data acquisition in longitudinal view. A linear array transducer, whose scanning axis was parallel to the x direction of the setup, was attached to a mini-shaker (type 4810, Brüel and Kjær, Naerum, Denmark) to generate out-of-plane motions (for practical reason, we moved the probe instead of the vessel phantom). The mini-shaker was

driven to vibrate as a 1.2 Hz sinusoid. The frequency and trace of the out-of-plane motion were set by a waveform generator and magnitudes of vibration were adjusted by a power amplifier (type 2706, Brüel and Kjær, Naerum, Denmark). Three out-of-plane motion magnitudes were investigated: 1 mm, 2 mm and 3 mm. The magnitudes were calibrated using a sonomicrometry system (Sonometrics Corporation, London Ontario, Canada). Panel (b) in figure 6.2 presents data acquisition in cross-sectional view with the probe scanning axis parallel to the y direction. Other technical parameters were the same as longitudinal view acquisitions.

6.4.3 Image acquisitions and reconstructions

6.4.3.1 *In vitro* experiments

In vitro ultrafast plane wave data were acquired with a Verasonics research scanner (V1-128, Verasonics Inc., Redmond, WA, USA) at a sampling frequency of 20 MHz. The full aperture of a 5 MHz linear array transducer with 128 elements (ATL L7-4, Philips, Bothell, WA, USA) was used to transmit and receive plane waves, and a rectangular window apodization function was considered for beamforming. Radiofrequency (RF) data with eleven emissions between −5° to 5° with a 1° increment were beamformed using the Stolt's f-k migration [191], which allowed a frame rate of 400 s^{-1}. RF images were reconstructed on a regular Cartesian grid with 39×75 µm (axial × lateral) sampling distances. The duration of acquisitions was set to 2.5 s corresponding to three cycles of the pulsatile pump. There were thus 1023 frames in a whole image sequence.

6.4.3.2 Clinical study

To verify findings of *in vitro* experiments, we performed NIVE on a clinical dataset obtained from 18 recruited participants with carotid artery stenosis of 50% or greater. Exclusion criteria were severe vascular calcifications impeding Doppler imaging, and internal carotid artery (ICA) for which there was previous radiotherapy in the neck region, endarterectomy or stenting. The study was approved by the human ethical review board of the Centre Hospitalier de l'Université de Montréal. Participants signed an informed consent.

Data acquisition details followed procedures described in previous studies [70, 192]. Specifically, RF data of ICA plaques were acquired by an experienced radiologist. A Sonix

ES500 RP ultrasonic system (Ultrasonix Medical Corp., Richmond, BC, Canada) equipped with a L14-5/38 linear array probe (with 128 elements and a 7.2 MHz center frequency) was used. Both longitudinal and cross-sectional scans were performed at the plaque location. We used line-by-line focused imaging instead of coherent plane wave compounding beamforming, as in the *in vitro* phantom study, because clinical RF data were acquired between April 2005 to December 2010 [192]. RF signals were sampled at 20 MHz and reconstructed on a regular Cartesian grid with 39×150 μm (axial $\times$ lateral) sampling distances. The frame rate for RF data was between 19-25 Hz depending on depth of ultrasound images. RF sequences were acquired for 3-5 seconds. During the acquisition, once the plaque imaging view was localized, the radiologist held the probe static to reduce out-of-plane motions caused by the moving probe. Moreover, participants were asked to hold breath and keep still to avoid further motions between the probe and the carotid artery.

6.4.3.3 Comparison of experimental conditions

An additional line-by-line focused imaging *in vitro* phantom experiment was performed using the Sonix ES500 RP scanner (L14-5/38 probe) to clarify the probe independence on reported results. Additionally, to interpret differences between *in vitro* and clinical results (explained later in Discussion), a line-by-line focused imaging experiment on phantom was performed using the Verasonics scanner (L7-4 probe) to compare with coherent plane wave compounding (CPWC) imaging. To be consistent with the clinical study, line-by-line beamformed data in longitudinal view regarding out-of-plane motions of 1 mm, 2 mm and 3 mm were reconstructed at a resolution of 39×150 μm (axial $\times$ lateral) and a frame rate of 25 s^{-1}.

6.4.4 Noninvasive vascular elastography

To characterize complex and non-rigid plaque tissue motions, strain-based elastography was used. The optical flow based Lagrangian speckle model estimator (LSME) [18] is able to obtain axial strain and shear elastograms directly into a single minimization process. The optical flow model is described briefly in Appendix (see section 6.9.1) and more details can be found in [18, 25]. The implementation of this algorithm is briefly described here.

Firstly, contours of the vascular plaque on a single frame in the middle of the image sequence were manually drawn to generate a ROI. An automatic segmentation algorithm [193] was used to propagate the ROI on remaining frames. The ROI was subdivided into small measurement windows (MW). The MW size was set at 1.5×1.5 mm with the same 80% overlap in axial and lateral directions for *in vitro* measures, and at 1.5×3 mm with 95% and 90% overlaps in axial and lateral directions, respectively, for clinical data. The MW size and overlaps were kept the same as in previous clinical studies [70, 192]. Secondly, a rigid registration using 2-D Fourier-based ensemble-correlations [155] was performed for each small MW between pre- and post-deformed RF images to account for large displacements. Then, the axial strain and shear derived from the optical flow equation were computed using a weighted least-squares method [156] from registered pre- and post-deformed MWs. Finally, a sequence of 2-D axial strain and axial shear elastograms were used to calculate time-varying maximum and mean strain and shear curves. Only mean strains within ROIs were analyzed for the clinical dataset.

6.4.5 Data analysis

To evaluate the influence of *in vitro* out-of-plane motions on time-varying strain and shear curves, correlation coefficients between deformations without out-of-plane motion and different elevational motion magnitudes were computed. For example, to compute the correlation coefficient between elastography curves without out-of-plane motion (S0) and 1 mm out-of-plane motion (S1), two complete peak-to-peak cycles were selected from each curve. Elastography curve values (sampled at 400 Hz) of each cycle for S0 was used to calculate correlation coefficients with those of each cycle for S1. Thus, four correlation coefficients were obtained to compute the mean correlation coefficient and the standard deviation. The mean and standard deviation were not computed for S0 since only two cycles were available. The same procedure was used to correlate S0 with S2 (2 mm motion) and S3 (3 mm motion) acquisitions.

For the clinical study, out-of-plane motion is intrinsic due to vessel pulsation during ultrasound scan, which is impossible to determine with only 2-D cross-sectional or longitudinal image view. However, for an image sequence in longitudinal view, the out-of-plane motion in elevation can be estimated by the lateral translation of a plaque ROI in cross-sectional view. This can be done with 2-D block matching algorithms [194, 195]. In the current study, the range

of cumulated lateral translation (RoCLT) for each cardiac cycle was derived by implementing such block matching method. A 2-D cross-correlation-based algorithm [196] considering temporal intensity variation of the reference block, using Kalman filtering, was applied on reconstructed cross-sectional B-mode images. The mean RoCLT assessed over all available cardiac cycles of a participant was averaged and considered as an estimation of the out-of-plane motion of the same plaque in the corresponding image sequence in longitudinal view. Only longitudinal elastography results of the clinical dataset are reported in this study.

Unlike *in vitro* analysis where results could be compared between different out-of-plane motions and no motion, there was no reference to compare with (*i.e.*, no out-of-plane motion) for the clinical dataset. To assess the quality of strain estimation, two metrics were used to evaluate the reproducibility of strain curves, namely the correlation coefficient as for the *in vitro* study and the normalized cross-correlation (NCC), For the correlation coefficient, cycles of each strain curve were selected manually. Every two different cycles were used to calculate correlation coefficients. We also computed NCC between all pairs of consecutive RF images: the preceding image and the motion-compensated image, similar to [197, 198]. Specifically, a given i^{th} RF frame in an image sequence was warped into the $(i+1)^{\text{th}}$ RF frame coordinate system using the estimated 2-D motion field between i^{th} and $(i+1)^{\text{th}}$ frames. NCC between motion-compensated i^{th} RF image and $(i+1)^{\text{th}}$ RF image was calculated for the whole image sequence. In this study, the motion compensation process consisted in an affine model considering displacements and strains from LSME estimations. The rationale behind this metric is that less out-of-plane motion between two consecutive RF frames may provide higher NCC values since more robust 2-D motions were used for compensation. On the other hand, larger out-of-plane motion affecting strain estimation accuracy should be associated with smaller NCC values. Moreover, parts of strain curves associated with severe out-of-plane motion could be identified by the occurrence of small NCC values.

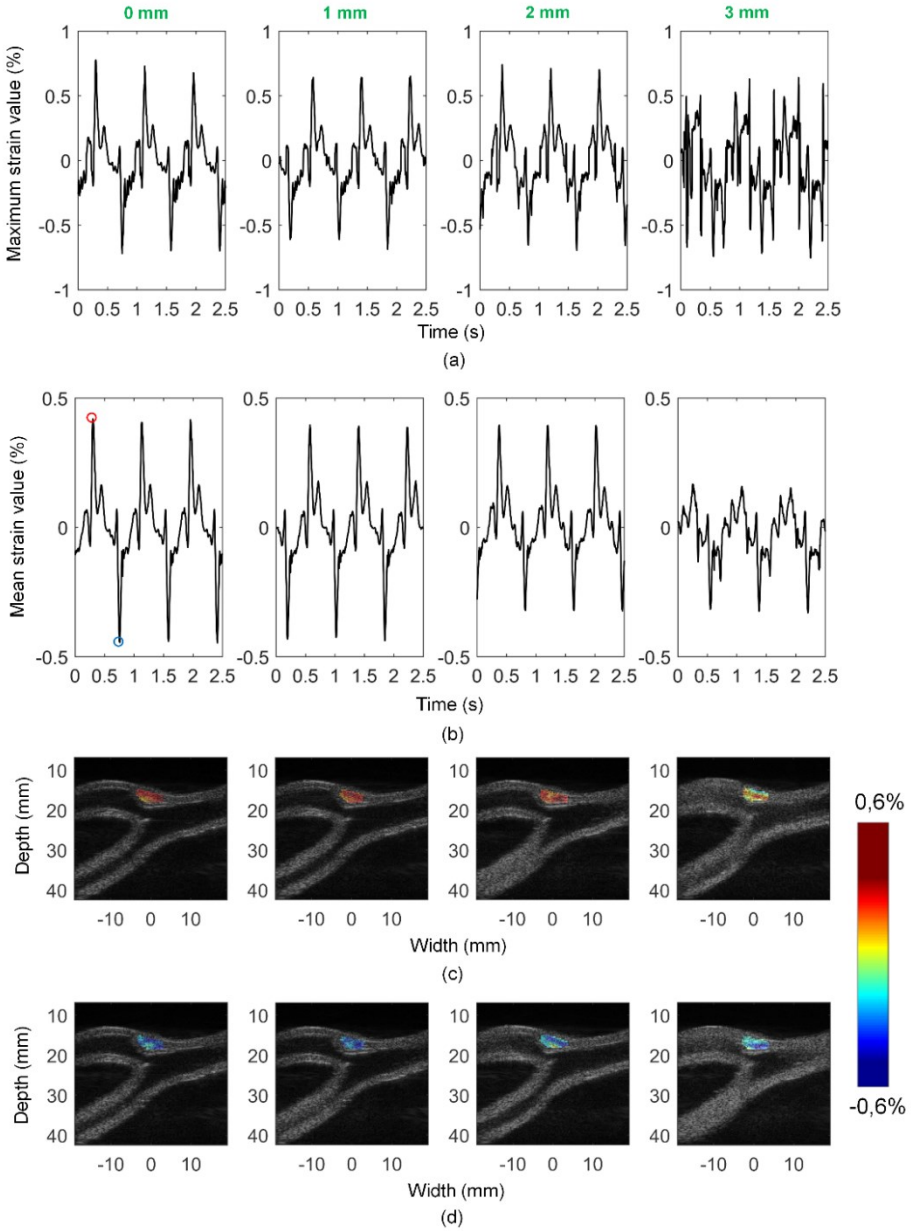

Figure 6.3 Time-varying maximum strain curves (a) and mean strain curves (b) in longitudinal view. The out-of-plane motions are 0 mm, 1 mm, 2 mm, and 3 mm respectively from left to right. (c) Axial strain maps at peak dilation for the first flow cycle (red circle in (b)) of the segmented plaque superimposed on the reconstructed B-mode images. (d) Axial strain maps at peak compression for the first flow cycle (blue circle in (b)) of the segmented plaque superimposed on the reconstructed B-mode images.

6.5 Results

6.5.1 Influence of out-of-plane motions on *in vitro* images in longitudinal and cross-sectional views

6.5.1.1 Longitudinal view image analysis

Figure 6.3(a) presents time-varying maximum strain curves (MaxSCs) for no motion and out-of-plane motions of 1 mm, 2 mm and 3 mm. Qualitatively, MaxSCs with 1 mm and 2 mm out-of-plane motions are similar to the curve without motion. However, it is more difficult to identify pulsatile cycles on MaxSC with 3 mm out-of-plane oscillations. Figure 6.3(b) shows similar results for time-varying mean strain curves (MeanSCs). Although three pulsatile cycles can be identified on MeanSC for the 3 mm out-of-plane motion, peak values are smaller than in the case of no motion. Axial strain maps superimposed on reconstructed B-mode images are shown in figure 6.3(c) and (d).

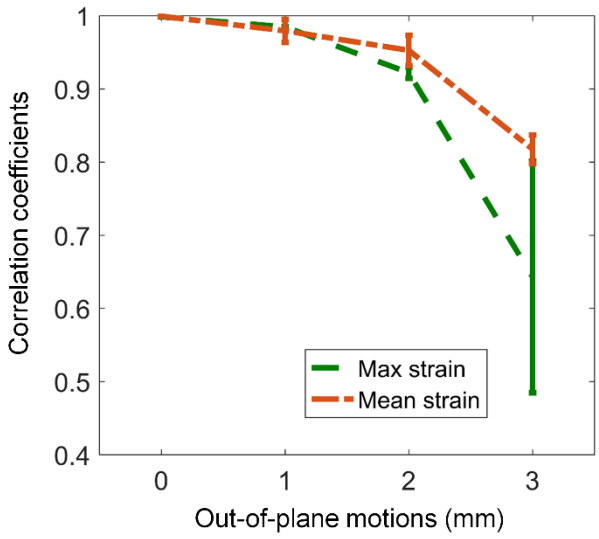

Figure 6.4 Correlation coefficients of time-varying maximum and mean strain curves regarding different out-of-plane motions in longitudinal view. For maximum strain curves, the correlation coefficients are 0.998, 0.985 ± 0.004, 0.920 ± 0.008 and 0.643 ± 0.158 respectively for out-of-plane motions of 0 mm, 1 mm, 2 mm and 3 mm. For mean strain curves, correlation coefficients are 0.999, 0.979 ± 0.016, 0.953 ± 0.021 and 0.818 ± 0.019 respectively for out-of-plane motions of 0 mm, 1 mm, 2 mm and 3 mm.

Figure 6.4 shows correlation coefficients of MaxSC and MeanSC for out-of-plane motions of 0 mm, 1 mm, 2 mm, and 3 mm. Out-of-plane motions up to 2 mm gave correlation coefficients higher than 0.9 for MaxSC. Higher correlation coefficients were obtained for MeanSCs. The general trend is a reduction of correlation coefficients with increasing out-of-plane motions. Correlation coefficient results for maximum and mean axial shears are given in Appendix (figure 6.11).

6.5.1.2 Cross-sectional view image analysis

Results of time-varying MaxSCs revealed similar behavior for 0 mm and 1 mm out-of-plane motions (figure 6.5(a)). Although some outliers are identified for the 2 mm oscillating motion, the overall trend is also similar. By comparison, there are more outliers on MaxSC for the 3 mm out-of-plane motion, which hinders the periodicity of the strain curve. Panel (b) depicts results for time-varying MeanSCs. With 1 mm and 2 mm out-of-plane motions, results look consistent with that without motion. At 3 mm motion, it is again difficult to identify pulsatile cycles. Axial strain maps superimposed on reconstructed B-mode images are seen in figure 6.5(c) and (d) for two moments within a cycle.

Correlation coefficients of MaxSCs and MeanSCs for different out-of-plane motions in cross-sectional view are shown in figure 6.6. Overall, conclusions are similar to those reported for longitudinal view data. At the largest motion of 3 mm, MaxSCs were still severely affected as in longitudinal view; mean correlations were around 0.6. Figure 6.12 in Appendix shows correlation coefficients for time-varying maximum and mean shear curves in cross-sectional view.

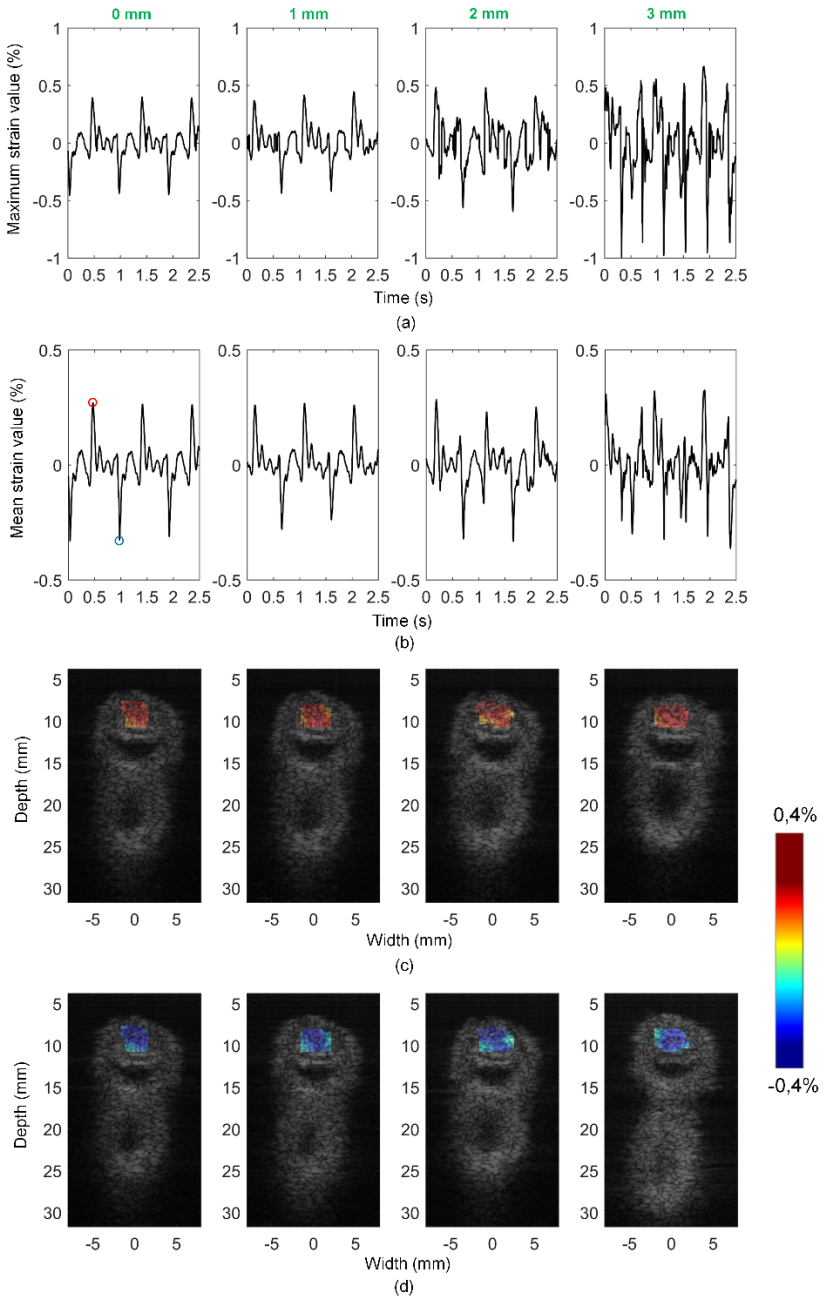

Figure 6.5 Time-varying maximum strain curves (a) and mean strain curves (b) in cross-sectional view. The out-of-plane motions are 0 mm, 1 mm, 2 mm, 3 mm respectively from left to right. (c) Axial strain maps at peak dilation for the first flow cycle (red circle in (b)) of the segmented plaque superimposed on the reconstructed B-mode images. (d) Axial strain maps at peak compression for the first flow cycle (blue circle in (b)) of the segmented plaque superimposed on the reconstructed B-mode images.

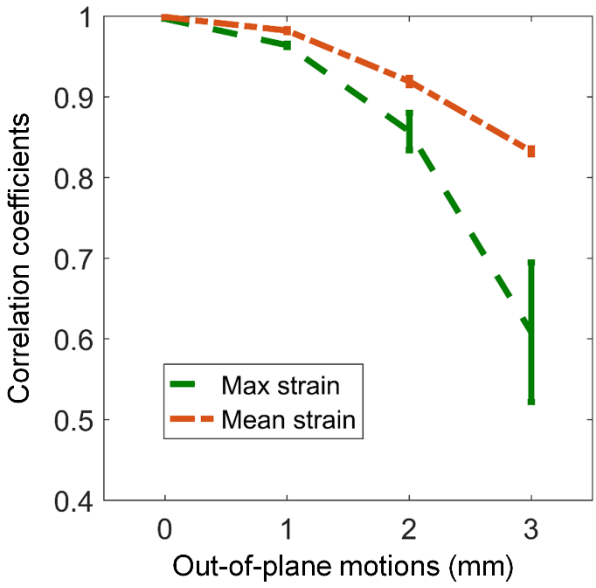

Figure 6.6 Correlation coefficients of time-varying maximum and mean strain curves regarding different out-of-plane motions in cross-sectional view. For maximum strain curves, the correlation coefficients are 0.997, 0.964 ± 0.002, 0.857 ± 0.023 and 0.608 ± 0.087 respectively for out-of-plane motions of 0 mm, 1 mm, 2 mm and 3 mm. For mean strain curves, the correlation coefficients are 0.999, 0.982 ± 0.002, 0.919 ± 0.005 and 0.832 ± 0.004 respectively for out-of-plane motions of 0 mm, 1 mm, 2 mm and 3 mm.

6.5.2 Influence of out-of-plane motions on clinical images

In this study, the mean carotid plaque lateral displacement in cross-sectional view for 18 participants was 0.63 mm, with maximum and minimum values at 1.04 mm and 0.25 mm, respectively. Those values were considered as the anticipated out-of-plane motions in longitudinal view. We divided them into three groups, small, moderate and large out-of-plane motions, with equal range (around 0.27 mm). Examples of MeanSCs from clinical images with small, moderate and large out-of-plane motions are shown in figure 6.7(b), (d) and (f), respectively. Corresponding axial strain maps at peak compression of the segmented plaque superimposed on reconstructed B-mode images are presented in figure 6.7(a), (c) and (e). As indicated by the orange dotted line in figure 6.7(b), (d) and (f), NCC curves revealed higher values after dilation and compression peaks of strain curves. Figure 6.8 shows correlation coefficients of mean strain curves and mean NCC values for clinical data with small, moderate

and large out-of-plane motions. Figure 6.13 presents correlation coefficients of mean shear curves and mean NCC values for the same motion categories.

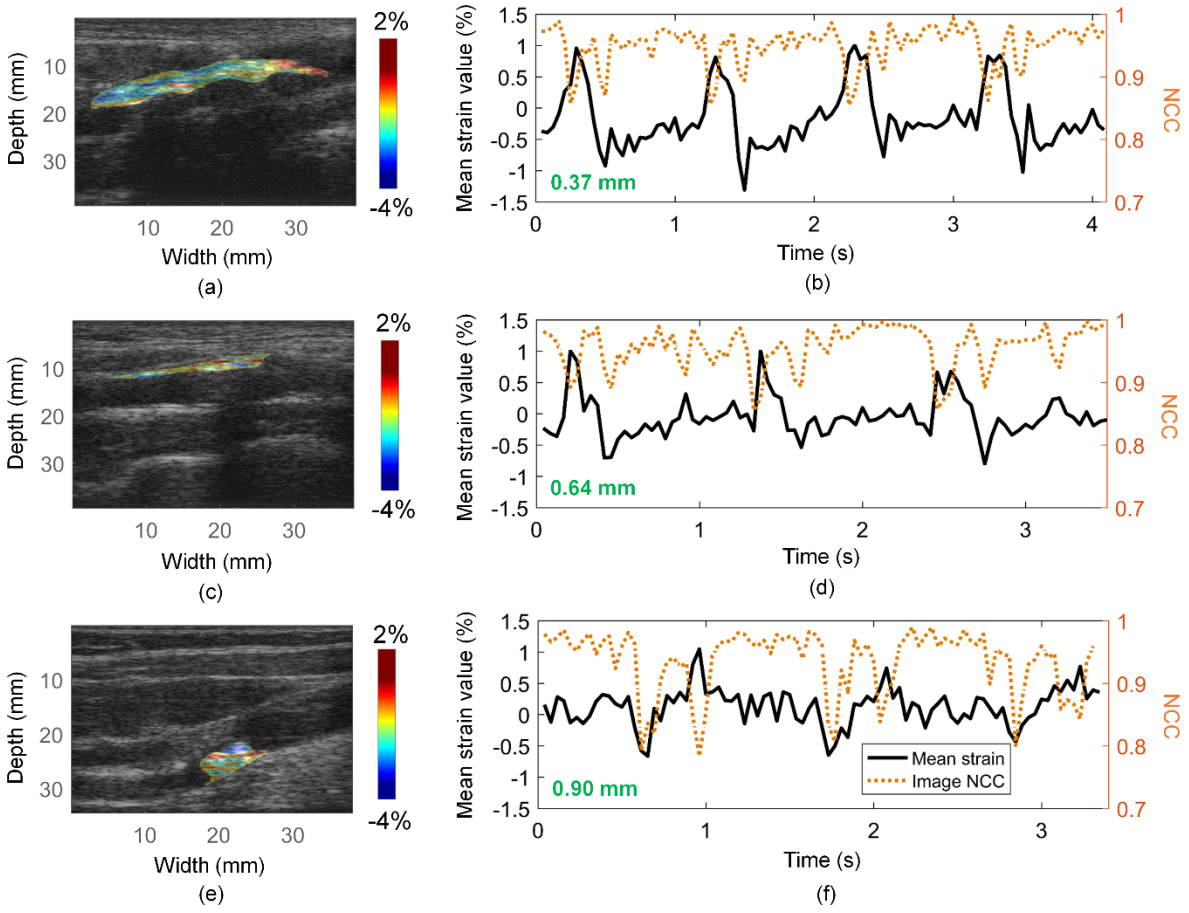

Figure 6.7 Examples of axial strain maps at peak compression of the segmented plaques superimposed on reconstructed B-mode images of clinical data with mean out-of-plane motions of 0.37 mm (a), 0.64 mm (c) and 0.90 mm (e). Corresponding time-varying mean strain curves and normalized cross-correlation (NCC) curves of motion-compensated RF images (b), (d) and (f).

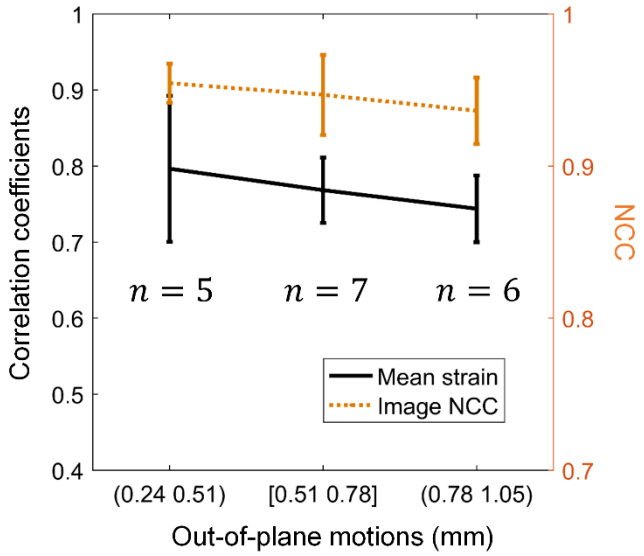

Figure 6.8 Correlation coefficients of mean strain curves regarding out-of-plane motion ranges of 0.24 - 0.51 mm, 0.51 - 0.78 mm, and 0.78 – 1.05 mm, whose sample sizes are 5, 7 and 6 participants, respectively. Correlation coefficients are 0.796 ± 0.096, 0.768 ± 0.043 and 0.744 ± 0.044, respectively, and corresponding mean normalized cross-correlation (NCC) values are 0.954 ± 0.013, 0.947 ± 0.026 and 0.936 ± 0.022 for these three groups of out-of-plane motions.

6.5.3 Evaluation of the probe independence

Figure 6.4 above presented *in vitro* experimental results on axial strains using the L7-4 probe (5 MHz). To confirm that those results are not probe dependent and could be used to interpret clinical data acquired with the L14-5/38 probe (7.2 MHz), figure 6.9 shows correlation coefficients of MaxSC and MeanSC for different out-of-plane motions using that latter probe coupled to the Ultrasonix scanner. Similar to experiments with the L7-4 probe, both MaxSC and MeanSC were characterized by correlation coefficients higher than 0.83 for 1 and 2 mm out-of-plane motions, confirming the robustness of strain estimations.

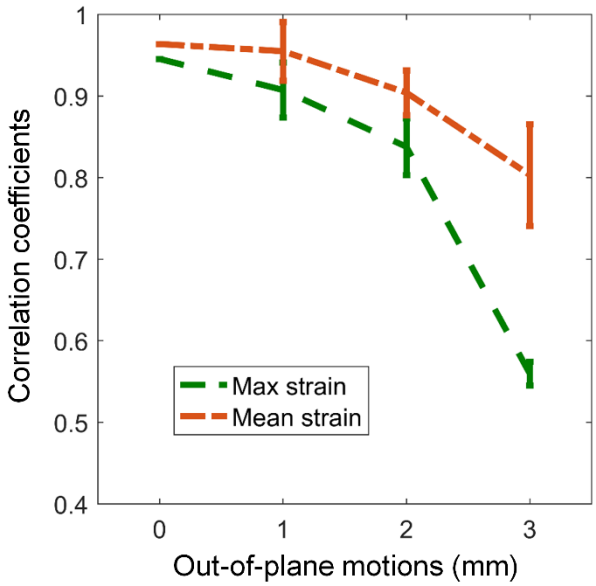

Figure 6.9 Correlation coefficients of time-varying maximum and mean strain curves regarding different out-of-plane motions in longitudinal view using the Ultrasonix scanner (L14-5/38 probe) for *in vitro* experiments. For maximum strain curves, correlation coefficients are 0.945, 0.907 ± 0.034, 0.838 ± 0.035 and 0.560 ± 0.015 for out-of-plane motions of 0 mm, 1 mm, 2 mm and 3 mm, respectively. For mean strain curves, correlation coefficients are 0.964, 0.955 ± 0.036, 0.904 ± 0.028 and 0.803 ± 0.062 for the same out-of-plane motions, respectively.

6.5.4 Comparison of different beamforming strategies

Correlation coefficients of maximum and mean axial strains determined using the Verasonics scanner (L7-4 probe) for CPWC and line-by-line focused imaging beamforming are presented in figure 6.10. CPWC results correspond to those of figure 6.4. As seen, both correlation coefficients of maximum and mean strains from CPWC imaging are higher than those obtained with focused imaging.

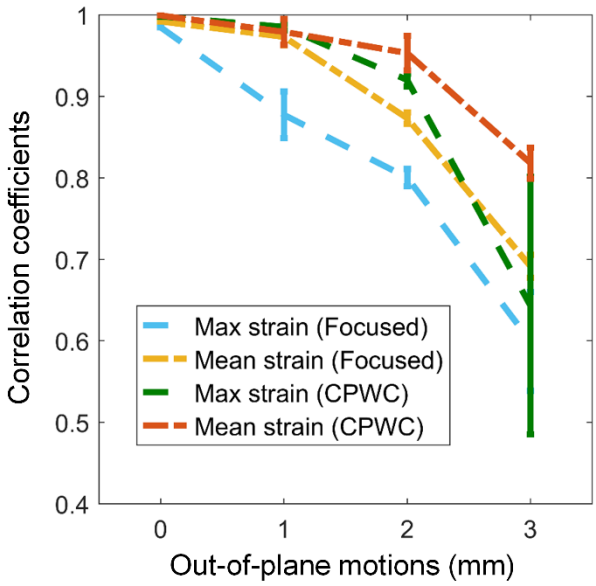

Figure 6.10 Correlation coefficients of time-varying maximum and mean strain curves regarding different out-of-plane motions in longitudinal view using the Verasonics scanner (L7-4 probe) with focused imaging and coherent plane wave compounding (CPWC) imaging for *in vitro* experiments considering out-of-plane motions of 0 mm, 1 mm, 2 mm and 3 mm. For maximum strain curves using focused imaging, correlation coefficients are 0.985, 0.877 ± 0.029, 0.800 ± 0.011 and 0.599 ± 0.061, respectively. For mean strain curves using focused imaging, correlation coefficients are 0.992, 0.973 ± 0.010, 0.873 ± 0.007 and 0.691 ± 0.014, respectively. For maximum and mean strain curves using CPWC imaging, correlation coefficients have been reported in figure 6.4.

6.6 Discussion

Out-of-plane motion is unavoidable when performing 2-D strain imaging due to vessel 3-D displacements. Since a 1D linear array probe only provides a 2-D scan plane, it is difficult to characterize motion information in elevation (*i.e.*, outside the imaging plane). To evaluate the impact of such out-of-plane motion on strain and shear estimates with *in vitro* and clinical data, we investigated it systematically using two beamforming schemes (plane wave and focused imaging) with two linear array probes (L7-4 and L14-5/38). For *in vitro* studies, we designed an experimental setup with known motion magnitude and frequency. *In vitro* results showed that the performance of axial strain estimations is indeed decreased with increasing out-of-plane motions. Similar results were obtained in Appendix for axial shears. Axial strain estimations

with the LSME were nevertheless robust and reproducible when out-of-plane motions was ≤ 2 mm either in longitudinal or cross-sectional imaging view. For the axial shear component, mean correlation coefficients of maximum and mean shear magnitudes were above 0.87 for motions ≤ 2 mm in both longitudinal and cross-sectional imaging views.

To our knowledge, there is no study reporting clinical out-of-plane motion magnitudes because of the lack of clinical trials on carotid elastography in 3D. However, as we did in this report, out-of-plane motions can be deduced. Cinthio *et al*. [188] confirmed that the longitudinal movement of human healthy carotid artery walls had the same magnitude as the radial motion in longitudinal view, which was less than 1 mm. Recent studies showed that the longitudinal motion magnitude of carotid atherosclerotic plaques can reach 1 mm [70, 192, 194, 199]. In the current study, we measured the maximum cumulated lateral motion of human carotid atherosclerotic plaques at 1.04 mm (mean of 0.63 ± 0.22 mm) in cross-sectional imaging view, which coincides with previous studies mentioned above. As shown *in vitro*, the performance of the LSME for axial strain and shear estimations was robust when the out-of-plane motion was 1 mm (correlation coefficients higher than 0.96), which implies that the LSME likely provides reliable axial strain and shear estimations clinically.

For *in vitro* experiments, axial strain and shear estimations only had small variations between 1 mm out-of-plane motion and no motion. The elevational resolution of a linear array probe accounts for these results. It is defined by the elevational F-number = $z_f / b_h \times \lambda$, where z_f is the focal depth, b_h is the element height and λ is the transmitted pulse wavelength. For the L7-4 probe, the elevational F-number = $25/7\lambda$ = 1.1 mm. The slice thickness inhibits resolving tissue structure within that range, thus reducing the impact of out-of-plane motion within the resolution cell. This explanation also applies to the clinical study, for which the elevational F-number is about 0.86 mm for the L14-5/38 probe.

From *in vivo* results in figure 6.7, the lowest NCC values were noticed at dilation and compression peaks of strain curves, which means the images were not compensated well using 2-D motions. That is because of larger out-of-plane motion occurrence at dilation and compression peaks of in-plane motions. The potential explanation is that out-of-plane motions are synchronized with in-plane motions due to 3-D vascular motions, which helps to identify

the part of a cardiac cycle in which 2-D strain estimations are more affected by out-of-plane motions.

To properly compare reported *in vitro* and clinical results, one would need to consider the inter-frame out-of-plane motion that differed between studies. Indeed, a smaller out-of-plane motion between consecutive frames should lead to larger overlap in elevation when a 2-D scan is performed, resulting in less speckle decorrelation. In the current study, although coherent plane wave compounding beamforming (frame rate of 400 s^{-1}, Verasonics scanner) and line-by-line focused imaging (frame rate between 18-25 s^{-1}, Ultrasonix scanner) were respectively used *in vitro* and in the clinical study, the mean inter-frame out-of-plane motions were smaller than 90 μm. Indeed, at 400 Hz, the inter-frame out-of-plane motions of 1 mm, 2 mm and 3 mm were 6 μm, 12 μm and 18 μm, respectively. In the clinical study at 18-25 Hz, mean inter-frame out-of-plane motions were 28 μm, 64 μm and 90 μm for the three groups depicting different ranges of motion in elevation, respectively. Previous studies showed that when inter-frame out-of-plane motion remains small (less than 100 μm), strain estimations obtained with 2-D and 3-D cross-correlation-based estimators are similar [23, 24].

As it could be seen in figure 6.10 with *in vitro* experiments, correlation coefficients for CPWC imaging were higher than those obtained with focused imaging when using the same ultrasound scanner (Verasonics) and transducer (L7-4). Differences in inter-frame out-of-plane motions at frame rates of 400 s^{-1} (CPWC) versus 25 s^{-1} (focused imaging) likely accounted for this. For CPWC imaging, as mentioned above, the inter-frame out-of-plane motions for 1 mm, 2 mm and 3 mm displacements were 6 μm, 12 μm and 18 μm, respectively. For focused imaging, inter-frame out-of-plane motions for 1, 2, and 3 mm probe oscillation were 40 μm, 80 μm and 120 μm, respectively. Again, larger transverse motions resulted in more decorrelation artifacts.

Another potential factor that could cause correlation coefficient differences between *in vitro* experiments and the clinical study is the more complex human tissue structure of carotid plaques than the designed phantom. To verify that, we refer to figure 6.9 for the 1 mm out-of-plane motion that is within the range of the largest *in vivo* clinical out-of-plane motions (0.78 - 1.05 mm) of figure 6.8. As seen, correlation coefficients of 0.955 ± 0.036 for the *in vitro* study (at 1 mm out-of-plane motion) are higher than those of the group of patients with largest out-of-

plane motions (0.744 ± 0.044). This suggests that indeed the complexity of the plaque structure contributes to decorrelation artifacts.

In this study, we deduced clinical out-of-plane motions of longitudinal image sequences by using 2-D cross-sectional image sequences. In the future, more accurate estimations of clinical carotid artery out-of-plane motions may be derived with 3-D data using a 2-D transducer array. Moreover, the 2-D LSME may be extended to 3-D to improve strain estimations, as theoretically derived in [107].

6.7 Conclusion

In this study, the influence of out-of-plane motions on the performance of the LSME was quantified *in vitro* and evaluated clinically with atherosclerotic carotid artery plaques. The experimental framework presented in this study is of interest as it could also allow studying the impact of out-of-plane motions on other strain estimation algorithms and beamforming strategies. For *in vitro* experiments, we found higher strain and shear estimation artifacts with increasing magnitudes of out-of-plane motion (lower correlation coefficients with higher out-of-plane motions). However, even with 2.0 mm out-of-plane motion, robust axial strain and shear estimations were still obtained. The clinical study verified *in vitro* results and showed that axial strain and shear estimations with small, moderate and large out-of-plane motions were quite reproducible. This knowledge should enable more confidence when analyzing clinical dataset for vulnerable carotid atherosclerotic plaque studies. Additionally, we found that the accuracy of strain estimations was decreased with increasing inter-frame out-of-plane motions, which suggests that CPWC imaging may strengthen clinical strain assessment of carotid arteries. In conclusion, the performance of the LSME for axial strain and shear estimations is robust in the presence of out-of-plane motion magnitudes corresponding to translations of carotid artery plaques observed clinically.

6.8 Acknowledgments

This work was supported by the Collaborative Health Research Program of the Natural Sciences and Engineering Research Council of Canada (CHRP-462240-2014) and the Canadian

Institutes of Health Research (CPG-134748). Clinical ultrasound data were acquired through the support of the Canadian Institutes of Health Research (PPP-78763).

6.9 Appendix

6.9.1 Optical flow based Lagrangian speckle model estimator

Other than axial strain, the LSME is also able to provide estimations of lateral strain, and axial and lateral shears. Specifically, an affine transformation model is applied into the optical flow equation. Within a small MW with $p \times q$ pixels, an over-determined linear equation system is solved to obtain all 2-D strain components.

$$\begin{bmatrix} I_{x_1}x_1 & I_{x_1}z_1 & I_{x_1} & I_{z_1}x_1 & I_{z_1}z_1 & I_{z_1} \\ \vdots & \vdots & \vdots & \vdots & \vdots & \vdots \\ I_{x_{p\times q}}x_{p\times q} & I_{x_{p\times q}}z_{p\times q} & I_{x_{p\times q}} & I_{z_{p\times q}}x_{p\times q} & I_{z_{p\times q}}z_{p\times q} & I_{z_{p\times q}} \end{bmatrix} \begin{bmatrix} s_{xx} \\ s_{xz} \\ U_x \\ s_{zx} \\ s_{zz} \\ U_z \end{bmatrix} = -\begin{bmatrix} I_{t_1} \\ \vdots \\ I_{t_{p\times q}} \end{bmatrix}, \quad (5.7)$$

where I_x, I_z are the spatial gradient of the image intensity, I_t denotes the temporal gradient of the image intensity, x, z are coordinates of pixels within the MW, $s_{xx}, s_{xz}, U_x, s_{zx}, s_{zz}, U_z$ are lateral strain, lateral shear, lateral displacement, axial shear, axial strain, and axial displacement, respectively. Here, axial strain is defined as the change in length in axial direction divided by the initial length in axial direction. Correspondingly, axial shear is defined as the change in length in axial direction divided by the initial length in lateral direction. In the current study, because of the limited lateral resolution of ultrasound imaging, lateral strain and shear components were not analyzed.

6.9.2 Decorrelation results for the axial shear component

Figure 6.11 shows correlation coefficients of maximum and mean axial shear curves for out-of-plane motions of 0 mm, 1 mm, 2 mm, and 3 mm for *in vitro* longitudinal view images. Figure 6.12 presents the same results in cross-sectional view. Finally, figure 6.13 shows correlation coefficients of mean axial shear curves for small, moderate and large out-of-plane motions for the clinical dataset. As done in previous studies [70, 192], the absolute shear

magnitude averaged within the segmented area was considered for maximum and mean time-varying curves.

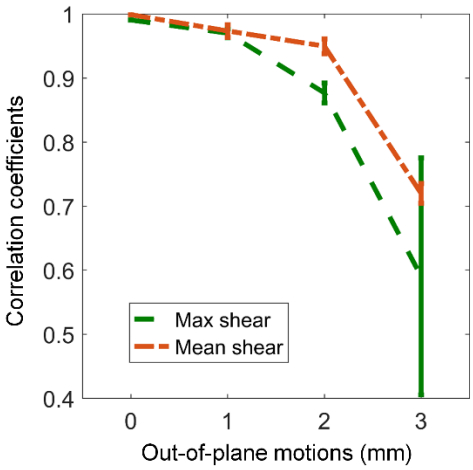

Figure 6.11 Correlation coefficients of maximum and mean axial shear curves regarding different out-of-plane motions in longitudinal view. For maximum shear curves, correlation coefficients are 0.991, 0.970 ± 0.007, 0.877 ± 0.016 and 0.590 ± 0.185 respectively for out-of-plane motions of 0 mm, 1 mm, 2 mm and 3 mm. For mean shear curves, correlation coefficients are 0.999, 0.973 ± 0.010, 0.950 ± 0.012 and 0.720 ± 0.016 respectively for out-of-plane motions of 0 mm, 1 mm, 2 mm and 3 mm.

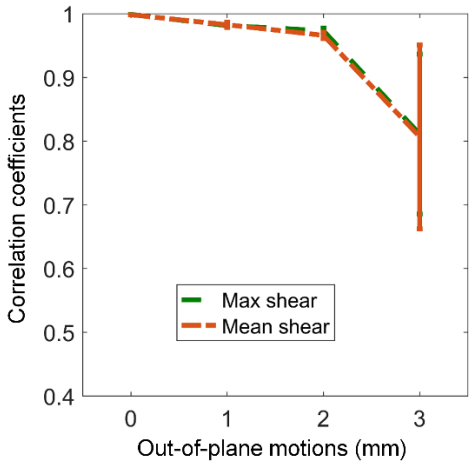

Figure 6.12 Correlation coefficients of maximum and mean axial shear curves regarding different out-of-plane motions in cross-sectional view. For maximum shear curves, correlation coefficients are 0.999, 0.981 ± 0.003, 0.973 ± 0.004 and 0.811 ± 0.126 respectively for out-of-plane motions of 0 mm, 1 mm, 2 mm and 3 mm. For mean shear curves, correlation coefficients are 0.998, 0.983 ± 0.004, 0.966 ± 0.005 and 0.807 ± 0.144 respectively for out-of-plane motions of 0 mm, 1 mm, 2 mm and 3 mm.

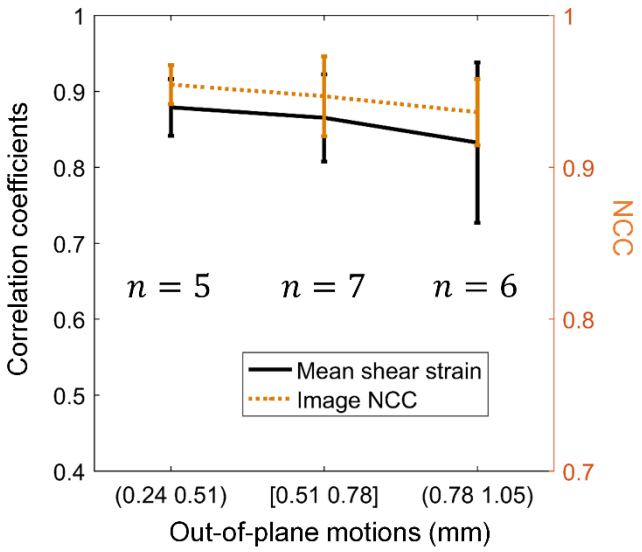

Figure 6.13 Correlation coefficients of mean axial shear curves for small, moderate and large out-of-plane motions of clinical images, which are 0.879 ± 0.037, 0.865 ± 0.058 and 0.832 ± 0.106, respectively, for these three groups of out-of-plane motions. Corresponding mean normalized cross-correlation (NCC) values are 0.954 ± 0.013, 0.947 ± 0.026 and 0.936 ± 0.022, respectively.

Chapter 7 : Parameterized strain estimation for vascular ultrasound elastography with a sparse model

7.1 Introduction to manuscript

This chapter reproduces the content of a submitted article 'Parameterized strain estimation for vascular ultrasound elastography with a sparse model' to the journal *IEEE Transactions on Medical Imaging* by Hongliang Li, Jonathan Porée, Boris Chayer, Marie-Hélène Roy Cardinal and Guy Cloutier for evaluation by a peer review committee.

The following is the order of authors for this submitted article and corresponding affiliations:

Hongliang Li[1,2], Jonathan Porée[1,2], Boris Chayer[1], Marie-Hélène Roy Cardinal[1] and Guy Cloutier[1,2,3]

[1] Laboratory of Biorheology and Medical Ultrasonics, University of Montreal Hospital Research Center (CRCHUM), Montréal, QC, Canada;

[2] Institute of Biomedical Engineering, University of Montreal, Montréal, QC, Canada;

[3] Department of Radiology, Radio-Oncology and Nuclear Medicine, University of Montreal, Montréal, QC, Canada.

The contributions of all authors to the submitted article is detailed below:

Hongliang Li: Developed and implemented the strain estimation algorithm and analysis algorithms, designed and fabricated *in vitro* phantoms, conducted *in vitro* data acquisitions, performed the post-processing of the data and the analysis of results, and drafted the article.

Jonathan Porée: Developed the finite element model, performed *in vivo* data acquisitions, contributed to *in vitro* data acquisitions and algorithm development.

Boris Chayer: Contributed to the fabrication of soft phantoms with hard inclusions.

Marie-Hélène Roy Cardinal: Contributed to the interpretation of results and to the writing of the manuscript.

Guy Cloutier: Supervised this work as the research director. Contributed to the interpretation of results as the project director. Corrected and finalized the manuscript for submission.

7.2 Abstract

Ultrasound vascular strain imaging has shown its potential to interrogate the motion of the vessel wall induced by the cardiac pulsation for predicting plaque instability. There is a trade-off among window parameters, quality of a strain image, and computation efficiency for window-based strain estimator. Moreover, conventional correlation-based methods only derive displacement fields first. Consequently, additional spatial derivatives are required to obtain strain estimates. Such gradient operation enhances the variance of the strain estimation when high frequency displacement noise is encountered. In this study, a sparse model strain estimator (SMSE) is proposed to reconstruct a dense strain field at a high resolution, with no spatial derivatives, with a high computation efficiency. Specifically, a dense optical flow (OF) model with Discrete Cosine Transform (DCT) descriptions was parameterized to derive affine strain components (axial and lateral strains and shears). Moreover, the sparse framework was analytically implemented to reduce estimation time. With simulations, the SMSE reduced estimation errors by up to 50% compared with the state-of-the-art window-based Lagrangian speckle model estimator (LSME). The SMSE was also proven to be more robust than the LSME against global and local noise. For in vitro and in vivo tests, residual strains assessing cumulated errors with the SMSE were 2 to 3 times lower than with the LSME. Regarding computation efficiency, the processing time of the SMSE was reduced by 4 to 25 times compared with the LSME, according to simulations, in vitro and in vivo results. Finally, phantom studies demonstrated the enhanced spatial resolution of the proposed SMSE algorithm against LSME.

7.3 Introduction

Vascular ultrasound strain imaging has shown its potential to extract the motion of the vessel wall caused by the cardiac pulsation for the purpose of trying predicting carotid artery plaque instability [200]. Currently, window-based methods are widely used to estimate two-dimensional (2-D) strain maps from radiofrequency (RF) datasets, using either image amplitude [14, 18, 21, 107, 127] or phase information [17, 25, 108, 109]. Specifically, pre-and post-motion

images are divided into overlapping windows. Assuming that motions of pixels within a window are uniform, window-based methods locally derive mean displacements and/or strains within that window. However, there is a trade-off among window parameters, quality of a strain image and computation efficiency. A small window size with a large overlap are desired for a better resolution as the cost of a high computational load. A large overlap nevertheless introduces worm artifact filtering [201, 202]. On the other hand, a small window size results in larger estimation variances.

An alternative way is to globally estimate pixel-wise motions in a region of interest (ROI) instead of using overlapping windows. To our knowledge, no pixel-based algorithms were proposed for vascular ultrasound elastography. Some approaches have been developed for quasi-static elastography [106, 111, 115-118], Doppler vector flow [203], myocardial motion tracking [204, 205] and computer vision [26]. Usually, ones formulate pixel-based motion estimations as an optimization problem where a cost function incorporating a data term and a regularization term is minimized. Sparse representations of motion fields were also introduced into motion estimators [206-208], where dense motions can be recovered using the compressed sensing theory [209] with a small portion of all samples. However, these models only consider displacement or velocity fields and do not estimate strain directly on a pixel base (*i.e.*, without spatial derivatives that are affecting variance). Affine model-based estimation could circumvent this limitation but remains into the category of window-based methods [16, 18, 25]. An optical-flow-based Lagrangian speckle model estimator (LSME) including an incompressibility constraint was proposed to obtain robust strain estimates in the context of vascular elastography [18]. A performance evaluation of the LSME and of an affine phase-based estimator (APBE) was also conducted showing the superiority of the LSME [25]. Although some of aforementioned pixel-based methods [106, 115] have considered axial or lateral strain estimations, shear strains are still not considered. To our knowledge, a pixel-wise vascular strain estimator with an affine model considering all strain components without spatial derivatives on displacements has not yet been proposed.

Computation efficiency is another issue that needs to be addressed. Computation time of window-based methods depends on the window size and on the level of overlap. Specifically, the computation time of a whole motion field corresponds to the sum of the time required to

locally perform successive window computations. To reduce the computation load, all pixels inside a ROI can be used to solve the dense motion field globally. However, this usually requires to optimize iteratively a cost function until convergence, which also impacts computation time. Rivaz's group proposed to convert the optimization problem into solving a sparse linear system of equations using a computationally efficient iterative algorithm [118]. However, the proposed method is still based on displacement estimates. Recently, an effort was made to change the iterative optimization into a least squares scheme to obtain analytic solutions of vector Doppler flow maps [27]. This strategy was adapted here for vascular strain imaging.

In this study, we propose to parameterize strain fields using a sparse model based on Discrete Cosine Transform (DCT) coefficients, which allows to directly derive strains without explicit gradient operation. This parameterized implementation also enables strains to be solved analytically using a least squares scheme. The proposed vascular sparse model-based strain estimator (SMSE) is providing high-resolution pixel-wise affine strain estimations with high accuracy and high computation efficiency compared with LSME implementation.

7.4 Algorithm description

The proposed algorithm is within the framework of the Horn-Schunck (HS) optical flow method. Unlike HS that only considers a smoothness constraint, a nearly incompressibility regularization term was also introduced into the cost function to improve lateral strain estimation. Moreover, motion fields were parameterized with a truncated Discrete Cosine Basis. This sparse representation was formulated to solve strain fields using a least squares method instead of an optimization problem, as in the HS algorithm. The pixel-based solution is providing axial, lateral and shear strain components simultaneously.

7.4.1 Cost function with smoothness and nearly incompressibility constraints

7.4.1.1 Data term

The cost function consists of data and regularization terms. The data term is from the optical flow constraint equation, which implies that the intensity between two consecutive images is not changing,

$$I_x U_x + I_y U_y + I_t = 0, \tag{7.1}$$

where I_x, I_y are the spatial gradient of the image intensity, I_t denotes the temporal gradient of the image intensity, and U_x, U_y are the unknown lateral and axial displacements. Since there are two unknown variables in (7.1), additional constraints need to be added to overcome the ill-posed problem.

7.4.1.2 Smoothness constraint

Horn and Schunck proposed a classical first-order optical flow smoothness constraint [26]. However, it does not take into account discontinuities in displacement fields and tends to over smooth them [27, 210]. Here, we used a second-order smoothness constraint that is tailored towards complex flow fields [211, 212]. The cost function with such a second-order smoothness constraint is defined as:

$$\min_{U_x,U_y}\left\{(I_x U_x + I_y U_y + I_t)^2 + \lambda_s\left(\left(\frac{\partial^2 U_x}{\partial x^2}\right)^2 + \left(\frac{\partial^2 U_x}{\partial y^2}\right)^2 + \left(\frac{\partial^2 U_x}{\partial x \partial y}\right)^2 + \left(\frac{\partial^2 U_x}{\partial y \partial x}\right)^2 + \left(\frac{\partial^2 U_y}{\partial x^2}\right)^2 + \left(\frac{\partial^2 U_y}{\partial y^2}\right)^2 + \left(\frac{\partial^2 U_y}{\partial x \partial y}\right)^2 + \left(\frac{\partial^2 U_y}{\partial y \partial x}\right)^2\right)\right\}, \tag{7.2}$$

where λ_s is a regularization parameter to control the influence of the smoothness constraint. The first half of (7.2) corresponds to (7.1). The second half represents displacement field smoothness constraints. To find suitable displacement fields minimizing (7.2), one can solve Euler-Lagrange equations, which is a typical variational problem. A detailed solution description can be found in [26]. In this study, displacement fields were parameterized with a truncated Discrete Cosine

Basis (see Section 7.4.2). The minimization problem was rewritten as a linear least squares problem.

7.4.1.3 Nearly incompressibility constraint

An incompressible material experiences no volume change under small deformations. Some biological tissues can be considered as nearly incompressible [211]; this is the case of human arteries [213]. In the field of ultrasound strain imaging, arterial tissue incompressibility was used to improve the quality of strain estimations [18, 25, 214]. Assuming 2-D plane strain, a null divergence of the displacement field $\vec{U}$ is considered, *i.e.* $div\ \vec{U} = \frac{\partial U_x}{\partial x} + \frac{\partial U_y}{\partial y} = 0$. Upon this assumption, the lateral strain is constrained to be the negative of the axial strain, as used in [18]. In the current study, we integrated instead this incompressibility constraint into (7.3) to obtain an additional regularization term to constrain the divergence close to zero:

$$\min_{U_x,U_y}\left\{(I_xU_x + I_yU_y + I_t)^2 + \lambda_s\left(\left(\frac{\partial^2 U_x}{\partial x^2}\right)^2 + \left(\frac{\partial^2 U_x}{\partial y^2}\right)^2 + \left(\frac{\partial^2 U_x}{\partial x\partial y}\right)^2 + \left(\frac{\partial^2 U_x}{\partial y\partial x}\right)^2 + \left(\frac{\partial^2 U_y}{\partial x^2}\right)^2 + \left(\frac{\partial^2 U_y}{\partial y^2}\right)^2 + \left(\frac{\partial^2 U_y}{\partial x\partial y}\right)^2 + \left(\frac{\partial^2 U_y}{\partial y\partial x}\right)^2\right) + \lambda_d\left(\frac{\partial U_x}{\partial x} + \frac{\partial U_y}{\partial y}\right)\right\}, \quad (7.3)$$

where λ_d is a regularization parameter to modulate the influence of the incompressibility constraint. Contrary to the implementation of [18], this regularization term does not impose tissue incompressibility, but constrains it into the cost function to obtain a nearly incompressible condition. This soft constraint avoids an ill-conditioned problem when forcing the divergence to zero. A similar quasi incompressibility constraint was utilized for the registration of magnetic resonance (MR) tissue images [211, 215], and for Doppler flow and tissue Doppler mapping [27, 216, 217]. It is used for the first time into the framework of an optical-flow based non-invasive vascular elastography method.

7.4.2 Sparse representation and reconstruction of the strain field

7.4.2.1 Discrete cosine representation

As mentioned earlier, the displacement field used in the minimization of (7.3) was expressed with type-II discrete cosine basis functions written as:

$$U_x(x,y) = \sum_m^{M_t} \sum_n^{N_t} c_{m,n}^x \cos(k_x^m(2x+1)) \cos(k_y^n(2y+1))$$
$$U_y(x,y) = \sum_m^{M_t} \sum_n^{N_t} c_{m,n}^y \cos(k_x^m(2x+1)) \cos(k_y^n(2y+1)), \quad (7.4)$$

where $k_x^m = \frac{m}{2M}\pi$, $k_y^n = \frac{n}{2N}\pi$, with the grid size (M, N) in lateral and axial directions, and (M_t, N_t) being the size of the truncated discrete cosine basis (*i.e.,* $M_t \leq M$, $N_t \leq N$). Section 7.5.5 justifies the choice of M_t and N_t. In (7.4), $c_{m,n}^x$ and $c_{m,n}^y$ are the DCT coefficients of the lateral and axial displacement components. In [206], it was verified that an optical flow vector is sparse in wavelet or DCT domains. Then, the problem to solving the optical flow vector in (7.3) was converted to sparse signal recovery from DCT coefficients. The advantage of optical flow sparsity enables to recover a dense flow field from much fewer pixels using the compressed sensing theory [207, 208]. In the next section, we propose a more efficient strategy to estimate sparse DCT coefficients from an over-complete pixel set using a least squares scheme.

Another advantage of parameterized representations of motion fields is that strain fields can be represented by DCT coefficients and DCT basis transformations, which avoids to explicitly compute derivative of noisy estimated displacements. Specifically, once DCT coefficients are resolved, strain components are represented by a combination of estimated DCT coefficients and DCT basis transformations, as shown here:

$$S_{xx} = \frac{\partial U_x}{\partial x} = \sum_m^{M_t} \sum_n^{N_t} c_{m,n}^x (-2k_x^m) \sin(k_x^m(2x+1)) \cos(k_y^n(2y+1))$$
$$S_{xy} = \frac{\partial U_x}{\partial y} = \sum_m^{M_t} \sum_n^{N_t} c_{m,n}^x (-2k_y^n) \cos(k_x^m(2x+1)) \sin(k_y^n(2y+1))$$
$$S_{yy} = \frac{\partial U_y}{\partial y} = \sum_m^{M_t} \sum_n^{N_t} c_{m,n}^y (-2k_y^n) \cos(k_x^m(2x+1)) \sin(k_y^n(2y+1))$$
$$S_{yx} = \frac{\partial U_y}{\partial x} = \sum_m^{M_t} \sum_n^{N_t} c_{m,n}^y (-2k_x^m) \sin(k_x^m(2x+1)) \cos(k_y^n(2y+1)), \quad (7.5)$$

where $S_{xx}, S_{xy}, S_{yy}, S_{yx}$ are lateral strain, lateral shear, axial strain and axial shear, respectively. Cartesian strain components were combined and represented as principal minor and major strain tensors, ε_{min}, ε_{max}, where

$$\varepsilon_{min,max} = \frac{S_{xx}+S_{yy}}{2} \pm \sqrt{\left(\frac{S_{xx}-S_{yy}}{2}\right)^2 + \left(\frac{S_{xy}+S_{yx}}{2}\right)^2}. \quad (7.6)$$

7.4.2.2 Regularized weighted least squares estimation

The proposed algorithm is capable of reconstructing dense displacement and strain fields at each pixel of an image of size $M \times N$. A strain field of a down-sampled image can also be computed with less computational complexity. Since the displacement field was parameterized with the discrete cosine basis, the cost function in (7.3) should be expressed in terms of DCT coefficients and the minimization problem formulated as a solution of a system of linear equations, as explained below.

Let $\mathbf{c} = \left[\mathbf{c_x}^T, \mathbf{c_y}^T\right]^T$ be a column vector with length of $2M_t \times N_t$, where $\mathbf{c_x} = \left[\cdots, c^x_{m,n}, \cdots\right]^T$ and $\mathbf{c_y} = \left[\cdots, c^y_{m,n}, \cdots\right]^T$ are the DCT coefficients of lateral and axial displacement fields, respectively. To parameterize the cost function in terms of $\mathbf{c}$, the data term, and smoothness and nearly incompressibility constraints, are represented in matrix form, respectively. Regarding the data term, let $\mathbf{U} = \left[\mathbf{U_x}^T, \mathbf{U_y}^T\right]^T$ represent the displacement field, where $\mathbf{U_x} = [\cdots, U_x, \cdots]^T$ and $\mathbf{U_y} = \left[\cdots, U_y, \cdots\right]^T$ are the column vectors of lateral and axial displacements with lengths $M \times N$, respectively. By defining $\mathbf{B}$ as a discrete cosine transform matrix with size $MN \times M_t N_t$, and $\{\mathbf{B}\}_{i,M_t n+m} = \cos(k_x^m(2x_i+1)\cos(k_y^n(2y_i+1)))$, the displacement fields can be expressed as $\mathbf{U_x} = \mathbf{B}\mathbf{c_x}$ and $\mathbf{U_y} = \mathbf{B}\mathbf{c_y}$. Let $\left\{\mathbf{I_{of,x}}\right\}_{i,i} = I_x(x_i, y_i)$, $\left\{\mathbf{I_{of,y}}\right\}_{i,i} = I_y(x_i, y_i)$, and $\left\{\mathbf{I_{of,t}}\right\}_{i,i} = -I_t(x_i, y_i)$ be diagonal matrixes containing image gradients, where the subscript *of* stands for optical flow. The data term of the cost function can then be written as:

$$\mathbf{D_{of}}\mathbf{B_{of}}\mathbf{c} + \mathbf{I_{of,t}}, \tag{7.7}$$

where $\mathbf{D_{of}} = [\mathbf{I_{of,x}} \quad \mathbf{I_{of,y}}]$ with size $MN \times 2MN$, and $\mathbf{B_{of}} = \begin{bmatrix}\mathbf{B} & 0 \\ 0 & \mathbf{B}\end{bmatrix}$.

The cost function of (7.3) introduced a nearly incompressibility constraint to govern a 2-D divergence-free displacement field. Since the displacement field $\mathbf{U}$ is expressed on a DCT basis, $\mathbf{B}$ and DCT coefficients $\mathbf{c}$, as shown in (7.4), allow to represent the divergence with a combination of transformations on $\mathbf{B}$ and $\mathbf{c}$. Let $\mathbf{B^x} = \dot{D}_x\mathbf{B}$ and $\mathbf{B^y} = \dot{D}_y\mathbf{B}$ be first-order

derivatives of **B** in lateral and axial directions, respectively, where $\dot{D}$ stands for the first-order derivative operator. Thus, the divergence of the displacement field is presented in terms of **c** as:

$$\mathbf{B_d c}, \tag{7.8}$$

where $\mathbf{B_d} = [\mathbf{B^x} \quad \mathbf{B^y}]$. Likewise, the two-order smoothness constraint of (7.2) can also be written as a linear combination of two-derivative **B** and **c** terms, as shown below:

$$\mathbf{B_s c}, \tag{7.9}$$

where $\mathbf{B_s} = [\mathbf{B}^* \quad \mathbf{B}^*]$, and $\mathbf{B}^* = \ddot{D}_{xx}\mathbf{B} + \ddot{D}_{yy}\mathbf{B} + \ddot{D}_{xy}\mathbf{B} + \ddot{D}_{yx}\mathbf{B}$. Here, $\ddot{D}$ stands for the two-order derivative operator applied on pixel coordinates.

Finally, putting (7.7), (7.8) and (7.9) together into the cost function of (7.3), the minimization problem is reformulated into a linear system as

$$\mathbf{Ac} = \mathbf{b}, \tag{7.10}$$

where $\mathbf{A} = \left(\mathbf{D_{of}B_{of}}\right)^T\left(\mathbf{D_{of}B_{of}}\right) + \lambda_d\mathbf{B_d^T B_d} + \lambda_s\mathbf{B_s^T B_s}$, and $\mathbf{b} = \left(\mathbf{D_{of}B_{of}}\right)^T\mathbf{I_{of,t}}$. **A** is a sparse matrix with size $2M_tN_t \times 2M_tN_t$ and **b** is a column vector with size $2M_tN_t \times 1$. Above least squares estimation on a motion field is usually sensitive to outliers, which are associated with violation of the optical flow constraint given by (7.1). To avoid it, a weighted least squares was performed to assign low weights to outliers after the first least squares estimation. The weights were expressed as $\boldsymbol{w} = \frac{\mathbf{1}}{\mathbf{1}+\boldsymbol{R}}$, where $\boldsymbol{R} = |I_xU_x + I_yU_y + I_t|$ is the absolute value of residuals of the optical flow equation to evaluate the estimation bias of each sample. Applying weights on each sample, the final estimation of DCT coefficients $\hat{\mathbf{c}}$ was solved as:

$$\hat{\mathbf{c}} = \left(\widehat{\mathbf{A}}^T\widehat{\mathbf{A}}\right)^{-1}\widehat{\mathbf{A}}^T\mathbf{b}, \tag{7.11}$$

where $\widehat{\mathbf{A}} = \left(\mathbf{D_{of}B_{of}}\right)^T\mathbf{W}\left(\mathbf{D_{of}B_{of}}\right) + \lambda_d\mathbf{B_d^T B_d} + \lambda_s\mathbf{B_s^T B_s}$ and **W** is a weight matrix with size $MN \times MN$, whose column elements are $\boldsymbol{w}$.

7.4.3 Algorithm implementation

The proposed algorithm consisted of 7 steps:

- Step 1: Segment manually the vascular wall on a middle frame of an RF image sequence to generate a ROI. The ROI on remaining frames was propagated using an automatic segmentation algorithm [193] that allowed tracking translation motion and small changes in ROI boundary at given frames.

- Step 2: Normalize the RF image sequence with the maximum value of image intensities.

- Step 3: Select pixels inside masks generated in Step 1 to do calculation.

- Step 4: Build vectors and matrixes in (7.10) using (7.7), (7.8), and (7.9), and solve the least squares system of (7.10) to obtain DCT coefficients $\mathbf{c}$.

- Step 5: Introduce DCT coefficients $\mathbf{c}$ into (7.4) to compute displacement fields.

- Step 6: With computed weights $\mathbf{W}$, solve DCT coefficients $\hat{\mathbf{c}}$ using (7.11).

- Step 7: Introduce DCT coefficients $\hat{\mathbf{c}}$ into (7.5) to compute principal strain components using (7.6).

7.5 Simulations and experiments

7.5.1 Simulations

A carotid artery model was created using COMSOL Multiphysics (Structural Mechanics Module, version 3.5, COMSOL, France) whose geometry was described in [157]. A soft necrotic core (elasticity modulus $E = 10$ kPa) and four calcified inclusions ($E = 5000$ kPa) were embedded in a medium ($E = 600$ kPa) mimicking a fibrous plaque. All plaque components were considered nearly incompressible (Poisson'ratio $= 0.4995$). The density of randomly distributed scatterers included in the vascular model was 100 per resolution cell to ensure fully developed speckle [165].

A systemic blood pressure waveform with pressure changes from 80 to 120 mmHg (10 to 16 kPa) was applied to the simulated model. The pressure waveform was divided into 500 segments to allow mimicking a frame rate of $500\ \mathrm{s}^{-1}$. For each intraluminal pressure difference, displacements and strains of the vessel wall were calculated using a finite elements method

(FEM) under plane strain condition. These displacements plus pre-deformation positions were used to update the post-deformation positions of scatterers. The strains were used as gold standard for comparison.

Cross-sectional RF data were simulated using the ultrasound simulation program Field II [164]. A L14-5/38 linear array probe with 128 elements (Ultrasonix Medical Corporation, Richmond, BC, Canada) was simulated with a 7.2 MHz center frequency and a 40 MHz sampling rate. The full aperture was considered as activated in transmission to create plane waves with emission angles ranging from -10° to 10° with 1° increment. Plane wave data with 21 angles at each intraluminal pressure difference were beamformed to create one coherent plane wave compounded (CPWC) image using a delay-and-sum algorithm [78]. All beamformed images were corrupted with white Gaussian noise to make them more realistic with signal-to-noise ratios (SNR) of 20 dB, 15 dB and 10 dB. To evaluate the robustness of strain estimation algorithms against localized noise, the 20 dB SNR images were corrupted with additional white Gaussian noise at four specific regions where SNR was reduced to 5 dB.

7.5.2 *In vitro* experiments

In vitro data from two vascular phantoms, one homogeneous and the other heterogeneous, were used to validate the proposed SMSE algorithm. These phantoms were made of 10% polyvinyl alcohol mixed with 3% acoustic scatterers (Sigmacell cellulose, type 50, Sigma Chemical, St Louis, MO, USA). The homogeneous phantom was solidified using 6 freeze-thaw-cycles to obtain a modulus of 182 ± 21 kPa [166]. The heterogeneous phantom consisted in a soft inclusion within a vascular wall mimicking a lipid plaque. This soft inclusion was obtained with 1 freeze-thaw-cycle giving a modulus of 25 ± 3 kPa [166]; the surrounding vascular wall was similar to the homogeneous phantom.

Each phantom was suspended in a water tank and pressurized by connecting the tube outlet to a water column. The intraluminal pressure was varied from 60 mmHg to 120 mmHg with a pulsatile pump (model 1421, Harvard Apparatus, Holliston, MA, USA). The pressure was monitored using a ViVitest software system (Vivitro Labs Inc., Victoria, BC, Canada).

7.5.3 *In vivo* experiments

To further validate the proposed strain estimator, RF data of a common carotid artery were acquired from a 30 year-old healthy male. The study was approved by the human ethical review board of the Centre Hospitalier de l'Université de Montréal. The volunteer signed an informed consent.

7.5.4 Data acquisition and image reconstruction

For *in vitro* and *in vivo* experiments, RF data in a cross-sectional view were acquired using a Sonix Touch ultrasonic system (Ultrasonix Medical Corporation, Richmond, BC, Canada) equipped with a L14-5/38 linear array probe with 128 elements, as considered in the simulation study. Plane wave data were generated and stored with full aperture using a Sonix DAQ multi-channel system and the development kit software (TexoSDK, v6.0.1). As for simulations, CPWC images were beamformed in post-processing using a delay-and-sum algorithm [78] and emission angles ranging from -10° to 10° with 1° increment (final frame rate of $500\ \mathrm{s}^{-1}$). RF images were reconstructed on a regular Cartesian grid with 50×20 µm resolution (lateral × axial). All RF images were normalized in intensity before performing elastography computations.

7.5.5 Parameters selection

In (7.3), λ_s and λ_d govern the influence of smoothness and nearly incompressibility constraints. Different pairs of these two parameters were tested using simulation data with a SNR of 20 dB. The test ranges for λ_s and λ_d were both from 0.01 to 1 with an increment of 0.01. The smoothness and nearly incompressibility constraints were assumed to have the same influence on simulated, *in vitro* and *in vivo* strain estimates. Thus, the parameter pair providing the least estimation error was chosen for all reported results. The selected pair of parameters was $\lambda_s = 0.05$ and $\lambda_d = 0.6$.

For the sparse strain model of (7.3), sizes of the truncated discrete cosine basis M_t and N_t were chosen to reconstruct motion fields based on prior information. To our knowledge, there is no guideline on DCT numbers to reconstruct a motion field. We thus considered the following observations. The thickness of the carotid artery wall with a plaque was assumed smaller than 3

mm [218]. To limit higher spatial frequency variation of the motion field, the minimum wavelength of the cosine basis function was set to 1.5 mm. Thus, the number of DCT coefficients, M_t or N_t, was given by the Cartesian grid resolution (lateral or axial) $\times$ image size (lateral M or axial N) / 1.5 mm. The truncation allowed reducing the matrix size in (7.10) from $2MN$ to $2M_tN_t$, which impacted positively the computational complexity compared with a reconstruction with all DCT coefficients.

7.5.6 Criteria for evaluation

7.5.6.1 Comparison with the Lagrangian Speckle Model Estimator (LSME)

The LSME estimator of [18] was applied to simulation, *in vitro* and *in vivo* data to compare with the proposed sparse algorithm. For a fair comparison, the estimation parameters were the same as in [25]. Namely, the window size was set to 1.0 mm × 1.0 mm with 80% overlap in axial and lateral directions, and the time-ensemble number was 8 with 90% time overlap.

7.5.6.2 Evaluation of strain estimation performance

For simulated data, an image sequence of one pressure cycle was selected and all 2-D strain components (S_{xx}, S_{xy}, S_{yy}, S_{yx}) were computed over consecutive frames and cumulated. Principal strains were determined using (7.6) and the largest cumulated strain map was considered as the final elastogram. Since reference strain values are known for simulations, the normalized root-mean-square-error (NRMSE) was used to evaluate elastograms in that case:

$$NRMSE = \frac{\sqrt{\frac{\sum_{i=1}^{N}(ref_i - est_i)^2}{N}}}{ref_{max} - ref_{min}}, \tag{7.12}$$

where N is the number of pixels in an elastogram, ref is the ground truth principal strain from the finite elements analysis, and est is the estimated principal strains. The subscripts *max* and *min* refer to the maximum and minimum values of the principal strain map.

The metric for evaluation of cumulated strains in *in vitro* and *in vivo* studies was the residual strain. The rationale is that the carotid artery should restore its initial state after an entire cycle. The residual strain is a good indicator to evaluate cumulative estimation errors for

vascular elastography [23, 148]. The less residual strain means less cumulative estimation errors. In this study, a whole cycle was determined by two periodic zero-crossing points on the time-varying principal strain curve. The residual strain was calculated as the mean strain value of the cumulated end frame for a full cardiac cycle. In addition to the residual strain metric, the reproducibility of cumulative strain curves was evaluated for *in vivo* results. Two successive cardiac cycles of cumulated principal strain maps were estimated and spatially averaged to obtain mean principal strain curves. Unlike computing a correlation coefficient of two strain curves, as done in [219], we performed a linear regression of the two strain curves to fit a function, $y = ax + b$, where x, y are strain curves of two successive cycles, and a, b are fitted coefficients. Here, a was used to evaluate the similarity between the two consecutive strain curves and it was expected to be 1 when the two curves are the same. The intercept b was used to evaluate residual strain errors, and in this case it was expected to be 0 when there is no residual strain error.

7.5.6.3 Other assessments of strain estimation algorithms

Additionally, computation time for a whole image sequence was viewed as an indicator of algorithm efficiency. To assess this, the LSME and proposed SMSE algorithms were both implemented in Matlab 2016a (MathWorks Inc., Natick, MA, USA) on a 4-core CPU at 3.7 GHz.

Finally, additional *in vitro* measurements were performed to compare the strain image resolution of both LSME and SMSE algorithms. Two soft phantoms with hard inclusions were fabricated. The first one had three hard inclusions of 2 mm, 1 mm and 0.8 mm as the same depth. The other was made with three hard inclusions of 2 mm but at different depths. The soft background was made with 0.3% agar (A9799, Sigma–Aldrich Chemical, St Louis, MO), 4% gelatin (G2500, Sigma–Aldrich Chemical), 8% glycerol, and 87.7% distilled water. Hard inclusions were fabricated with 15% polyvinyl alcohol, 3% cellulose particles (Sigmacell, type 5504, Sigma Chemical), and 82% distilled water that underwent 6 freeze-thaw-cycles. Axial compressions with maximum deformations of 1 mm were launched on the top of the phantom with the ultrasound probe that was driven by a mini-shaker vibrating as a 1.2 Hz sinusoid. For the first phantom, the LSME with the same window size (1 mm × 1 mm) but different overlaps

of 50%, 80% and 95% were used to compare axial strains S_{yy} with those obtained with the proposed SMSE algorithm. For the second phantom, the LSME still had a window size of 1 mm × 1 mm with a 80% overlap.

7.6 Results

7.6.1 The simulation study

Figure 7.1(a) shows a B-mode image with a SNR of 20 dB of the carotid artery simulation using CPWC imaging. Principal strain maps estimated with the LSME and SMSE are presented in figure 7.1(d)-(g). For principal minor strains, both LSME and SMSE provided similar estimation performance with NRMSE of 8.45% and 6.75% with respect to the ground true, respectively. The LSME strain map (figure 7.1(d)) allowed identifying the small hard inclusion close to the lumen at 7 o'clock, but provided less evidence of the presence of the two hard inclusions in the upper right of the model than with the SMSE (figure 7.1(f)). The estimation error of principal minor strains was reduced by 20% with the SMSE compared with the LSME. For principal major strains, the SMSE strain map (figure 7.1(g)) revealed hard inclusions better than with the LSME (figure 7.1(e)). The NRMSE in figure 7.1(e) and (g) are 9.56% and 7.02%, respectively. The estimation error of principal minor strains was reduced by 27% using the SMSE. The impact of the LSME window size on strain estimates can be visualized in the zoomed ROI. The SMSE principal minor strain shows smoother inner and outer artery edges compared with the window-based LSME algorithm. A similar conclusion applies to the principal major strain map.

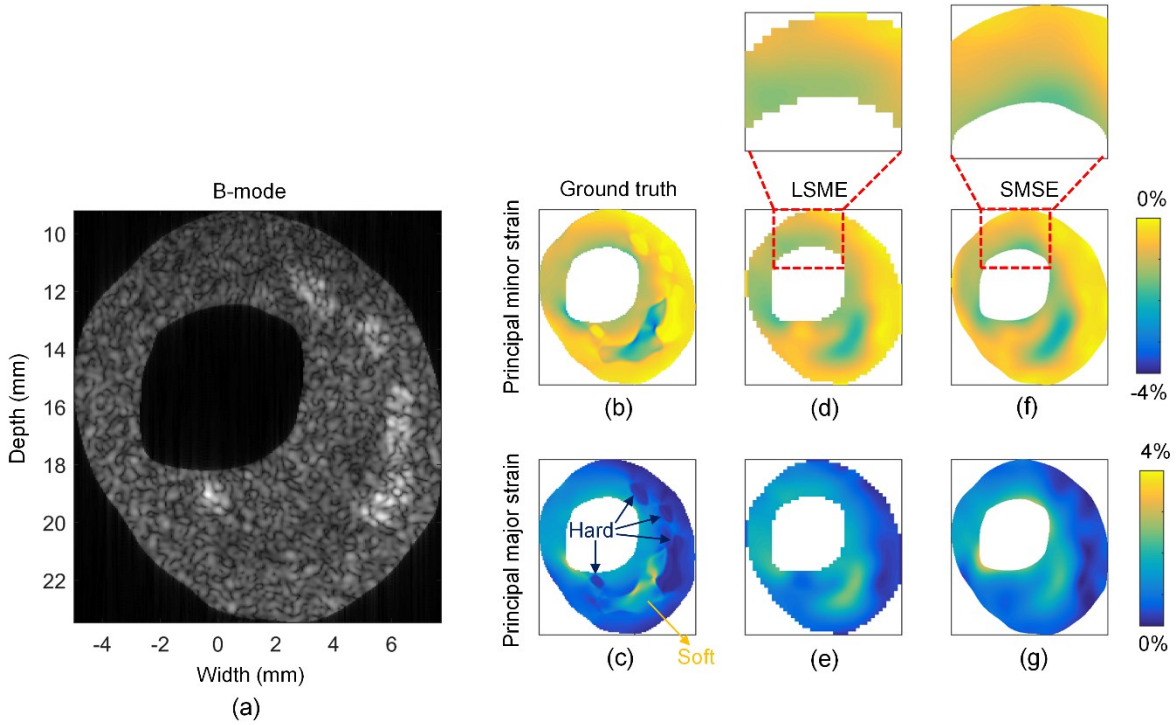

Figure 7.1 (a) B-mode image of an artery simulation model with one soft inclusion and four hard inclusions. The image SNR is 20 dB. (b), (c) Principal minor and major strains of the finite-elements model ground truth. (d), (e) Principal minor and major strains using LSME, whose NRMSE are 8.45% and 9.56%, respectively. (f), (g) Principal minor and major strains using SMSE, whose NRMSE are 6.75% and 7.02%, respectively. Close-ups in the red rectangular regions are displayed to present the resolution of strain maps.

To test robustness against noise, figure 7.2 presents simulations with SNRs of 10 dB and 15 dB. Principal strain maps with the LSME were noisier than with the SMSE when the SNR was reduced, especially in the thin wall region of the upper left part. NRMSE of LSME principal minor and major strain maps for the SNR of 10 dB are 13.90% and 16.27%, respectively, while those with the SMSE are 7.54% and 8.17%, respectively. Estimation errors of principal minor and major strains were reduced by 46% and 50%, respectively, using the SMSE. As shown in figure 7.2(d), at the SNR of 15 dB, the LSME estimation performance was improved with NRMSE of 9.81% and 11.33% for principal minor and major strain maps, whereas they remained similar but better with the SMSE (NRMSE of 7.30% and 7.49% for principal minor and major strain maps, respectively).

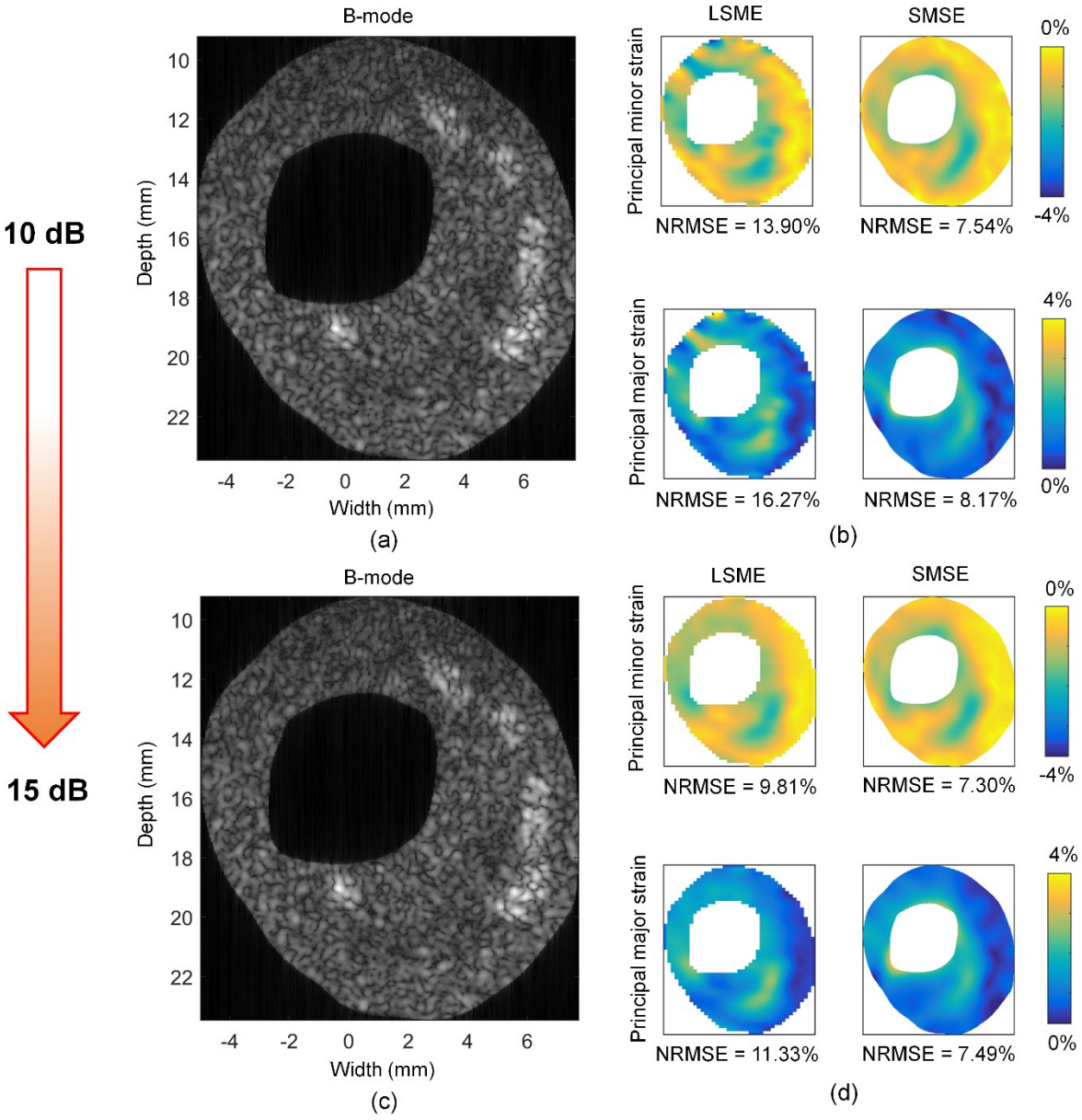

Figure 7.2 (a), (b) B-mode images with a SNR of 10 dB and corresponding principal strain maps. (c), (d) B-mode images with a SNR of 15 dB and corresponding principal strain maps. NRMSEs of principal strain maps with the LSME and SMSE are shown.

Figure 7.3 presents robustness of both algorithms against localized noise (simulations with a SNR of 20 dB where the SNR was reduced to 5 dB into the upper left (a), upper right (b), lower left (c) and lower right (d) regions). All LSME principal strain maps were obviously deteriorated by the addition of local noise. NRMSE of SMSE principal strain maps nearly

remained the same in all regions. Moreover, NRMSE with the SMSE were less than with the LSME (see legend of figure 7.3 for values).

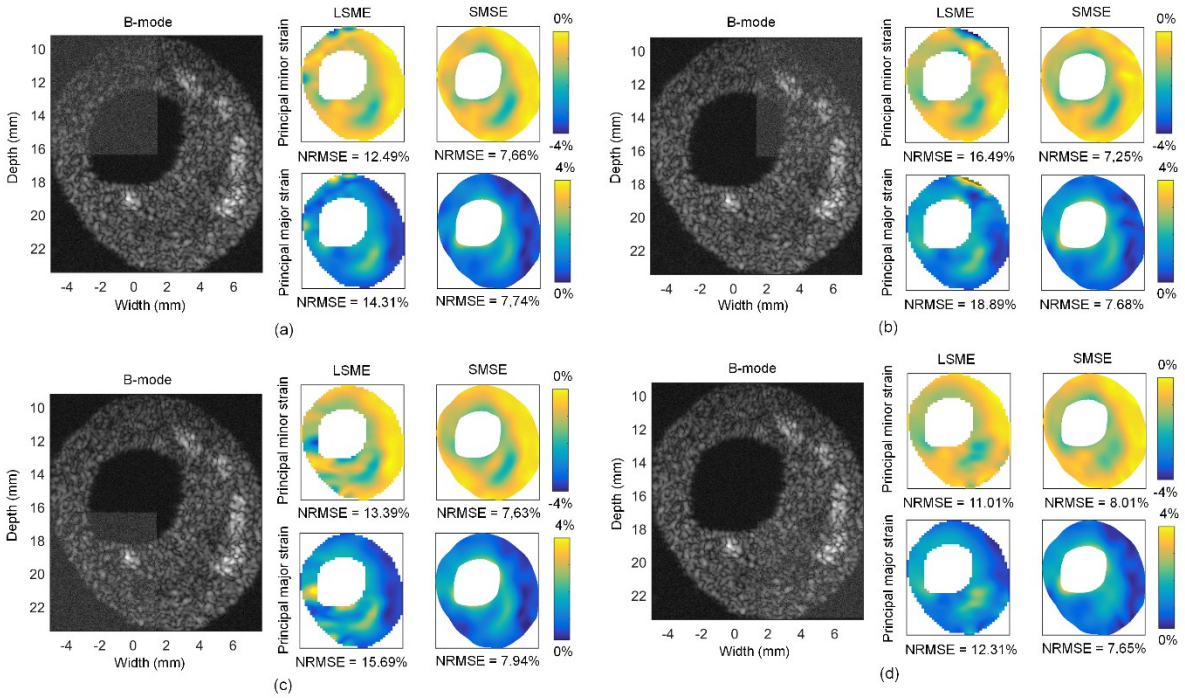

Figure 7.3 B-mode images with a global SNR of 20 dB and local noise at a SNR of 5 dB in the upper left (a), upper right (b), lower left (c) and lower right (d) regions and corresponding principal strain maps. NRMSEs of principal strain maps with the LSME and SMSE are shown.

7.6.2 *In vitro* experiments

7.6.2.1 The homogeneous vascular phantom study

Figure 7.4(a) presents a CPWC B-mode image of the homogeneous vascular phantom. Figure 7.4(b)-(e) shows principal strain maps using the LSME and SMSE. Like simulation results, the vascular geometry was more smoothly delineated in principal strains using the SMSE (panels (d) and (e)) than with the LSME (panels (b) and (c)). According to previous literature [168], the strain magnitude is expected to decrease with increasing radial distance from the lumen, which is known as the strain decay phenomenon. Qualitatively, the strain decay is more distinct on SMSE principal strain maps. Some artifacts are noticed on LSME elastograms at the lower left region (figure 7.4(b) and (c)). Residual principal minor and major strains at the

end of the flow cycle were -0.49% and 0.49% for the LSME, and they were reduced to -0.14% and 0.13% for the SMSE.

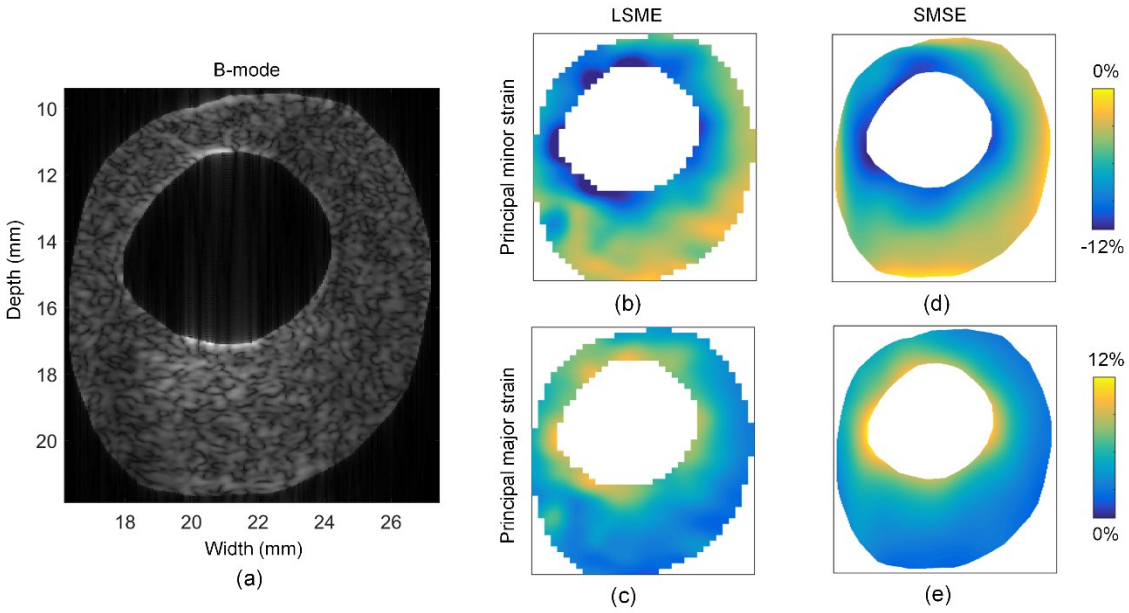

Figure 7.4 (a) B-mode image of a homogeneous vascular phantom. (b), (c) Principal minor and major strains using the LSME, whose residual strains are -0.49% and 0.49%, respectively. (d), (e) Principal minor and major strains using the SMSE, whose residual strains are -0.14% and 0.13%, respectively.

7.6.2.1 The heterogeneous phantom study

Figure 7.5 presents a CPWC B-mode image of the heterogeneous vascular phantom with a soft inclusion, and principal strains using the LSME and SMSE. The soft inclusion is identifiable on all strain maps. The strain decay phenomenon caused an overestimation of the dimension of the soft inclusion with both algorithms. Residual principal minor and major strains were -0.56% and 0.56% for the LSME, respectively. They were lower at -0.19% and 0.17% for the SMSE, respectively.

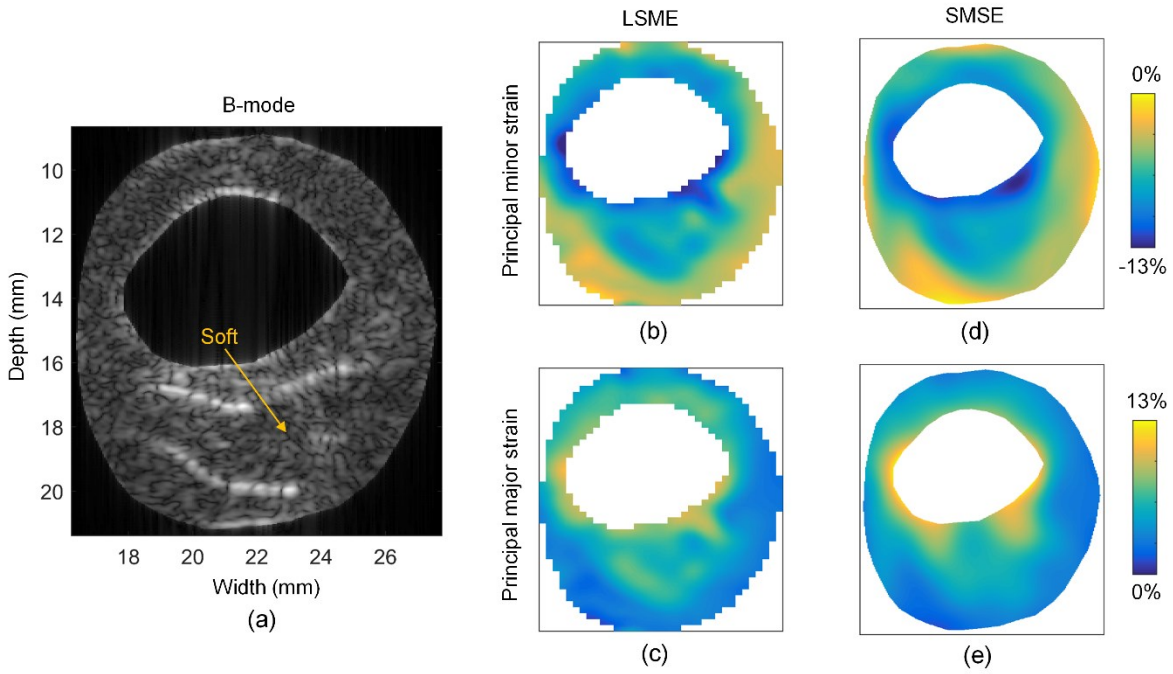

Figure 7.5 (a) B-mode image of a heterogeneous vascular phantom with a soft inclusion under the lumen. (b), (c) Principal minor and major strains using the LSME, whose residual strains are -0.56% and 0.56%, respectively. (d), (e) Principal minor and major strains using the SMSE, whose residual strains are -0.19% and 0.17%, respectively.

7.6.3 *In vivo* validation

Figure 7.6 displays an *in vivo* B-mode image of a common carotid artery. LSME and SMSE principal strain maps are shown in figure 7.6(b)-(e). Because of boundary conditions imposed by surrounding tissues, non-homogeneous strain maps were noticed with both algorithms as a function of the angular position. However, regional differences are observed when comparing both elastography methods. Residual strains at the end of the sequence for principal minor and major strain maps using the LSME were -5.56% and 5.56%, respectively, whereas they were below at -1.92% and 1.77% for the SMSE, respectively.

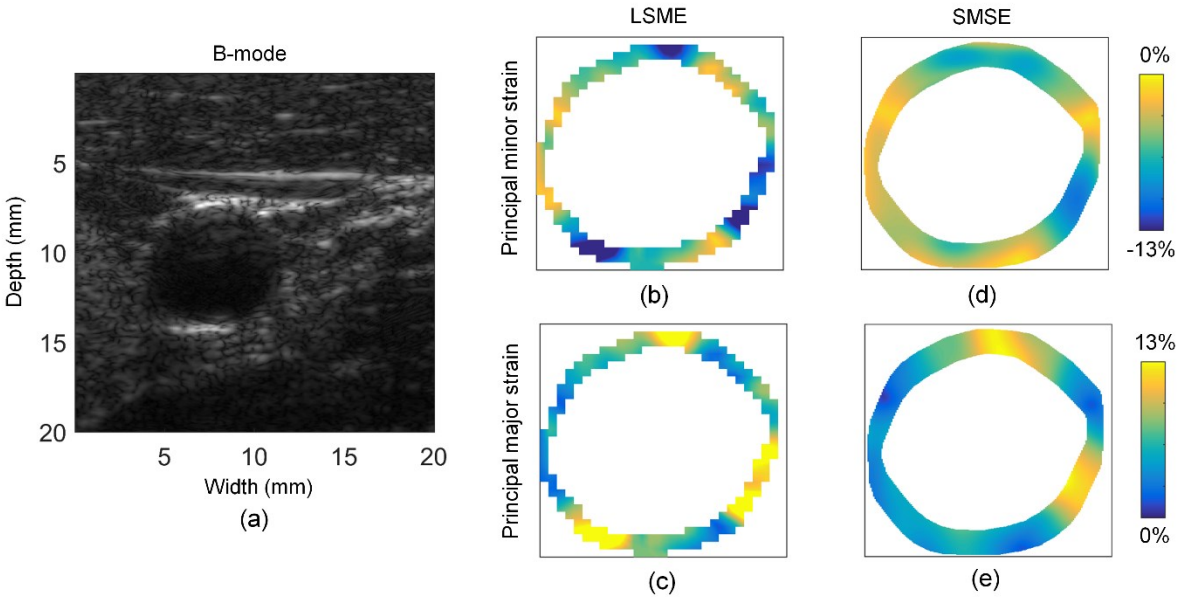

Figure 7.6 (a) *In vivo* B-mode image of a carotid artery of a 30 year-old healthy male. (b), (c) Principal minor and major strains using the LSME, whose residual strains are -5.56% and 5.56%, respectively. (d), (e) Principal minor and major strains using the SMSE, whose residual strains are -1.92% and 1.77%, respectively.

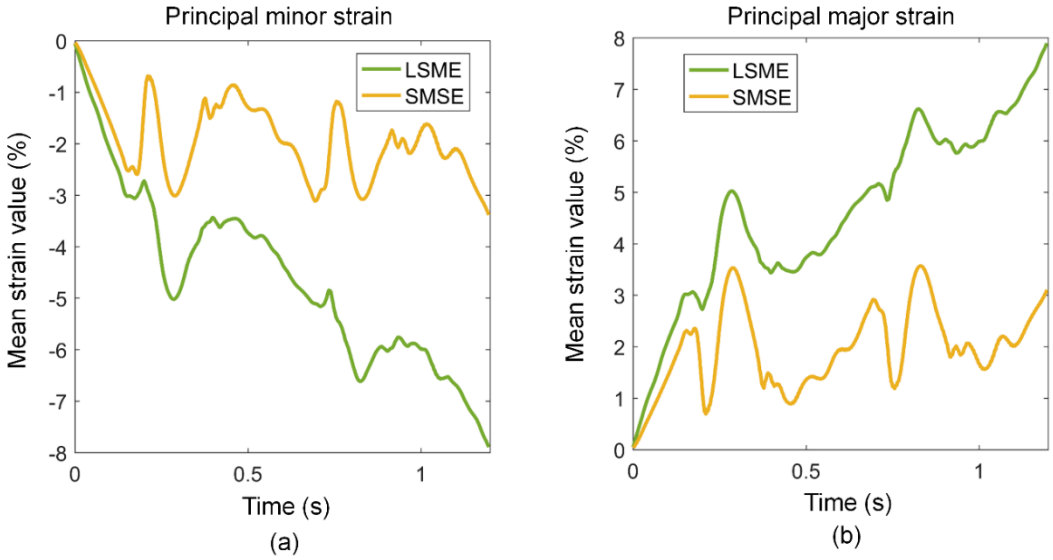

Figure 7.7 (a) Mean strain curve of cumulated principal minor strains for the LSME and SMSE over two cardiac cycles. (b) Mean strain curve of the cumulated principal major strain for the LSME and SMSE over two cardiac cycles.

Principal strain curves averaged over two cardiac cycles are presented in figure 7.7 for the LSME and SMSE. As quantified above, the SMSE gave less residual strain errors. To

quantify the reproducibility, strain curves of two cardiac cycles were used to perform a linear fit. As shown in figure 7.8, a higher regression coefficient a and a lower intercept b were obtained with the SMSE.

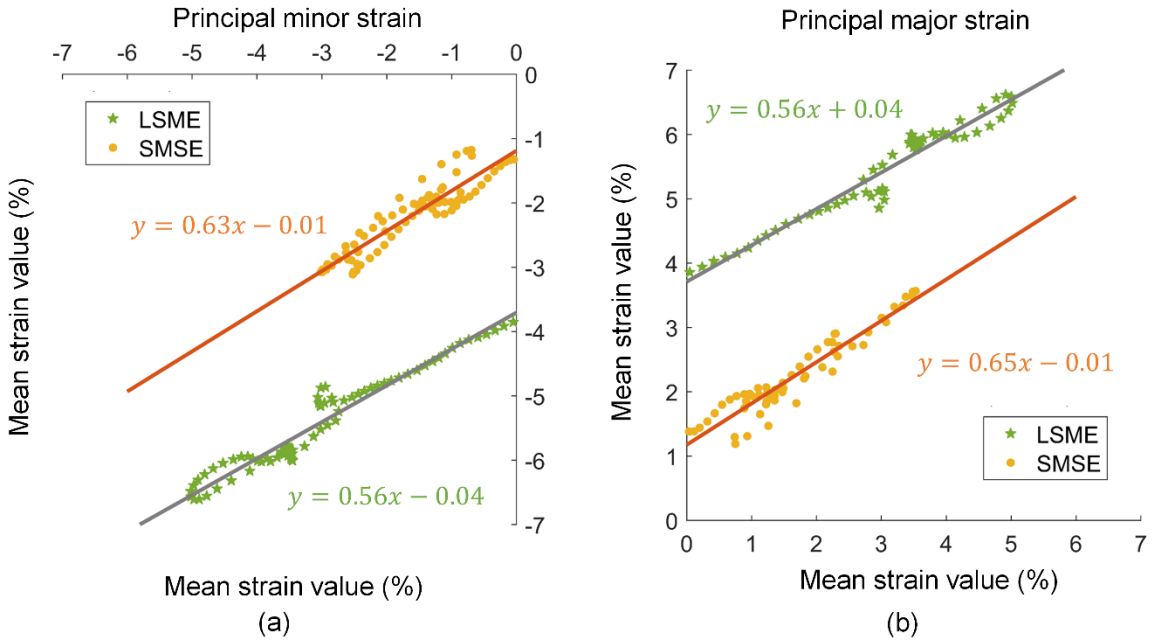

Figure 7.8 Two successive cardiac cycles of cumulative principal strain curves were selected from figure 7 to perform linear regressions for (a) principal minor strains of the LSME and SMSE, and (b) principal major strains of the LSME and SMSE.

7.6.4 Computation efficiency comparison

Computation time for processing a whole image sequence was calculated and normalized by the number of frames per sequence. As presented in Table 7-1, the computation time of the SMSE was reduced by 4 to 25 folds compared with the LSME regarding simulation, *in vitro* and *in vivo* data.

Table 7-1 Computation efficiency (second/frame).

Type of experiments	LSME	SMSE
Simulations	13.1	3.0
In vitro - homogeneous	9.2	1.7
In vitro - heterogeneous	9.6	2.1
In vivo	7.5	0.3

7.6.5 Spatial resolution

As seen in figure 7.9, the LSME elastogram with a 50% overlap (panel b) presents a smoother strain distribution than with higher overlaps, but fails to detect the inclusion of 0.8 mm. At 80% or 95% overlaps (panels c and d), the spatial sampling is improved but at the cost of a higher variance. The SMSE algorithm provided better results and allowed identifying all inclusion sizes. The impact of the hard inclusion depth is presented in figure 7.10 (for the 2 mm diameter inclusion). Again, the best results are obtained with the SMSE method.

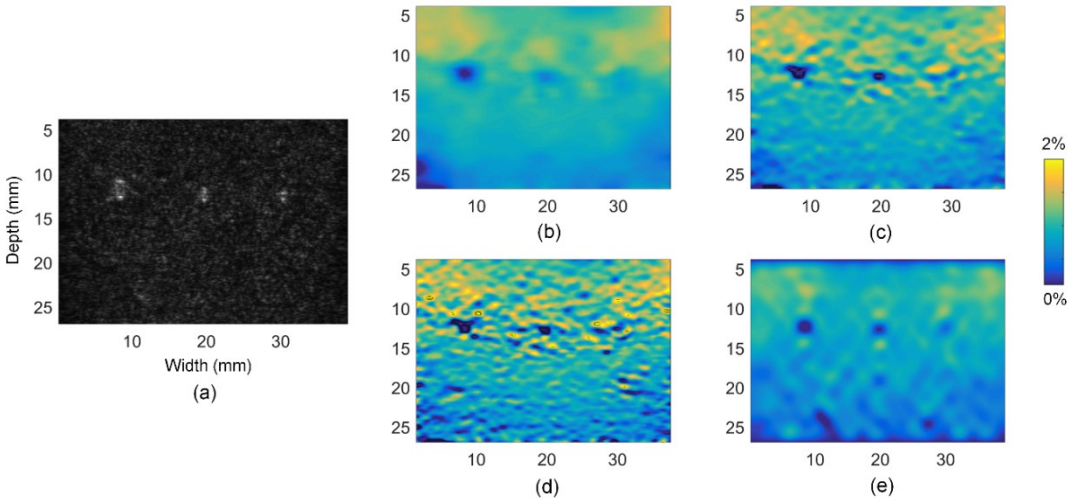

Figure 7.9 (a) B-mode image of a soft phantom with three sizes of hard inclusions of 2 mm, 1 mm and 0.8 mm. (b), (c), (d) axial strains using the LSME with a 1.0 mm × 1.0 mm window size and 50%, 80% and 95% overlaps, respectively. (e) axial strains using the SMSE.

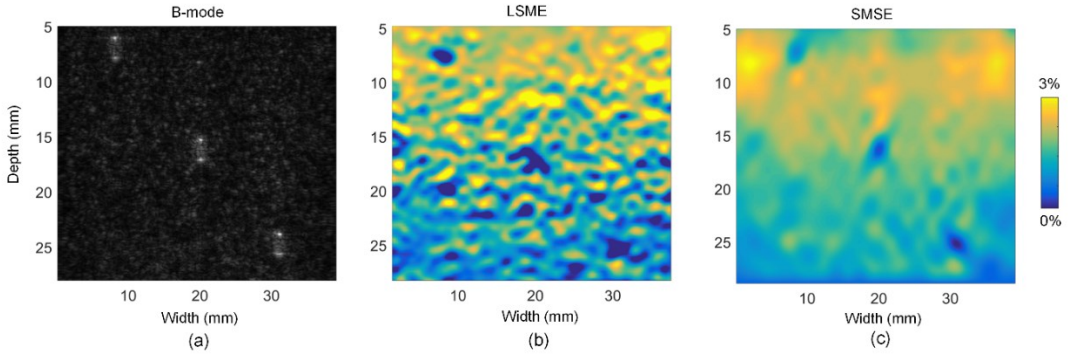

Figure 7.10 (a) B-mode image of a soft phantom with three hard inclusions of 2 mm at different depths. (b) axial strains using the LSME with a 1.0 mm × 1.0 mm window size and 80% overlap. (c) axial strains using the SMSE.

7.7 Discussion

Although dense OF estimation is already applied into computer vision [26] and myocardial motion tracking [205] to obtain displacement fields, these models required new developments for strain imaging in the context of vascular mechanical characterization. In the current study, we extended the dense OF model with DCT descriptions to derive four strain components (axial and lateral strains and shears). Those strain components were combined to obtain coordinate-system independent principal strains. Moreover, a sparse framework was analytically implemented to reduce estimation time compared with window-based strategies.

For *in vivo* results, principal strain maps were not homogeneous circumferentially (figure 7.6(b)-(e)). The same heterogeneous observation in strain maps for healthy carotid arteries were recently reported [15, 124]. The potential explanation is likely the presence of different boundary conditions surrounding the carotid artery [18]. Thus, we proposed to use a linear regression strategy to evaluate the reproducibility of cumulated principal strain curves instead of SNR measurements, as done in [15, 124].

There is a trade-off between elastogram spatial sampling and computation efficiency for window-based approaches. The spatial sampling is determined by the window overlap, as demonstrated in figure 7.9 for the case of the LSME algorithm. Compared with the 80% window overlap used to obtain most results, the computation time was reduced 4 times when using the 50% overlap, and it was increased 46 times for the 95% overlap. The proposed SMSE method could circumvent this trade-off issue by considering all pixels globally. Even with a theoretical pixel resolution, the SMSE computation time was still lower than that of the LSME with a lower resolution. Moreover, an arbitrary resolution can be set in this SMSE implementation, which could reduce the computation time proportionally. According to *in vivo* SMSE performance whose frame rate was around 3 s^{-1} with described computer facilities and software, it is believed that real-time estimation could be achieved by combining appropriate down-sampling estimation and parallel computing.

Another trade-off of window-based approaches is the compromise between elastogram spatial sampling and artifacts. Intuitively, larger overlap can increase elastogram spatial sampling, but at an expense of increasing artifacts. As seen in figure 7.9, the axial elastogram

using the LSME with a 50% overlap presented a smooth strain distribution, while it failed to detect the inclusion of 0.8 mm. With an overlap of 80% or 95%, the elastogram spatial sampling was increased and it was visually possible to barely see the 0.8 mm inclusion, but at the expense of strong background variance. Moreover, worm artifacts due to a large overlap were noticed. Worm artifacts appear as thin and short alternate bands attributed to correlation noise patterns when the overlap is increased [201]. The elastogram using the SMSE avoided these artifacts and presented clear outlines of each inclusions.

Theoretically, other sophisticated regularization terms that are used in dense optical flow techniques, such as sparsity of optical flow gradients [208] and non-local terms [220, 221] can be added into the proposed SMSE model as a prior knowledge instead of the nearly incompressibility term to solve the strain field. The impact of using different regularization terms on strain estimations deserves to be investigated in future studies.

The SMSE is not only able to provide robust strain estimates at a sub-mm spatial resolution, but also the assessment of the 2-D displacement field, as described by (7.4). Thus, the SMSE may be applicable in the context of shear wave elastography to track the 2-D velocity field [222]. Future experiments in that direction are worthy to be investigated. Beside ultrasound vascular elastography, it is believed that this sparse model can also be of value for magnetic resonance elastography [223] or non-rigid object tracking in computer vision applications [224]. As shown in Fig. 7.10(c), the detection of small hard inclusions at different depths might also enhance the capability of current quasi-static breast compression elastography technologies [225].

7.8 Conclusion

In this study, an affine model-based estimator including a sparsity strategy was proposed to provide vascular strain estimations at high spatial and temporal resolutions close to real-time. With simulation data, the SMSE gave less estimation errors than the window-based LSME approach. For *in vitro* results, elastograms with the SMSE showed less residual strain errors than with the LSME. For *in vivo* results, the SMSE provided also less residual strain errors and more reproducible cumulative strain curves. Computation time was reduced significantly with

the SMSE compared with the LSME. In addition, the SMSE avoided window effects of window-based approaches.

7.9 Acknowledgment

This work was funded by the Collaborative Health Research Program of the Natural Sciences and Engineering Research Council of Canada (CHRP-462240-2014) and the Canadian Institutes of Health Research (CPG-134748). Authors acknowledge the scholarship support of the Québec Bioimaging Network of the Fonds de Recherche Québec Santé to Mr. Li (Institute of Biomedical Engineering, University of Montréal).

Chapter 8 : Discussion and general conclusion

8.1 General summary

This thesis, including three articles, presented a series of accomplishments from experimental validations to algorithm development to improve NIVE for the characterization of carotid plaques.

The first article of this thesis (Chapter 5) exploited TO beamforming and two window-based affine strain estimators, the developed APBE and the LSME. The most important conclusion that we found is that combining the LSME with TO beamforming allowed obtaining comparable strain estimates than the LSME without TO beamforming according to simulations (figure 5.2) and better performance in the case of complex and heterogeneous phantoms over a wide range of applied strains from 0.07% to 3.6% (figure 5.6). In addition, we developed the APBE with a time-ensemble approach and an incompressibility constraint under the framework of CPWC and TO imaging for NIVE applications. For all simulation and *in vitro* studies, the developed APBE outperformed the original one proposed in the literature.

In Chapter 5, only in-plane motions were considered during a 2-D scan. However, it is recognized that intrinsic 3-D tissue motions should cause speckle decorrelation when performing 2-D strain estimations. The second article in this thesis (Chapter 6) thus evaluated the influence of such out-of-plane motions on the performance of strain estimations with the LSME (as it outperformed the APBE algorithm, as demonstrated in Chapter 5). For this purpose, a novel carotid bifurcation phantom with a stenotic soft inclusion was designed. With it, an *in vitro* experimental setup was built to simulate out-of-plane motions of 1 mm, 2 mm and 3 mm. We found higher strain estimation artifacts with increasing magnitude of out-of-plane motions (figure 6.4 and 6.6). Even so, we still obtained robust strain estimations with 2.0 mm out-of-plane motion. Moreover, less decorrelation artifacts using CPWC imaging than those obtained using focused imaging were noticed, likely due to less inter-frame out-of-plane motions (figure 6.10). For the clinical validation of this work, we used two datasets of scans on the same carotid plaque, in both cross-sectional and longitudinal views, to deduce the out-of-plane motion. The deduced out-of-plane motions from the clinical dataset of 18 participants ranged from 0.25 mm

to 1.04 mm. Clinical results verified *in vitro* results and showed that strain estimates remained reproducible (figure 6.8), which should give confidence on the use of the LSME algorithm for carotid plaque characterization.

The third article of this thesis (Chapter 7) focused on developing a strain estimation algorithm to improve the accuracy of NIVE. Therefore, we only consider affine model-based methods other than displacement-based methods including dense optical flow [112] and cross-correlation-based [145] methods. The reason is that these displacement-based methods have to perform a gradient operation to derive affine strain components, which could induce estimation variances and reduce strain image resolution. Further performance comparison between affine model-based and displacement-based methods could be interestingly investigated. Specifically, we proposed a pixel-based affine strain estimator, the SMSE, to obtain a dense strain field with pixel-wise resolution as well as a high computation efficiency. The global estimation strategy of the SMSE allowed more accurate strain estimations than with the LSME window-based method, for simulations, *in vitro* and *in vivo* results. Moreover, the SMSE is avoiding window effects so as to better characterize small inclusions. In addition, the sparse implementation of the SMSE reduced the processing time by 4 to 25 folds, compared with the LSME, which may allow a possible real time implementation of NIVE.

8.2 Originality of works

The originality of the three main chapters of this thesis was to improve and evaluate the performance of NIVE systematically by ways of advanced beamforming methods, an experimental image acquisition strategy simulating out-of-plane motions, and a novel strain estimation algorithm.

The main contribution of the first article of this thesis was to introduce TO beamforming into NIVE. We are the first to evaluate the performance of TO beamforming on lateral estimations with window-based affine strain estimators. Introducing TO speckles helped the performance of principal strain estimations with the LSME in the case of complex and heterogeneous structures. The second contribution targeted in developing a window-based affine strain estimator, the APBE, with a time-ensemble approach and an incompressibility constraint, whose performance on NIVE using CPWC and TO beamforming was also evaluated

for the first time. We concluded that the developed APBE outperformed the previous one used in the literature for cardiac motion tracking.

The second article of this thesis contained two main original aspects. Firstly, we proposed a framework, including an *in vitro* experimental setup and an evaluation strategy based on a clinical dataset, which allowed studying the impact of out-of-plane motions on strain estimation algorithms and beamforming methods. With this framework, we evaluated the performance of the LSME with different magnitudes of out-of-plane motions using CPWC and line-by-line focused imaging. It was found that axial estimations with the LSME were convincing in the presence of up to 2 mm out-of-plane motion for *in vitro* results, and 1.04 mm out-of-plane motion for clinical ultrasound imaging. Secondly, the influence of out-of-plane motions on NIVE was, for the first time, investigated using two imaging modalities with different imaging frame rates, CPWC with a high frame rate (400 s^{-1}) and line-by-line focused imaging with a low frame rate (25 s^{-1}). *In vitro* results indicated that less inter-frame out-of-plane motion associated with a higher frame rate caused less decorrelation artifacts. This suggests that CPWC imaging may be a better alternative to reduce out-of-plane artifacts for clinical strain assessment of carotid arteries.

The originality of the third article of this thesis (Chapter 7) was to propose a pixel-based affine strain estimator, which parameterized the strain field with DCT coefficients. This parameterized field allowed four main advantages. Firstly, affine strain fields were directly constructed using DCT coefficients without an explicit derivative operation, which eliminated the amplification of high frequency displacement noise of displacement-based methods. Secondly, the displacement representation with DCT coefficients allowed to perform motion estimations within a HS optical flow framework. Thus, we could obtain pixel-wise strain estimations, which avoided disadvantages of window-based methods, such as a trade-off between resolution and estimation accuracy. Thirdly, unlike the HS optical flow, the sparse DCT representation could be solved analytically using a least squares method instead of an iterative minimization, which made the optimization problem more efficient. Moreover, the processing time of this method is only proportional to the pixels inside a vessel wall, not the pixels in the whole image. Thus, the donut geometry of cross-sectional vessel with less pixels than other organs could make possible a real time implementation of NIVE. Fourthly, the proposed DCT-

based framework is open to variant cost functions. The data term, which consists in the optical flow constraint equation in the current SMSE, can be changed with any displacement-based terms. Likewise, the regularization term can also be replaced with other displacement-based spatial or temporal terms.

8.3 Future works

In this thesis, we have improved the accuracy of NIVE systematically from the image formation step to image post-processing development methods in the context of 2-D ultrasound imaging. Some future works could be pursued based on the works of Chapters 5, 6 and 7, respectively. Regarding beamforming, it would be interesting to implement TO (Chapter 5) for NIVE with the proposed SMSE algorithm (Chapter 7). Lateral oscillations could also be beneficial for the SMSE as they did for the LSME, and provide even better estimations with the SMSE as global estimations may be more robust against the loss of lateral resolution and spectrum magnitude of TO images. Like the LSME, the APBE and SMSE robustness could also be investigated against out-of-plane motions using the proposed evaluation framework (Chapter 6). Their performance would need to be evaluated before launching new clinical patient datasets. For affine strain estimators, the SMSE can be implemented as a frequency-domain method instead of a space-domain method by replacing the optical flow constraint equation in (5.1) by an analytic phase correlation equation in (4.8). This implementation could be more suitable for TO images for better lateral estimations. In addition, instead of the pre-defined DCT basis function used in the current SMSE, the motion fields can be formulated by other learned basis functions via dictionary learning [204, 205] or supervised learning [226] that would need large amounts of ground-truth data for the training phase to obtain more accurate reconstructions of motion fields.

Recent works have extended 2-D ultrasound imaging to 3-D using a 2-D matrix array probe. Provost *et al*. [227] demonstrated 3-D ultrafast imaging using either diverging or plane waves for 3-D shear wave and Doppler imaging. Salles *et al*. [169] proposed 3-D TO imaging to characterize tissue motions using a 3-D displacement-based method. A most recent work applied 3-D plane wave imaging into quasi-static elastography to estimate axial strains using a 1-D NCC method [228]. For 2-D affine strain estimators, the APBE, LSME and SMSE can be

easily extended to 3-D. Without the influence of out-of-plane motions, it is expected that more accurate estimations could be obtained with 3-D data. On the other hand, we have shown that introducing a temporal continuity constraint, *i.e.* the time-ensemble approach into the APBE, improved its robustness. Thus, constraining the spatio-temporal behavior of tissues using 3-D data could make it possible to increase the robustness of 3-D estimators. Especially for the SMSE, an additional temporal regularization term can be added in the cost function to take into account tissue acceleration. This new temporal constraint could improve the assessment of vascular wall tissue behavior.

Although the works in Chapter 5 and Chapter 7 have shown an ability to detect a soft inclusion in simulation and in vitro results, they are worthy to be further validated on vulnerable plaques characterized by MRI or histology. To characterize the thin fibrosis cap in a vulnerable plaque, high frequency ultrasound could be an alternative to measure its thickness. Coupling with the high resolution SMSE, the strain difference between the soft lipid core and thin fibrosis cap could be identified.

Some literatures have shown that the strain parameters with the LSME were able to discriminate vulnerable plaques characterized by MRI with 31 patients with symptomatic and asymptomatic stenosis [70, 229]. However, these studies were performed using line-by-line focused imaging. Further clinical data acquisitions using advanced imaging methods, such as plane wave and transverse oscillation imaging are necessary to validate the reproducibility of the proposed methods in this thesis.

In this thesis, we focused on static ultrasound elastography which provides tissue relative elasticity (strain). Another category of elastography is dynamic ultrasound elastography, such as acoustic radiation force imaging (ARFI) and shear wave elastography, which is able to provide tissue absolute elasticity (elastic module). Although it is not able to compare the results of the two categories directly, one possible quantitative comparison is to evaluate the sensitivity and specificity of identifying vulnerable plaques on the same clinical data using these two categories of elastography. This further study is worthy to be investigated.

8.4 General conclusion

Atherosclerosis is a complex vascular disease. The early detection of vulnerable plaques is essential for stroke prevention and evaluation of therapeutic strategies. NIVE has shown great potential for the characterization of vulnerable plaques. It was the objective of this thesis to improve NIVE for becoming a fast and efficient method for early screening and diagnosis of atherosclerosis.

The proposed methods and results of this thesis are suggesting the possibility of using NIVE for clinical assessment of carotid plaques as we should improvements in accuracy and efficiency. Despite there are still many unknown aspects to be explored, we believe that NIVE may become an indispensable diagnostic tool for future clinical examinations.

References

[1] B. W. Parks and A. J. Lusis, "Macrophage accumulation in atherosclerosis," *N Engl J Med,* vol. 369, no. 24, pp. 2352-2353, Dec 12 2013.

[2] L. Cardoso and S. Weinbaum, "Changing views of the biomechanics of vulnerable plaque rupture: a review," *Ann Biomed Eng,* vol. 42, no. 2, pp. 415-431, Feb 2014.

[3] T. M. Freilinger, A. Schindler, C. Schmidt, J. Grimm, C. Cyran, F. Schwarz *et al.*, "Prevalence of nonstenosing, complicated atherosclerotic plaques in cryptogenic stroke," *JACC Cardiovasc Imaging,* vol. 5, no. 4, pp. 397-405, Apr 2012.

[4] N. Horie, M. Morikawa, S. Ishizaka, T. Takeshita, G. So, K. Hayashi *et al.*, "Assessment of carotid plaque stability based on the dynamic enhancement pattern in plaque components with multidetector CT angiography," *Stroke,* vol. 43, no. 2, pp. 393-398, Feb 2012.

[5] Z. Y. Li, S. P. Howarth, T. Tang, and J. H. Gillard, "How critical is fibrous cap thickness to carotid plaque stability? A flow-plaque interaction model," *Stroke,* vol. 37, no. 5, pp. 1195-9, May 2006.

[6] H. H. Hansen, G. J. de Borst, M. L. Bots, F. L. Moll, G. Pasterkamp, and C. L. de Korte, "Validation of noninvasive in vivo compound ultrasound strain imaging using histologic plaque vulnerability features," *Stroke,* vol. 47, no. 11, pp. 2770-2775, Nov 2016.

[7] E. G. Grant, C. B. Benson, G. L. Moneta, A. V. Alexandrov, J. D. Baker, E. I. Bluth *et al.*, "Carotid artery stenosis: gray-scale and Doppler US diagnosis—Society of Radiologists in Ultrasound Consensus Conference," *Radiology* vol. 229, no. 2, pp. 340-346, 2003.

[8] J. Ophir, I. Cespedes, H. Ponnekanti, Y. Yazdi, and X. Li, "Elastography: a quantitative method for imaging the elasticity of biological tissues," *Ultrasonic imaging,* vol. 13, no. 2, pp. 111-134, 1991.

[9] C. L. de Korte, S. G. Carlier, F. Mastik, M. M. Doyley, A. F. van der Steen, P. W. Serruys *et al.*, "Morphological and mechanical information of coronary arteries obtained with intravascular elastography: feasibility study in vivo," *Eur Heart J,* vol. 23, no. 5, pp. 405-413, Mar 2002.

[10] R. L. Maurice, J. Ohayon, Y. Fretigny, M. Bertrand, G. Soulez, and G. Cloutier, "Noninvasive vascular elastography: theoretical framework," *IEEE Transactions on Medical Imaging,* vol. 23, no. 2, pp. 164-180, 2004.

[11] E. Konofagou and J. Ophir, "A new elastographic method for estimation and imaging of lateral displacements, lateral strains, corrected axial strains and Poisson's ratios in tissues," *Ultrasound in Medicine & Biology,* vol. 24, no. 8, pp. 1183-1199, 1998.

[12] H. Ribbers, R. G. Lopata, S. Holewijn, G. Pasterkamp, J. D. Blankensteijn, and C. L. de Korte, "Noninvasive two-dimensional strain imaging of arteries: validation in phantoms and preliminary experience in carotid arteries in vivo," *Ultrasound Med Biol,* vol. 33, no. 4, pp. 530-540, Apr 2007.

[13] M. Rao and T. Varghese, "Estimation of the optimal maximum beam angle and angular increment for normal and shear strain estimation," *IEEE Trans Biomed Eng,* vol. 56, no. 3, pp. 760-9, Mar 2009.

[14] H. H. Hansen, R. G. Lopata, T. Idzenga, and C. L. de Korte, "Full 2D displacement vector and strain tensor estimation for superficial tissue using beam-steered ultrasound imaging," *Physics in Medicine & Biology,* vol. 55, no. 11, pp. 3201-3218, Jun 7 2010.
[15] Z. Liu, Q. He, and J. Luo, "Spatial angular compounding with affine model based optical flow for improvement of motion estimation," *IEEE Transactions on Ultrasonics, Ferroelectrics, and Frequency Control,* vol. 66, no. 4, pp. 701-716, 2019.
[16] K. Liu, P. Zhang, J. Shao, X. Zhu, Y. Zhang, and J. Bai, "A 2D strain estimator with numerical optimization method for soft-tissue elastography," *Ultrasonics,* vol. 49, no. 8, pp. 723-732, Dec 2009.
[17] M. Alessandrini, A. Basarab, L. Boussel, X. Guo, A. Serusclat, D. Friboulet *et al.*, "A new technique for the estimation of cardiac motion in echocardiography based on transverse oscillations: a preliminary evaluation in silico and a feasibility demonstration in vivo," *IEEE Trans Med Imaging,* vol. 33, no. 5, pp. 1148-1162, 2014.
[18] J. Poree, D. Garcia, B. Chayer, J. Ohayon, and G. Cloutier, "Noninvasive vascular elastography with plane strain incompressibility assumption using ultrafast coherent compound plane wave imaging," *IEEE Trans Med Imaging,* vol. 34, no. 12, pp. 2618-2631, Dec 2015.
[19] E. Mercure, G. Cloutier, C. Schmitt, and R. L. Maurice, "Performance evaluation of different implementations of the Lagrangian speckle model estimator for non-invasive vascular ultrasound elastography," *Med Phys,* vol. 35, no. 7, pp. 3116-3126, Jul 2008.
[20] S. Korukonda and M. M. Doyley, "Estimating axial and lateral strain using a synthetic aperture elastographic imaging system," *Ultrasound Med Biol,* vol. 37, no. 11, pp. 1893-1908, Nov 2011.
[21] S. Korukonda and M. M. Doyley, "Visualizing the radial and circumferential strain distribution within vessel phantoms using synthetic-aperture ultrasound elastography," *IEEE Trans Ultrason Ferroelectr Freq Control,* vol. 59, no. 8, pp. 1639-1653, Aug 2012.
[22] S. Salles, A. J. Chee, D. Garcia, A. C. Yu, D. Vray, and H. Liebgott, "2-D arterial wall motion imaging using ultrafast ultrasound and transverse oscillations," *IEEE Trans Ultrason Ferroelectr Freq Control,* vol. 62, no. 6, pp. 1047-1058, Jun 2015.
[23] S. Fekkes, A. E. Swillens, H. H. Hansen, A. E. Saris, M. M. Nillesen, F. Iannaccone *et al.*, "2-D versus 3-D cross-correlation-based radial and circumferential strain estimation using multiplane 2-D ultrafast ultrasound in a 3-D atherosclerotic carotid artery model," *IEEE Trans Ultrason Ferroelectr Freq Control,* vol. 63, no. 10, pp. 1543-1553, Oct 2016.
[24] E. Brusseau, A. Bernard, C. Meynier, P. Chaudet, V. Detti, G. Ferin *et al.*, "Specific ultrasound data acquisition for tissue motion and strain estimation: initial results," *Ultrasound Med Biol,* vol. 43, no. 12, pp. 2904-2913, Dec 2017.
[25] H. Li, J. Poree, M. H. Roy Cardinal, and G. Cloutier, "Two-dimensional affine model-based estimators for principal strain vascular ultrasound elastography with compound plane wave and transverse oscillation beamforming," *Ultrasonics,* vol. 91, pp. 77-91, Jan 2019.
[26] B. K. P. Horn and B. G. Schunck, "Determining optical flow," *Artificial intelligence,* vol. 17, no. 1-3, pp. 185-203, 1981.
[27] J. Poree, M. Baudet, F. Tournoux, G. Cloutier, and D. Garcia, "A dual tissue-Doppler optical-flow method for speckle tracking echocardiography at high frame rate," *IEEE Trans Med Imaging,* vol. 37, no. 9, pp. 2022-2032, Sep 2018.

[28] S. E. Huether and K. L. McCance, "Understanding pathophysiology," *St Louis, MO: Mosby,* 2008.
[29] H. C. Stary, A. B. Chandler, R. E. Dinsmore, V. Fuster, S. Glagov, W. Insull *et al.*, "A definition of advanced types of atherosclerotic lesions and a histological classification of atherosclerosis: a report from the Committee on Vascular Lesions of the Council on Arteriosclerosis, American Heart Association," *Circulation,* vol. 92, no. 5, pp. 1355-1374, 1995.
[30] R. Virmani, F. D. Kolodgie, A. P. Burke, A. Farb, and S. M. Schwartz, "Lessons from sudden coronary death: a comprehensive morphological classification scheme for atherosclerotic lesions," *Arteriosclerosis, thrombosis, and vascular biology,* vol. 20, no. 5, pp. 1262-1275, 2000.
[31] L. G. Spagnoli, A. Mauriello, G. Sangiorgi, S. Fratoni, E. Bonanno, R. S. Schwartz *et al.*, "Extracranial thrombotically active carotid plaque as a risk factor for ischemic stroke," *JAMA,* vol. 292, no. 15, pp. 1845-1852, 2004.
[32] A. Autret, D. Saudeau, P. Bertrand, L. Pourcelot, C. Marchal, and S. D. Boisvilliers, "Stroke risk in patients with carotid stenosis," *The Lancet,* vol. 329, no. 8538, pp. 888-890, 1987.
[33] J. M. U-King-Im, V. Young, and J. H. Gillard, "Carotid-artery imaging in the diagnosis and management of patients at risk of stroke," *The Lancet Neurology* vol. 8, no. 6, pp. 569-580, 2009.
[34] M. S. Dennis, J. M. Bamford, P. A. G. Sandercock, and C. P. Warlow, "A comparison of risk factors and prognosis for transient ischemic attacks and minor ischemic strokes. The Oxfordshire Community Stroke Project," *Stroke,* vol. 20, no. 11, pp. 1494-1499, 1989.
[35] J. S. Suri, C. kathuria, and F. Molinari, "Atherosclerosis disease management," *Springer Science & Business Media,* 2010.
[36] A. Mauriello, G. M. Sangiorgi, R. Virmani, S. Trimarchi, D. R. Holmes, Jr., F. D. Kolodgie *et al.*, "A pathobiologic link between risk factors profile and morphological markers of carotid instability," *Atherosclerosis,* vol. 208, no. 2, pp. 572-580, Feb 2010.
[37] R. Virmani, A. P. Burke, A. Farb, and F. D. Kolodgie, "Pathology of the vulnerable plaque," *J Am Coll Cardiol,* vol. 47, no. 8 Suppl, pp. C13-8, Apr 18 2006.
[38] S. Shindo, K. Fujii, M. Shirakawa, K. Uchida, Y. Enomoto, T. Iwama *et al.*, "Morphologic features of carotid plaque rupture assessed by optical coherence tomography," *American Journal of Neuroradiology,* vol. 36, no. 11, pp. 2140-2146, Nov 2015.
[39] G. Devuyst, T. Karapanayiotides, P. Ruchat, M. Pusztaszeri, J. A. Lobrinus, L. Jonasson *et al.*, "Ultrasound measurement of the fibrous cap in symptomatic and asymptomatic atheromatous carotid plaques," *Circulation,* vol. 111, no. 21, pp. 2776-2782, May 31 2005.
[40] J. N. Redgrave, P. Gallagher, J. K. Lovett, and P. M. Rothwell, "Critical cap thickness and rupture in symptomatic carotid plaques: the oxford plaque study," *Stroke,* vol. 39, no. 6, pp. 1722-1729, Jun 2008.
[41] J. K. DeMarco and J. Huston, "Imaging of high-risk carotid artery plaques: current status and future directions," *Neurosurg Focus,* vol. 36, no. 1, p. E1, Jan 2014.

[42] H. R. Underhill, T. S. Hatsukami, J. Cai, W. Yu, J. K. DeMarco, N. L. Polissar *et al.*, "A noninvasive imaging approach to assess plaque severity: the carotid atherosclerosis score," *AJNR Am J Neuroradiol,* vol. 31, no. 6, pp. 1068-1075, Jun 2010.

[43] V. C. Cappendijk, A. G. Kessels, S. Heeneman, K. B. Cleutjens, G. W. Schurink, R. J. Welten *et al.*, "Comparison of lipid-rich necrotic core size in symptomatic and asymptomatic carotid atherosclerotic plaque: Initial results," *J Magn Reson Imaging,* vol. 27, no. 6, pp. 1356-1361, Jun 2008.

[44] N. M. Bornstein, A. Krajewski, A. J. Lewis, and J. W. Norris, "Clinical significance of carotid plaque hemorrhage," *Archives of neurology,* vol. 47, no. 9, pp. 958-959, 1990.

[45] N. Takaya, C. Yuan, B. Chu, T. Saam, N. L. Polissar, G. P. Jarvik *et al.*, "Presence of intraplaque hemorrhage stimulates progression of carotid atherosclerotic plaques: a high-resolution magnetic resonance imaging study," *Circulation,* vol. 111, no. 21, pp. 2768-2775, May 31 2005.

[46] A. V. Finn, M. Nakano, J. Narula, F. D. Kolodgie, and R. Virmani, "Concept of vulnerable/unstable plaque," *Arterioscler Thromb Vasc Biol,* vol. 30, no. 7, pp. 1282-1292, Jul 2010.

[47] S. Carr, A. Farb, W. H. Pearce, R. Virmani, and J. S. T. Yao, "Atherosclerotic plaque rupture in symptomatic carotid artery stenosis," *Journal of vascular surgery,* vol. 23, no. 5, pp. 755-766, 1996.

[48] L. Remonda, P. Senn, A. Barth, M. Arnold, K.-O. Lovblad, and G. Schroth, "Contrast-enhanced 3D MR angiography of the carotid artery: comparison with conventional digital subtraction angiography," *American Journal of Neuroradiology,* vol. 23, no. 2, pp. 213-219, 2002.

[49] D. Vancraeynest, A. Pasquet, V. Roelants, B. L. Gerber, and J.-L. J. Vanoverschelde, "Imaging the vulnerable plaque," *Journal of the American College of Cardiology,* vol. 57, no. 20, pp. 1961-1979, 2011.

[50] M. R. Elliott and A. J. Thrush, "Measurement of resolution in intravascular ultrasound images," *Physiological measurement,* vol. 17, no. 4, pp. 259-265, 1996.

[51] M. E. Brezinski, G. J. Tearney, N. J. Weissman, S. A. Boppart, B. E. Bouma, M. R. Hee *et al.*, "Assessing atherosclerotic plaque morphology: comparison of optical coherence tomography and high frequency intravascular ultrasound," *Heart,* vol. 77, no. 5, pp. 397-403, 1997.

[52] T. Ma, M. Yu, Z. Chen, C. Fei, K. K. Shung, and Q. Zhou, "Multi-frequency intravascular ultrasound (IVUS) imaging," *IEEE Trans Ultrason Ferroelectr Freq Control,* vol. 62, no. 1, pp. 97-107, 2015.

[53] H. T. Räsänen, H. I. Manninen, R. L. Vanninen, P. Vainio, M. Berg, and T. Saari, "Mild carotid artery atherosclerosis: assessment by 3-dimensional time-of-flight magnetic resonance angiography, with reference to intravascular ultrasound imaging and contrast angiography," *Stroke,* vol. 30, no. 4, pp. 827-833, 1999.

[54] G. J. Tearney, H. Yabushita, S. L. Houser, H. T. Aretz, I.-K. Jang, K. H. Schlendorf *et al.*, "Quantification of macrophage content in atherosclerotic plaques by optical coherence tomography," *Circulation,* vol. 107, no. 1, pp. 113-119, 2003.

[55] D. H. O'Leary and M. L. Bots, "Imaging of atherosclerosis: carotid intima-media thickness," *European Heart Journal,* vol. 31, no. 14, pp. 1682-1689, Jul 2010.

[56] A. Thapar, I. H. Jenkins, A. Mehta, and A. H. Davies, "Diagnosis and management of carotid atherosclerosis," *BMJ,* vol. 346, p. f1485, Mar 18 2013.

[57] L. Saba, C. Yuan, T. S. Hatsukami, N. Balu, Y. Qiao, J. K. DeMarco *et al.*, "Carotid Artery Wall Imaging: Perspective and Guidelines from the ASNR Vessel Wall Imaging Study Group and Expert Consensus Recommendations of the American Society of Neuroradiology," *American Journal of Neuroradiology,* vol. 39, no. 2, pp. E9-E31, Feb 2018.

[58] T. T. de Weert, M. Ouhlous, E. Meijering, P. E. Zondervan, J. M. Hendriks, M. R. van Sambeek *et al.*, "In vivo characterization and quantification of atherosclerotic carotid plaque components with multidetector computed tomography and histopathological correlation," *Arterioscler Thromb Vasc Biol,* vol. 26, no. 10, pp. 2366-2372, Oct 2006.

[59] L. Saba, R. Sanfilippo, S. Sannia, M. Anzidei, R. Montisci, G. Mallarini *et al.*, "Association between carotid artery plaque volume, composition, and ulceration: a retrospective assessment with MDCT," *AJR Am J Roentgenol,* vol. 199, no. 1, pp. 151-156, Jul 2012.

[60] J. Cai, T. S. Hatsukami, M. S. Ferguson, W. S. Kerwin, T. Saam, B. Chu *et al.*, "In vivo quantitative measurement of intact fibrous cap and lipid-rich necrotic core size in atherosclerotic carotid plaque: comparison of high-resolution, contrast-enhanced magnetic resonance imaging and histology," *Circulation,* vol. 112, no. 22, pp. 3437-3744, Nov 29 2005.

[61] S. Partovi, M. Loebe, M. Aschwanden, T. Baldi, K. A. Jager, S. B. Feinstein *et al.*, "Contrast-enhanced ultrasound for assessing carotid atherosclerotic plaque lesions," *AJR Am J Roentgenol,* vol. 198, no. 1, pp. W13-W19, Jan 2012.

[62] K. Saito, K. Nagatsuka, H. Ishibashi-Ueda, A. Watanabe, H. Kannki, and K. Iihara, "Contrast-enhanced ultrasound for the evaluation of neovascularization in atherosclerotic carotid artery plaques," *Stroke,* vol. 45, no. 10, pp. 3073-3075, Oct 2014.

[63] Z. Akkus, A. Hoogi, G. Renaud, S. C. van den Oord, G. L. Ten Kate, A. F. Schinkel *et al.*, "New quantification methods for carotid intra-plaque neovascularization using contrast-enhanced ultrasound," *Ultrasound Med Biol,* vol. 40, no. 1, pp. 25-36, Jan 2014.

[64] A. S. Jaipersad, A. Shantsila, S. Silverman, G. Y. Lip, and E. Shantsila, "Evaluation of carotid plaque neovascularization using contrast ultrasound," *Angiology,* vol. 64, no. 6, pp. 447-550, Aug 2013.

[65] J. R. Davies, J. H. Rudd, P. L. Weissberg, and J. Narula, "Radionuclide imaging for the detection of inflammation in vulnerable plaques," *J Am Coll Cardiol,* vol. 47, no. 8 Suppl, pp. C57-68, Apr 18 2006.

[66] A. Tawakol, R. Q. Migrino, G. G. Bashian, S. Bedri, D. Vermylen, R. C. Cury *et al.*, "In vivo 18F-fluorodeoxyglucose positron emission tomography imaging provides a noninvasive measure of carotid plaque inflammation in patients," *J Am Coll Cardiol,* vol. 48, no. 9, pp. 1818-1824, Nov 7 2006.

[67] L. Hermus, G. M. van Dam, and C. J. Zeebregts, "Advanced carotid plaque imaging," *Eur J Vasc Endovasc Surg,* vol. 39, no. 2, pp. 125-133, Feb 2010.

[68] J. Chen, C.-H. Tung, U. Mahmood, V. Ntziachristos, R. Gyurko, M. C. Fishman *et al.*, "In Vivo Imaging of Proteolytic Activity in Atherosclerosis," *Circulation,* vol. 105, no. 23, pp. 2766-2771, 2002.

[69] J. O. Deguchi, M. Aikawa, C. H. Tung, E. Aikawa, D. E. Kim, V. Ntziachristos *et al.*, "Inflammation in atherosclerosis: visualizing matrix metalloproteinase action in macrophages in vivo," *Circulation,* vol. 114, no. 1, pp. 55-62, Jul 4 2006.

[70] M. H. Roy Cardinal, M. H. G. Heusinkveld, Z. Qin, R. G. P. Lopata, C. Naim, G. Soulez *et al.*, "Carotid artery plaque vulnerability assessment using noninvasive ultrasound elastography: Validation with MRI," *AJR Am J Roentgenol,* vol. 209, no. 1, pp. 142-151, Jul 2017.

[71] J. Bercoff, "Ultrafast ultrasound imaging," in *Ultrasound imaging-Medical applications*: IntechOpen, 2011.

[72] P.-C. Li and M.-L. Li, "Adaptive imaging using the generalized coherence factor," *IEEE Transactions on Ultrasonics, Ferroelectrics, and Frequency Control,* vol. 50, no. 2, pp. 128-141.

[73] J. F. Synnevag, A. Austeng, and S. Holm, "Adaptive beamforming applied to medical ultrasound imaging," *IEEE Transactions on Ultrasonics, Ferroelectrics and Frequency Control,* vol. 54, no. 8, pp. 1606-1613, 2007.

[74] S.-L. Wang and P.-C. Li, "MVDR-based coherence weighting for high-frame-rate adaptive imaging," *IEEE Transactions on Ultrasonics, Ferroelectrics, and Frequency Control,* vol. 56, no. 10, pp. 2097-2110.

[75] J. Zhao, Y. Wang, X. Zeng, J. Yu, B. Y. Yiu, and A. C. Yu, "Plane wave compounding based on a joint transmitting-receiving adaptive beamformer," *IEEE Trans Ultrason Ferroelectr Freq Control,* vol. 62, no. 8, pp. 1440-1452, Aug 2015.

[76] G. Matrone, A. S. Savoia, G. Caliano, and G. Magenes, "The delay multiply and sum beamforming algorithm in ultrasound B-mode medical imaging," *IEEE Trans Med Imaging,* vol. 34, no. 4, pp. 940-949, Apr 2015.

[77] G. R. Lockwood and F. S. Foster, "Design of sparse array imaging systems," *IEEE Ultrasonics Symposium,* vol. 2, pp. 1237-1243, 1995.

[78] G. Montaldo, M. Tanter, J. Bercoff, N. Benech, and M. Fink, "Coherent plane-wave compounding for very high frame rate ultrasonography and transient elastography," *IEEE Transactions on Ultrasonics, Ferroelectrics and Frequency Control,* vol. 56, no. 3, pp. 489-506, 2009.

[79] J. A. Jensen and P. Munk, "A new method for estimation of velocity vectors," *IEEE Transactions on Ultrasonics, Ferroelectrics, and Frequency Control,* vol. 45, pp. 886-894, 1998.

[80] M. E. Anderson, "Multi-dimensional velocity estimation with ultrasound using spatial quadrature," *IEEE Transactions on Ultrasonics, Ferroelectrics and Frequency Control,* vol. 45, pp. 852-861, 1998.

[81] H. Liebgott, J. Wilhjelm, J. Jensen, D. Vray, and P. Delachartre, "PSF dedicated to estimation of displacement vectors for tissue elasticity imaging with ultrasound," *IEEE Transactions on Ultrasonics, Ferroelectrics and Frequency Control,* vol. 54, no. 4, pp. 746-756, 2007.

[82] M. Lenge, A. Ramalli, P. Tortoli, C. Cachard, and H. Liebgott, "Plane-wave transverse oscillation for high-frame-rate 2-D vector flow imaging," *IEEE Trans Ultrason Ferroelectr Freq Control,* vol. 62, no. 12, pp. 2126-2137, Dec 2015.

[83] K. R. Nightingale, M. L. Palmeri, R. W. Nightingale, and G. E. Trahey, "On the feasibility of remote palpation using acoustic radiation force," *J Acoust Soc Am,* vol. 110, no. 1, pp. 625-634, Jul 2001.

[84] E. E. Konofagou, J. D'hooge, and J. Ophir, "Myocardial elastography—A feasibility study in vivo," *Ultrasound in medicine & biology,* vol. 28, no. 4, pp. 475-482, 2002.

[85] C. L. de Korte, A. F. van der Steen, E. I. Céspedes, G. Pasterkamp, S. G. Carlier, F. Mastik *et al.*, "Characterization of plaque components andvulnerability with intravascular ultrasound elastography," *Physics in Medicine & Biology,* vol. 45, no. 6, pp. 1465-1475, 2000.

[86] C. Schmitt, G. Soulez, R. L. Maurice, M. F. Giroux, and G. Cloutier, "Noninvasive vascular elastography: toward a complementary characterization tool of atherosclerosis in carotid arteries," *Ultrasound Med Biol,* vol. 33, no. 12, pp. 1841-1858, Dec 2007.

[87] A. P. Sarvazyan, O. V. Rudenko, S. D. Swanson, J. B. Fowlkes, and S. Y. Emelianov, "Shear wave elasticity imaging: a new ultrasonic technology of medical diagnostics," *Ultrasound in medicine & biology,* vol. 24, no. 9, pp. 1419-1435, 1998.

[88] L. Sandrin, B. Fourquet, J. M. Hasquenoph, S. Yon, C. Fournier, F. Mal *et al.*, "Transient elastography: a new noninvasive method for assessment of hepatic fibrosis," *Ultrasound in medicine & biology,* vol. 29, no. 12, pp. 1705-1713, 2003.

[89] J. Bercoff, M. Tanter, and M. Fink, "Supersonic shear imaging: a new technique for soft tissue elasticity mapping," *IEEE transactions on ultrasonics, ferroelectrics, and frequency control,* vol. 51, no. 4, pp. 396-409, 2004.

[90] T. Shiina, K. R. Nightingale, M. L. Palmeri, T. J. Hall, J. C. Bamber, R. G. Barr *et al.*, "WFUMB guidelines and recommendations for clinical use of ultrasound elastography: Part 1: basic principles and terminology," *Ultrasound Med Biol,* vol. 41, no. 5, pp. 1126-1147, May 2015.

[91] S. Selladurai and A. K. Thittai, "Strategies to obtain subpitch precision in lateral motion estimation in ultrasound elastography," *IEEE Trans Ultrason Ferroelectr Freq Control,* vol. 65, no. 3, pp. 448-456, Mar 2018.

[92] R. G. Lopata, M. M. Nillesen, H. H. Hansen, I. H. Gerrits, J. M. Thijssen, and C. L. de Korte, "Performance evaluation of methods for two-dimensional displacement and strain estimation using ultrasound radio frequency data," *Ultrasound Med Biol,* vol. 35, no. 5, pp. 796-812, May 2009.

[93] R. Z. Azar, O. Goksel, and S. E. Salcudean, "Sub-sample displacement estimation from digitized ultrasound RF signals using multi-dimensional polynomial fitting of the cross-correlation function," *IEEE transactions on ultrasonics, ferroelectrics, and frequency control,* vol. 57, no. 11, pp. 2403-2420, 2010.

[94] M. McCormick, T. Varghese, X. Wang, C. Mitchell, M. A. Kliewer, and R. J. Dempsey, "Methods for robust in vivo strain estimation in the carotid artery," *Phys Med Biol,* vol. 57, no. 22, pp. 7329-7353, Nov 21 2012.

[95] J. Jiang and T. J. Hall, "A coupled subsample displacement estimation method for ultrasound-based strain elastography," *Phys Med Biol,* vol. 60, no. 21, pp. 8347-8364, Nov 7 2015.

[96] P. Chaturvedi, M. F. Insana, and T. J. Hall, "2-D companding for noise reduction in strain imaging," *IEEE Transactions on Ultrasonics, Ferroelectrics and Frequency Control,* vol. 45, no. 1, pp. 179-191, 1998.

[97] F. Viola, R. L. Coe, K. Owen, D. A. Guenther, and W. F. Walker, "MUlti-Dimensional Spline-Based Estimator (MUSE) for motion estimation: algorithm development and initial results," *Ann Biomed Eng,* vol. 36, no. 12, pp. 1942-1960, Dec 2008.

[98] C. Pellot-Barakat, F. Frouin, M. F. Insana, and A. Herment, "Ultrasound elastography based on multiscale estimations of regularized displacement fields," *IEEE Trans Med Imaging,* vol. 23, no. 2, pp. 153-163, Feb 2004.

[99] H. Rivaz, E. Boctor, P. Foroughi, R. Zellars, G. Fichtinger, and G. Hager, "Ultrasound elastography: a dynamic programming approach," *IEEE Trans Med Imaging,* vol. 27, no. 10, pp. 1373-1377, Oct 2008.
[100] J. Jiang and T. J. Hall, "A generalized speckle tracking algorithm for ultrasonic strain imaging using dynamic programming," *Ultrasound Med Biol,* vol. 35, no. 11, pp. 1863-1879, Nov 2009.
[101] M. McCormick, N. Rubert, and T. Varghese, "Bayesian regularization applied to ultrasound strain imaging," *IEEE Trans Biomed Eng,* vol. 58, no. 6, pp. 1612-1620, Jun 2011.
[102] B. D. Lucas and T. Kanade, "An iterative image registration technique with an application to stereo vision," *Proceedings of Imaging Understanding Workshop,* pp. 121-130, 1981.
[103] Y. Zhou and Y.-P. Zheng, "A motion estimation refinement framework for real-time tissue axial strain estimation with freehand ultrasound," *IEEE transactions on ultrasonics, ferroelectrics, and frequency control,* vol. 57, no. 9, pp. 1943-1951, 2010.
[104] S. K. Alam, F. L. Lizzi, T. Varghese, E. J. Feleppa, and S. Ramachandran, "Adaptive spectral strain estimators for elastography," *Ultrasonic imaging,* vol. 26, no. 3, pp. 131-149, 2004.
[105] F. Kallel and J. Ophir, "A least-squares strain estimator for elastography," *Ultrasonic imaging,* vol. 19, pp. 195-208, 1997.
[106] M. Omidyeganeh, Y. Xiao, M. O. Ahmad, and H. Rivaz, "Estimation of strain elastography from ultrasound radio-frequency data by utilizing analytic gradient of the similarity metric," *IEEE Trans Med Imaging,* vol. 36, no. 6, pp. 1347-1358, Jun 2017.
[107] R. L. Maurice, M. Daronat, J. Ohayon, É. Stoyanova, F. S. Foster, and G. Cloutier, "Non-invasive high-frequency vascular ultrasound elastography," *Physics in Medicine and Biology,* vol. 50, no. 7, pp. 1611-1628, 2005.
[108] C. Sumi, "Fine elasticity imaging utilizing the iterative RF-echo phase matching method," *IEEE Transactions on Ultrasonics, Ferroelectrics and Frequency Control,* vol. 46, no. 1, pp. 158-166, 1999.
[109] A. Basarab, P. Gueth, H. Liebgott, and P. Delachartre, "Phase-based block matching applied to motion estimation with unconventional beamforming strategies," *IEEE Transactions on Ultrasonics, Ferroelectrics and Frequency Control,* vol. 56, no. 5, pp. 945-957, 2009.
[110] H. Li, J. Porée, and G. Cloutier, "A modified affine phase-based estimator for noninvasive vascular ultrasound elastography using coherent plane wave compounding and transverse oscillation imaging," *IEEE International Ultrasonics Symposium,* pp. 1-4, 2016.
[111] M. Ashikuzzaman, C. J. Gauthier, and H. Rivaz, "Global ultrasound elastography in spatial and temporal domains," *IEEE Trans Ultrason Ferroelectr Freq Control,* vol. 66, no. 5, pp. 876-887, May 2019.
[112] A. A. Khan, S. Sikdar, T. Hatsukami, J. Cebral, M. Jones, J. Huston *et al.*, "Noninvasive characterization of carotid plaque strain," *J Vasc Surg,* vol. 65, no. 6, pp. 1653-1663, Jun 2017.
[113] Y. Zhang, H. Li, H. Zheng, and Y. Kang, "Strain estimation method based on 2D companding and optical flow," *Journal of Northeastern University,* vol. 35, no. 7, pp. 917-921, 2014-07-15 2014.

[114] Y. Zhang, S. Li, X. Li, H. Li, and H. Zheng, "A method of ultrasonic strain estimation under large tissue compression," *2013 IEEE International Conference on Medical Imaging Physics and Engineering,* pp. 158-161, 2013.
[115] E. Brusseau, J. Kybic, J. F. Deprez, and O. Basset, "2-D locally regularized tissue strain estimation from radio-frequency ultrasound images: theoretical developments and results on experimental data," *IEEE Trans Med Imaging,* vol. 27, no. 2, pp. 145-160, Feb 2008.
[116] H. Rivaz, E. M. Boctor, M. A. Choti, and G. D. Hager, "Real-time regularized ultrasound elastography," *IEEE Trans Med Imaging,* vol. 30, no. 4, pp. 928-45, Apr 2011.
[117] H. Rivaz, E. M. Boctor, M. A. Choti, and G. D. Hager, "Ultrasound elastography using multiple images," *Med Image Anal,* vol. 18, no. 2, pp. 314-329, Feb 2014.
[118] H. S. Hashemi and H. Rivaz, "Global time-delay estimation in ultrasound elastography," *IEEE Transactions on Ultrasonics, Ferroelectrics and Frequency Control,* vol. 64, no. 10, pp. 1625-1636, 2017.
[119] S. K. Alam, J. Ophir, and E. E. Konofagou, "An adaptive strain estimator for elastography," *IEEE transactions on ultrasonics, ferroelectrics, and frequency control,* vol. 45, no. 2, pp. 461-472, 1998.
[120] M. A. Hussain, E. M. Abu Anas, S. K. Alam, S. Y. Lee, and M. K. Hasan, "Direct and gradient-based average strain estimation by using weighted nearest neighbor cross-correlation peaks," *IEEE Trans Ultrason Ferroelectr Freq Control,* vol. 59, no. 8, pp. 1713-1728, Aug 2012.
[121] S. R. Ara, F. Mohsin, F. Alam, S. A. Rupa, S. Y. Lee, and M. K. Hasan, "Phase-based direct average strain estimation for elastography," *IEEE transactions on ultrasonics, ferroelectrics, and frequency control,* vol. 66, no. 11, pp. 2266-2283, 2013.
[122] E. E. Konofagou, T. Varghese, J. Ophir, and S. K. Alam, "Power spectral strain estimators in elastography," *Ultrasound in Medicine & Biology,* vol. 25, no. 7, pp. 1115-1129, 1999.
[123] T. Varghese, E. E. Konofagou, J. Ophir, S. K. Alam, and M. Bilgen, "Direct strain estimation in elastography using spectral cross-correlation," *Ultrasound in Medicine & Biology,* vol. 26, no. 9, pp. 1525-1537, 2000.
[124] R. Nayak, S. Huntzicker, J. Ohayon, N. Carson, V. Dogra, G. Schifitto *et al.*, "Principal strain vascular elastography: simulation and preliminary clinical evaluation," *Ultrasound Med Biol,* vol. 43, no. 3, pp. 682-699, Mar 2017.
[125] M. M. Doyley, J. C. Bamber, F. Fuechsel, and N. L. Bush, "A freehand elastographic imaging approach for clinical breast imaging: system development and performance evaluation," *Ultrasound in medicine & biology,* vol. 27, no. 10, pp. 1347-1357, 2001.
[126] J. Luo and E. E. Konofagou, "A fast normalized cross-correlation calculation method for motion estimation," *IEEE transactions on ultrasonics, ferroelectrics, and frequency control,* vol. 57, no. 6, pp. 1347-1357, 2010.
[127] M. Larsson, B. Heyde, F. Kremer, L. A. Brodin, and J. D'Hooge, "Ultrasound speckle tracking for radial, longitudinal and circumferential strain estimation of the carotid artery-an in vitro validation via sonomicrometry using clinical and high-frequency ultrasound," *Ultrasonics,* vol. 56, pp. 399-408, Feb 2015.
[128] M. A. Lubinski, S. Y. Emelianov, and M. O'Donnell, "Speckle tracking methods for ultrasonic elasticity imaging using short-time correlation," *IEEE transactions on ultrasonics, ferroelectrics, and frequency control,* vol. 46, no. 1, pp. 82-96, 1999.

[129] S. Golemati, A. Sassano, M. J. Lever, A. A. Bharath, S. Dhanjil, and A. N. Nicolaides, "Carotid artery wall motion estimated from b-mode ultrasound using region tracking and block matching," *Ultrasound in Medicine & Biology,* vol. 29, no. 3, pp. 387-399, 2003.
[130] H. Li, Y. Guo, and W. N. Lee, "Systematic performance evaluation of a cross-correlation-based ultrasound strain imaging method," *Ultrasound Med Biol,* vol. 42, no. 10, pp. 2436-2456, Oct 2016.
[131] K. Kaluzynski, X. Chen, S. Y. Emelianov, A. R. Skovoroda, and M. O'Donnel, "Strain rate imaging using two-dimensional speckle tracking," *IEEE Transctions on Ultrasonics, Ferroelectrics, and Frequency control,* vol. 48, no. 4, pp. 1111-1123, 2001.
[132] X. Chen, M. J. Zohdy, S. Y. Emelianov, and M. O'Donnel, "Lateral speckle tracking using synthetic lateral phase," *IEEE Transactions on Ultrasonics, Ferroelectrics, and Frequency Control,* vol. 51, no. 5, pp. 540-550, 2004.
[133] E. S. Ebbini, "Phase-coupled two-dimensional speckle tracking algorithm," *IEEE transactions on ultrasonics, ferroelectrics, and frequency control,* vol. 53, no. 5, pp. 972-990, 2006.
[134] V. Behar, D. Adam, P. Lysyansky, and Z. Friedman, "Improving motion estimation by accounting for local image distortion," *Ultrasonics,* vol. 43, no. 1, pp. 57-65, Oct 2004.
[135] S. K. Alam and J. Ophir, "Reduction of signal decorrelation from mechanical compression of tissues by temporal stretching: Applications to elastography," *Ultrasound in medicine & biology,* vol. 23, no. 1, pp. 95-105, 1997.
[136] H. Chen, H. Shi, and T. Varghese, "Improvement of elastographic displacement estimation using a two-step cross-correlation method," *Ultrasound in medicine & biology,* vol. 33, no. 1, pp. 48-56, 2007.
[137] H. Shi and T. Varghese, "Two-dimensional multi-level strain estimation for discontinuous tissue," *Phys Med Biol,* vol. 52, no. 2, pp. 389-401, Jan 21 2007.
[138] R. G. P. Lopata, H. H. G. Hansen, M. M. Nillesen, J. M. Thijssen, L. Kapusta, and C. L. d. Korte, "Methodical study on the estimation of strain in shearing and rotating structures using radio frequency ultrasound based on 1-D and 2-D strain estimation techniques," *IEEE transactions on ultrasonics, ferroelectrics, and frequency control,* vol. 57, no. 4, pp. 855-865, 2010.
[139] X. Pan, J. Gao, S. Tao, K. Liu, J. Bai, and J. Luo, "A two-step optical flow method for strain estimation in elastography: Simulation and phantom study," *Ultrasonics,* vol. 54, no. 4, pp. 990-996, Apr 2014.
[140] A. Basarab, H. Liebgott, and P. Delachartre, "Analytic estimation of subsample spatial shift using the phases of multidimensional analytic signals," *IEEE Trans Image Process,* vol. 18, no. 2, pp. 440-447, Feb 2009.
[141] F. Varray and H. Liebgott, "Multi-resolution transverse oscillation in ultrasound imaging for motion estimation," *IEEE Trans Ultrason Ferroelectr Freq Control,* vol. 60, no. 7, pp. 1333-1342, Jul 2013.
[142] M. A. Lubinski, S. Y. Emelianov, K. R. Raghavan, A. E. Yagle, A. R. Skovoroda, and M. O'Donnell, "Lateral displacement estimation using tissue incompressibility," *IEEE Transactions on Ultrasonics, Ferroelectrics, and Frequency Control,* vol. 43, no. 2, pp. 247-256, 1996.
[143] U. Techavipoo, Q. Chen, T. Varghese, and J. A. Zagzebski, "Estimation of displacement vectors and strain tensors in elastography using angular insonifications," *IEEE Trans Med Imaging,* vol. 23, no. 12, pp. 1479-1489, Dec 2004.

[144] M. Rao, Q. Chen, H. Shi, and T. Varghese, "Spatial-angular compounding for elastography using beam steering on linear array transducers," *Medical physics,* vol. 33, no. 3, pp. 618-626, 2006.
[145] H. Hansen, R. Lopata, and C. L. de Korte, "Noninvasive carotid strain imaging using angular compounding at large beam steered angles: Validation in vessel phantoms," *IEEE Transactions on Medical Imaging,* vol. 28, no. 6, pp. 872-880, 2009.
[146] H. H. Hansen, R. G. Lopata, T. Idzenga, and C. L. de Korte, "An angular compounding technique using displacement projection for noninvasive ultrasound strain imaging of vessel cross-sections," *Ultrasound Med Biol,* vol. 36, no. 11, pp. 1947-1956, Nov 2010.
[147] S. Korukonda, R. Nayak, N. Carson, G. Schifitto, V. Dogra, and M. M. Doyley, "Noninvasive vascular elastography using plane-wave and sparse-array imaging," *IEEE Trans Ultrason Ferroelectr Freq Control,* vol. 60, no. 2, pp. 332-342, Feb 2013.
[148] H. H. Hansen, A. E. Saris, N. R. Vaka, M. M. Nillesen, and C. L. de Korte, "Ultrafast vascular strain compounding using plane wave transmission," *J Biomech,* vol. 47, no. 4, pp. 815-823, Mar 3 2014.
[149] J. A. Jensen, "A new estimator for vector velocity estimation," *IEEE transactions on ultrasonics, ferroelectrics, and frequency control,* vol. 48, no. 4, pp. 886-894, 2001.
[150] S. Salles, D. Garcia, B. Bou-Saïd, F. Savary, A. Sérusclat, D. Vray *et al.*, "Plane wave transverse oscillation (PWTO): An ultra-fast transverse oscillation imaging mode performed in the Fourier domain for 2D motion estimation of the carotid artery," *IEEE 11th International Symposium on Biomedical Imaging (ISBI),* p. 14091412, 2014.
[151] H. Liebgott, A. Basarab, P. Gueth, D. Friboulet, and P. Delachartre, "Transverse oscillations for tissue motion estimation," *Ultrasonics,* vol. 50, no. 6, pp. 548-555, May 2010.
[152] *"Index of /ius-special-issue-2014", Creatis.insa-lyon.fr, (2014).* http://www.creatis.insa-lyon.fr/ius-special-issue-2014/.
[153] D. R. Nolan and J. P. McGarry, "On the Compressibility of Arterial Tissue," *Ann Biomed Eng,* vol. 44, no. 4, pp. 993-1007, Apr 2016.
[154] R. A. Baldewsing, J. A. Schaar, F. Mastik, C. W. J. Oomens, and A. F. W. van der Steen, "Assessment of vulnerable plaque composition by matching the deformation of a parametric plaque model to measured plaque deformation," *IEEE Transactions on Medical Imaging,* vol. 24, no. 4, pp. 514-528, 2005.
[155] C. D. Meinhart, S. T. Wereley, and J. G. Santiago, "A PIV algorithm for estimating time-averaged velocity fields," *Journal of Fluids Engineering,* vol. 122, no. 2, pp. 285-289, 2000.
[156] P. W. Holland and R. E. Welsch, "Robust regression using iteratively reweighted least-squares," *Communications in Statistics - Theory and Methods,* vol. 6, no. 9, pp. 813-827, 1977/01/01 1977.
[157] J. Poree, B. Chayer, G. Soulez, J. Ohayon, and G. Cloutier, "Noninvasive vascular modulography method for imaging the local elasticity of atherosclerotic plaques: simulation and in vitro vessel phantom study," *IEEE Trans Ultrason Ferroelectr Freq Control,* vol. 64, no. 12, pp. 1805-1817, Dec 2017.
[158] A. C. Akyildiz, L. Speelman, and F. J. Gijsen, "Mechanical properties of human atherosclerotic intima tissue," *J Biomech,* vol. 47, no. 4, pp. 773-783, Mar 3 2014.

[159] G. C. Cheng, H. M. Loree, R. D. Kamm, M. C. Fishbein, and R. T. Lee, "Distribution of circumferential stress in ruptured and stable atherosclerotic lesions. A structural analysis with histopathological correlation," *Circulation,* vol. 87, no. 4, pp. 1179-1187, 1993.
[160] G. Finet, J. Ohayon, and G. Rioufol, "Biomechanical interaction between cap thickness, lipid core composition and blood pressure in vulnerable coronary plaque: impact on stability or instability," *Coronary artery disease,* vol. 15, no. 1, pp. 13-20, 2004.
[161] S. Le Floc'h, J. Ohayon, P. Tracqui, G. Finet, A. M. Gharib, R. L. Maurice *et al.*, "Vulnerable atherosclerotic plaque elasticity reconstruction based on a segmentation-driven optimization procedure using strain measurements: theoretical framework," *IEEE Trans Med Imaging,* vol. 28, no. 7, pp. 1126-1137, Jul 2009.
[162] A. Bouvier, F. Deleaval, M. M. Doyley, S. K. Yazdani, G. Finet, S. Le Floc'h *et al.*, "A direct vulnerable atherosclerotic plaque elasticity reconstruction method based on an original material-finite element formulation: theoretical framework," *Phys Med Biol,* vol. 58, no. 23, pp. 8457-8476, Dec 7 2013.
[163] A. Tacheau, S. Le Floc'h, G. Finet, M. M. Doyley, R. I. Pettigrew, G. Cloutier *et al.*, "The imaging modulography technique revisited for high-definition intravascular ultrasound: Theoretical framework," *Ultrasound Med Biol,* vol. 42, no. 3, pp. 727-741, Mar 2016.
[164] J. A. Jensen, "Field: A program for simulating ultrasound systems," *Medical & Biological Engineering & Computing,* vol. 34, no. 1, pp. 351-353, 1996.
[165] R. F. Wagner, S. W. Smith, J. M. Sandrik, and H. Lopez, "Statistics of speckle in ultrasound B-Scans," *IEEE Transactions on Sonics and Ultrasonics,* vol. 30, no. 3, pp. 156-163, 1983.
[166] J. Fromageau, J. L. Gennisson, C. Schmitt, R. L. Maurice, R. Mongrain, and G. Cloutier, "Estimation of polyvinyl alcohol cryogel mechanical properties with four ultrasound elastography methods and comparison with gold standard testings," *IEEE Transactions on Ultrasonics, Ferroelectrics and Frequency Control,* vol. 54, no. 3, pp. 498-509, 2007.
[167] G. T. Mase and G. E. Mase, *Continuum Mechanics for Engineers*. 1992.
[168] B. M. Shapo, J. R. Crowe, A. R. Skovoroda, M. J. Eberle, N. A. Cohn, and M. O'Donnell, "Displacement and strain imaging of coronary arteries with intraluminal ultrasound," *IEEE Transactions on Ultrasonics, Ferroelectrics and Frequency Control,* vol. 43, no. 2, pp. 234-246, 1996.
[169] S. Salles, H. Liebgott, D. Garcia, and D. Vray, "Full 3-D transverse oscillations: a method for tissue motion estimation," *IEEE Trans Ultrason Ferroelectr Freq Control,* vol. 62, no. 8, pp. 1473-85, Aug 2015.
[170] T. Hastie, R. Tibshirani, and J. Friedman, "The elements of statistical learning.," vol. Elements, no. 1, pp. 337-387, 2009.
[171] C. Fermüller, D. Shulman, and Y. Aloimonos, "The Statistics of Optical Flow," *Computer Vision and Image Understanding,* vol. 82, no. 1, pp. 1-32, 2001.
[172] B. Byram, G. E. Trahey, and M. Palmeri, "Bayesian speckle tracking. Part II: biased ultrasound displacement estimation," *IEEE Trans Ultrason Ferroelectr Freq Control,* vol. 60, no. 1, pp. 144-157, Jan 2013.
[173] Z. Corbyn, "A growing global burden," *Nature,* vol. 510, no. 7506, pp. S2-S2, 2014.
[174] J. Blacher, B. Pannier, A. P. Guerin, S. J. Marchais, M. E. Safar, and G. M. London, "Carotid arterial stiffness as a predictor of cardiovascular and all-cause mortality in end-stage renal disease," *Hypertension,* vol. 32, no. 3, pp. 570-574, 1998.

[175] J. Capon, "High-resolution frequency-wavenumber spectrum analysis," *Proceedings of the IEEE,* vol. 57, no. 8, pp. 1408-1418, 1969.
[176] N. Bottenus and G. E. Trahey, "Evaluation of the transverse oscillation method using the Cramer-Rao lower bound," *IEEE Trans Ultrason Ferroelectr Freq Control,* vol. 62, no. 11, pp. 2009-2017, Nov 2015.
[177] B. Heyde, N. Bottenus, J. D'Hooge, and G. E. Trahey, "Evaluation of the transverse oscillation technique for cardiac phased array imaging: A theoretical study," *IEEE Trans Ultrason Ferroelectr Freq Control,* vol. 64, no. 2, pp. 320-334, Feb 2017.
[178] H. Kanai, H. Hasegawa, M. Ichiki, F. Tezuka, and Y. Koiwa, "Elasticity imaging of atheroma with transcutaneous ultrasound: preliminary study," *Circulation,* vol. 107, no. 24, pp. 3018-3021, Jun 24 2003.
[179] J. Luo and E. E. Konofagou, "Imaging of wall motion coupled with blood flow velocity in the heart and vessels in vivo: a feasibility study," *Ultrasound Med Biol,* vol. 37, no. 6, pp. 980-995, Jun 2011.
[180] E. Widman, K. Caidahl, B. Heyde, J. D'Hooge, and M. Larsson, "Ultrasound speckle tracking strain estimation of in vivo carotid artery plaque with in vitro sonomicrometry validation," *Ultrasound Med Biol,* vol. 41, no. 1, pp. 77-88, Jan 2015.
[181] V. A. Korshunov, H. Wang, R. Ahmed, D. M. Mickelsen, Q. Zhou, C. Yan *et al.*, "Model-based vascular elastography improves the detection of flow-induced carotid artery remodeling in mice," *Sci Rep,* vol. 7, no. 1, p. 12081, Sep 21 2017.
[182] H. Hasegawa and H. Kanai, "Simultaneous imaging of artery-wall strain and blood flow by high frame rate acquisition of RF signals," *IEEE transactions on ultrasonics, ferroelectrics, and frequency control,* vol. 55, no. 12, pp. 2626-2639, 2008.
[183] M. Larsson, F. Kremer, P. Claus, T. Kuznetsova, L.-Å. Brodin, and J. D'hooge, "Ultrasound-based radial and longitudinal strain estimation of the carotid artery A feasibility study," *IEEE transactions on ultrasonics, ferroelectrics, and frequency control,* vol. 58, no. 10, pp. 2244-2251, 2011.
[184] R. J. Housden, A. H. Gee, G. M. Treece, and R. W. Prager, "Sub-sample interpolation strategies for sensorless freehand 3D ultrasound," *Ultrasound in medicine & biology,* vol. 32, no. 12, pp. 1897-1904, 2006.
[185] A. H. Gee, R. James Housden, P. Hassenpflug, G. M. Treece, and R. W. Prager, "Sensorless freehand 3D ultrasound in real tissue: speckle decorrelation without fully developed speckle," *Med Image Anal,* vol. 10, no. 2, pp. 137-149, Apr 2006.
[186] C. Laporte and T. Arbel, "Learning to estimate out-of-plane motion in ultrasound imagery of real tissue," *Med Image Anal,* vol. 15, no. 2, pp. 202-213, Apr 2011.
[187] N. Afsham, M. Najafi, P. Abolmaesumi, and R. Rohling, "A generalized correlation-based model for out-of-plane motion estimation in freehand ultrasound," *IEEE Trans Med Imaging,* vol. 33, no. 1, pp. 186-199, Jan 2014.
[188] M. Cinthio, A. R. Ahlgren, J. Bergkvist, T. Jansson, H. W. Persson, and K. Lindstrom, "Longitudinal movements and resulting shear strain of the arterial wall," *Am J Physiol Heart Circ Physiol,* vol. 291, no. 1, pp. H394-402, Jul 2006.
[189] A. Swillens, L. løvstakken, J. Kips, H. Torp, and P. Segers, "Ultrasound simulation of complex flow velocity fields based on computational fluid dynamics," *IEEE transactions on ultrasonics, ferroelectrics, and frequency control,* vol. 56, no. 3, pp. 546-556, 2009.

[190] S. J. Kleis and L. A. Sanchez, "Dependence of speed of sound on salinity and temperature in concentrated NaCl solutions," *Solar Energy,* vol. 45, no. 4, pp. 201-206, 1990.
[191] D. Garcia, L. L. Tarnec, S. Muth, E. Montagnon, J. Poree, and G. Cloutier, "Stolt's f-k migration for plane wave ultrasound imaging," *IEEE Transactions on Ultrasonics, Ferroelectrics, and Frequency Control,* vol. 60, no. 9, pp. 1853-1867, 2013.
[192] G. Cloutier, M. R. Cardinal, Y. Ju, M. F. Giroux, S. Lanthier, and G. Soulez, "Carotid plaque vulnerability assessment using ultrasound elastography and echogenicity analysis," *AJR Am J Roentgenol,* vol. 211, no. 4, pp. 847-855, Oct 2018.
[193] F. Destrempes, J. Meunier, M. F. Giroux, G. Soulez, and G. Cloutier, "Segmentation of plaques in sequences of ultrasonic B-mode images of carotid arteries based on motion estimation and a Bayesian model," *IEEE Trans Biomed Eng,* vol. 58, no. 8, pp. 2202-2211, Aug 2011.
[194] G. Zahnd, L. Boussel, A. Marion, M. Durand, P. Moulin, A. Serusclat *et al.*, "Measurement of two-dimensional movement parameters of the carotid artery wall for early detection of arteriosclerosis: a preliminary clinical study," *Ultrasound Med Biol,* vol. 37, no. 9, pp. 1421-1429, Sep 2011.
[195] J. Tat, J. S. Au, P. J. Keir, and M. J. MacDonald, "Reduced common carotid artery longitudinal wall motion and intramural shear strain in individuals with elevated cardiovascular disease risk using speckle tracking," *Clin Physiol Funct Imaging,* vol. 37, no. 2, pp. 106-116, Mar 2017.
[196] G. Zahnd, M. Orkisz, A. Serusclat, P. Moulin, and D. Vray, "Evaluation of a Kalman-based block matching method to assess the bi-dimensional motion of the carotid artery wall in B-mode ultrasound sequences," *Med Image Anal,* vol. 17, no. 5, pp. 573-585, Jul 2013.
[197] J. Jiang, T. J. Hall, and A. M. Sommer, "A novel performance descriptor for ultrasonic strain imaging: A preliminary study," *IEEE transactions on ultrasonics, ferroelectrics, and frequency control,* vol. 53, no. 6, pp. 1088-1102, 2006.
[198] J. Jiang, T. J. Hall, and A. M. Sommer, "A novel image formation method for ultrasonic strain imaging," *Ultrasound Med Biol,* vol. 33, no. 4, pp. 643-652, Apr 2007.
[199] J. Tat, I. N. Psaromiligkos, and S. S. Daskalopoulou, "Carotid atherosclerotic plaque alters the direction of longitudinal motion in the artery wall," *Ultrasound Med Biol,* vol. 42, no. 9, pp. 2114-2122, Sep 2016.
[200] R. J. Dempsey, T. Varghese, D. C. Jackson, X. Wang, N. H. Meshram, C. C. Mitchell *et al.*, "Carotid atherosclerotic plaque instability and cognition determined by ultrasound-measured plaque strain in asymptomatic patients with significant stenosis," *J Neurosurg,* vol. 128, no. 1, pp. 111-119, Jan 2018.
[201] J. Ophir, S. K. Alam, B. Garra, F. Kallel, E. Konofagou, T. Krouskop *et al.*, "Elastography: ultrasonic estimation and imaging of the elastic properties of tissues," *Proceedings of the Institution of Mechanical Engineers, Part H: Journal of Engineering in Medicine,* vol. 213, no. 3, pp. 203-233, 1999.
[202] U. Techavipoo and T. Varghese, "Wavelet denoising of displacement estimates in elastography," *Ultrasound Med Biol,* vol. 30, no. 4, pp. 477-491, Apr 2004.
[203] M. Arigovindan, M. Suhling, C. Jansen, P. Hunziker, and M. Unser, "Full motion and flow field recovery from echo Doppler data," *IEEE Trans Med Imaging,* vol. 26, no. 1, pp. 31-45, Jan 2007.

[204] N. Ouzir, A. Basarab, H. Liebgott, B. Harbaoui, and J. Y. Tourneret, "Motion estimation in echocardiography using sparse representation and dictionary learning," *IEEE Trans Image Process,* vol. 27, no. 1, pp. 64-77, Jan. 2018.
[205] N. Ouzir, A. Basarab, O. Lairez, and J. Y. Tourneret, "Robust optical flow estimation in cardiac ultrasound images using a sparse representation," *IEEE Trans Med Imaging,* vol. 38, no. 3, pp. 741-752, Sep 18 2019.
[206] X. Shen and Y. Wu, "Exploiting sparsity in dense optical flow," *IEEE International Conference on Image Processing,* pp. 741-744, 2010.
[207] X. Shen and Y. Wu, "Sparsity model for robust optical flow estimation at motion discontinuities," *IEEE Computer Society Conference on Computer Vision and Pattern Recognition,* pp. 2456-2463, 2010.
[208] J. Han, F. Qi, and G. Shi, "Gradient sparsity for piecewise continuous optical flow estimation," *IEEE International Conference on Image Processing,* pp. 2389-2392, 2011.
[209] D. L. Donoho, "Compressed sensing," *IEEE Transactions on Information Theory,* vol. 52, no. 4, pp. 1289-1306, 2006.
[210] G. Aubert, R. Deriche, and P. Kornprobst, "Computing optical flow via variational techniques," *SIAM Journal on Applied Mathematics,* vol. 60, no. 1, pp. 156-182, 1999.
[211] T. Rohlfing, C. R. Maurer, Jr., D. A. Bluemke, and M. A. Jacobs, "Volume-preserving nonrigid registration of MR breast images using free-form deformation with an incompressibility constraint," *IEEE Trans Med Imaging,* vol. 22, no. 6, pp. 730-741, Jun 2003.
[212] B. Chakraborty, Z. Liu, B. Heyde, J. Luo, and J. D'Hooge, "2-D myocardial deformation imaging based on RF-based nonrigid image registration," *IEEE Transactions on Ultrasonics, Ferroelectrics, and Frequency Control,* vol. 65, no. 6, pp. 1037-1047, 2018.
[213] A. Karimi, T. Sera, S. Kudo, and M. Navidbakhsh, "Experimental verification of the healthy and atherosclerotic coronary arteries incompressibility via Digital Image Correlation," *Artery Research,* vol. 16, pp. 1-7, 2016.
[214] T. Liang, L. Yung, and W. Yu, "On feature motion decorrelation in ultrasound speckle tracking," *IEEE Trans Med Imaging,* vol. 32, no. 2, pp. 435-448, Feb 2013.
[215] T. Mansi, X. Pennec, M. Sermesant, H. Delingette, and N. Ayache, "iLogDemons: A demons-based registration algorithm for tracking incompressible elastic biological tissues," *International Journal of Computer Vision,* vol. 92, no. 1, pp. 92-111, 2010.
[216] A. Gomez, K. Pushparajah, J. M. Simpson, D. Giese, T. Schaeffter, and G. Penney, "A sensitivity analysis on 3D velocity reconstruction from multiple registered echo Doppler views," *Medical Image Analysis,* vol. 17, no. 6, pp. 616-631, Aug 2013.
[217] A. Gomez, A. de Vecchi, M. Jantsch, W. Shi, K. Pushparajah, J. M. Simpson *et al.*, "4D blood flow reconstruction over the entire ventricle from wall motion and blood velocity derived from ultrasound data," *IEEE Trans Med Imaging,* vol. 34, no. 11, pp. 2298-2308, Nov 2015.
[218] M. Amato, F. Veglia, U. de Faire, P. Giral, R. Rauramaa, A. J. Smit *et al.*, "Carotid plaque-thickness and common carotid IMT show additive value in cardiovascular risk prediction and reclassification," *Atherosclerosis,* vol. 263, pp. 412-419, Aug 2017.
[219] H. Li, B. Chayer, M.-H. Roy Cardinal, J. Muijsers, M. van den Hoven, Z. Qin *et al.*, "Investigation of out-of-plane motion artifacts in 2D noninvasive vascular ultrasound elastography," *Physics in Medicine & Biology,* vol. 63, no. 24, p. 245003, 2018.

[220] D. Sun, S. Roth, and M. J. Black, "Secrets of optical flow estimation and their principles," *IEEE computer society conference on Computer Vision and Pattern Recognition,* pp. 2432-2439, 2010.
[221] W. Dong, G. Shi, X. Hu, and Y. Ma, "Nonlocal sparse and low-rank regularization for optical flow estimation," *IEEE Trans Image Process,* vol. 23, no. 10, pp. 4527-4538, Oct 2014.
[222] M. Tanter, M. Pernot, J. L. Gennisson, and M. Fink, "A review of the medical applications of shear wave elastography," *The Journal of the Acoustical Society of America,* vol. 134, no. 5, pp. 4009-4009, 2013.
[223] Y. K. Mariappan, K. J. Glaser, and R. L. Ehman, "Magnetic resonance elastography: a review," *Clin Anat,* vol. 23, no. 5, pp. 497-511, Jul 2010.
[224] S. Duffner and C. Garcia, "PixelTrack: A fast adaptive algorithm for tracking non-rigid objects," *IEEE International Conference on Computer Vision,* pp. 2480-2487, 2013.
[225] A. Itoh, E. Ueno, E. Tohno, H. Kamma, H. Takahashi, T. Shiina *et al.*, "Breast disease: clinical application of US elastography for diagnosis," *Radiology,* vol. 239, no. 2, pp. 341-350, 2006.
[226] A. Lu, N. Parajuli, M. Zontak, J. Stendahl, K. Ta, Z. Liu *et al.*, "Learning-based regularization for cardiac strain analysis with ability for domain adaptation," *arXiv preprint,* vol. arXiv, no. 1807, p. 04807, 2018.
[227] J. Provost, C. Papadacci, J. E. Arango, M. Imbault, M. Fink, J. L. Gennisson *et al.*, "3D ultrafast ultrasound imaging in vivo," *Phys Med Biol,* vol. 59, no. 19, pp. L1-L13, Oct 7 2014.
[228] C. Papadacci, E. A. Bunting, and E. E. Konofagou, "3D Quasi-static ultrasound elastography with plane wave in vivo," *IEEE Trans Med Imaging,* vol. 36, no. 2, pp. 357-365, Feb 2017.
[229] C. Naim, G. Cloutier, E. Mercure, F. Destrempes, Z. Qin, W. El-Abyad *et al.*, "Characterisation of carotid plaques with ultrasound elastography: feasibility and correlation with high-resolution magnetic resonance imaging," *Eur Radiol,* vol. 23, no. 7, pp. 2030-41, Jul 2013.

Appendix

List of journal articles:

1. **Hongliang Li,** Jonathan Porée, Marie-Hélène Roy Cardinal, Guy Cloutier. Two-dimensional affine model-based strain estimators for principal strain vascular ultrasound elastography with compound plane wave and transverse oscillation beamforming. *Ultrasonics*, 91: 77-91, 2019.

2. **Hongliang Li,** Boris Chayer, Marie-Hélène Roy Cardinal, Judith Muijsers, Marcel van den Hoven, Zhao Qin, Gilles Soulez, Richard G.P. Lopata, Guy Cloutier. Investigation of out-of-plane motion artifacts in 2D noninvasive vascular ultrasound elastography. *Physics in Medicine & Biology*, 63(24): 245003, 2018.

3. Boris Chayer, Marcel van den Hoven, Marie-Hélène Roy Cardinal, **Hongliang Li**, Abigail Swillens, Richard G.P. Lopata, Guy Cloutier. Atherosclerotic carotid bifurcation phantoms with stenotic soft inclusions for ultrasound flow and vessel wall elastography imaging. *Physics in Medicine & Biology*. 64(9): 095025, 2019.

4. **Hongliang Li,** Jonathan Porée, Boris Chayer, Marie-Hélène Roy Cardinal, Guy Cloutier. Parameterized strain estimation for vascular ultrasound elastography with a sparse model. *Submitted to IEEE Transactions on Medical Imaging*.

5. **Hongliang Li,** Guy Cloutier. Ultrasound strain elastography techniques: A review. *In preparation.*

List of peer reviewed conference papers:

1. **Hongliang Li,** Jonathan Porée, Guy Cloutier. A modified affine phase-based estimator for non-invasive vascular ultrasound elastography using coherent plane wave compounding and transverse oscillation imaging. *2016 IEEE International Ultrasonics Symposium (IUS), 2016 IEEE International. IEEE, 2016: 1-4*.

2. **Hongliang Li,** Jonathan Porée, Boris Chayer, Marie-Hélène Roy Cardinal, Guy Cloutier. A global strain estimation algorithm for non-invasive vascular ultrasound elastography. *2019 IEEE International Ultrasonics Symposium (IUS)*. *Accepted*.

3. Boris Chayer, Marcel van den Hoven, Marie-Hélène Roy Cardinal, **Hongliang Li,** Abigail Swillens, Richard G.P. Lopata, Guy Cloutier. Atherosclerotic carotid bifurcation phantoms with a stenotic soft inclusion for flow-structure ultrasound imaging analysis. *2019 IEEE International Ultrasonics Symposium (IUS)*. *Accepted*.

List of presentations:

1. **Hongliang Li,** Boris Chayer, Marie-Hélène Roy Cardinal, Judith Muijsers, Marcel van den Hoven, Richard G. P. Lopata, Guy Cloutier, "Investigation of out-of-plane motion artifacts in two-dimensional noninvasive vascular elastography using high-frame-rate ultrasound imaging on a diseased carotid bifurcation phantom", 10th Scientific Day of QBIN, Canada, March, 2018 (Poster).

2. **Hongliang Li,** Boris Chayer, Marie-Hélène Roy Cardinal, Judith Muijsers, Marcel van den Hoven, Richard G. P. Lopata, Guy Cloutier, "Investigation of out-of-plane motion artifacts in noninvasive vascular elastography using high-frame-rate ultrasound imaging: an *in vitro* vessel phantom study", 8^{e} Scientific Day of CRCHUM, Canada, October, 2017 (Poster).

3. **Hongliang Li,** Jonathan Porée, Guy Cloutier, "A phase-based strain estimator for non-invasive vascular ultrasound elastography using ultrafast transverse oscillation imaging", University Day of the Department of Radiology, Radiation Oncology and Nuclear Medicine of the Faculty of Medicine of the Université de Montréal, Canada, February, 2017 (Oral).

4. **Hongliang Li,** Jonathan Porée, Guy Cloutier, "A modified affine phase-based estimator for non-invasive vascular ultrasound elastography using coherent plane wave compounding and transverse oscillation imaging", 2016 IEEE International Ultrasonics Symposium, France, September, 2016 (Oral).

5. **Hongliang Li,** Jonathan Porée, Damien Garcia, Guy Cloutier, "Performance evaluation of two strain tensor estimators for noninvasive vascular ultrasound elastography", Artimino Ultrasound Conference, Sweden, June, 2015 (Oral).